QUANTITATIVE FLOW VISUALIZATION SYSTEM FOR GAS-LIQUID TWO PHASE FLOWS

JOHN E. HISCOCK

Your file Votre référence
ISBN: 0-612-89633-1
Our file Notre référence
ISBN: 0-612-89633-1

Quantitative Flow Visualization System

for Gas-Liquid Two Phase Flows

by

© John E. Hiscock, B. Eng.

A thesis submitted to the

School of Graduate Studies

in partial fulfillment of the

requirements for the degree of

Master of Engineering

Faculty of Engineering and Applied Science

Memorial University of Newfoundland

July 2000

St. John's Newfoundland Canada

Perfection is reached, not when there is no longer anything to add,

but when there is no longer anything to take away.

A. Saint Exupery

Abstract

The main objective of this research was to develop a quantitative flow visualization technique to measure gas bubble size and velocities of vertical-up gas-liquid flows. A system to acquire high-speed digital images was designed and integrated with a hot-film anemometry system in the test section of the 76 mm flow loop at Memorial University of Newfoundland. Digital image processing algorithms were developed to obtain the gas bubble size and velocity information from the high-speed flow images. The gas slug and bubble velocities were estimated using two separate image processing algorithms: a supervised motion tracking algorithm and an edge detection cross-correlation algorithm. The supervised motion tracking algorithm allows the user to identify and track the movement of distinguishable gas bubbles and slugs. The edge detection cross-correlation algorithm uses standard edge detection routines to identify the boundaries of the slugs and bubbles. The bubble size information is obtained through morphological operations on the edge-detected images. The displacement of the bubbles between two frames is obtained through a cross-correlation analysis between the frames. Measurements were performed in the slug flow regime at several gas and liquid superficial velocities. Results obtained from the quantitative noninvasive flow visualization and image analysis techniques are in good agreement with results from simultaneous hot film anemometry measurements.

Acknowledgements

Financial support from the Natural Sciences and Engineering Research Council (NSERC) Scholarship; the Faculty of Engineering and Applied Science, Memorial University of Newfoundland; and the author's supervisor, Dr. Chan Ching is greatly acknowledged. The generous support and contributions to the multiphase flow research program at Memorial University of Newfoundland from INSTRUMAR Ltd. is also gratefully recognized.

My deepest and sincere gratitude is extended to my supervisor, Dr. Chan Ching, for his continued support, constructive guidance and invaluable advice throughout this project. His kindness, respect and patience are deeply admired.

Personal thanks are extended to the author's fiancée, Reeni Woolgar, for her moral support and advice throughout the program. An expression of thanks is also extended to Dr. John Robinson for his ongoing image processing advice and Alfred Marshal of INSTRUMAR Limited for his continued input and discussion. I would also like to recognize friend Guanjun Wang for his support and assistance throughout the project.

Finally, I am forever indebted to my parents, John and Ruby, for their continuous support, encouragement and assistance.

Table of Contents

Abstract iii

Acknowledgements iv

List of Tables viii

List of Figures x

Chapter 1
Introduction 1

1.1 Background 2

1.2 Objectives 4

1.3 Outline of Thesis 5

Chapter 2
Literature Review 6

2.1 Vertically Upward Gas-Liquid Two-Phase Flows 6

2.2 Intrusive Multiphase Flow Measurement Techniques 11

2.3 Non-Intrusive Multiphase Flow Measurement Techniques 17

Chapter 3
Flow Loop Facility 25

3.1 Description of the Flow Loop 25

3.2 Flow Visualization System 30

3.2.1 Digital Imaging System 30

3.2.2 Lighting Techniques 34

3.3 Hot-Film Anemometry System 35

3.4 Simultaneous Flow Visualization and Hot-Film Measurements 37

Chapter 4
Data Reduction 40

4.1 Supervised Motion Tracking Algorithms 41

4.1.1 Mesh Tracking Software 42

4.1.2 Camera Software 43

4.2 Edge Detection Cross-Correlation Algorithm 44

4.2.1 REDUCTION Function 46

4.2.2 MULTIMAGES Function 47

4.2.3 BUBBLEFILL Function 48

4.2.4 RELBUBBLESIZE and BUBBLECLASSIFICATION Functions 51

4.2.5 CROSSCORR Function 54

4.2.6 VELCLASSMATCH Function 58

4.3 Hot-Film Data Reduction Technique 61

4.3.1 Data Reduction 62

4.3.2 Wavelet Signal Decomposition 63

4.3.3 Bubble and Slug Extraction 67

4.3.4 Bubble Velocity and Size Estimation 69

Chapter 5
Results and Discussion 71

5.1 Flow Visualization Results 72

5.1.1 Motion Tracking Algorithm Results 72

5.1.2 Edge Detection Cross-Correlation Algorithm Results 82

5.2 Simultaneous Flow Visualization and Hot-Film Measurement Results 108

5.2.1 Dynamic Response of the Hot-Film to the Passage of a Gas Slug 108

5.2.2 Comparison of Flow Visualization and Hot Film Measurement Results 110

Chapter 6
Conclusions and Recommendations 114

6.1 Conclusions 114

6.2 Research Contributions 116

6.3 Recommendations 117

References 120

Appendix A
MATLAB Program Listing for Edge Detection Cross-Correlation Algorithm ... 125

List of Tables

Table 3.1: Flow Loop Specifications 27

Table 3.2: Exposure Times for Set Shutter Speeds 33

Table 3.3: Camera Specifications 33

Table 4.1: Bubble Size and Position Information from the Analysis of Figure 4.6(a) 53

Table 4.2: Velocity Matrix showing Segment Velocities (m/s) 57

Table 4.3: Velocity Matrix (m/s) with Selected Slug Velocities (as per Figure 4.9) shown in Italics 61

Table 5.1: Test Conditions 71

Table 5.2: Camera Recording Parameters 72

Table 5.3: Case A-1, Motion Tracking Results 75

Table 5.4: Case B-1 Motion Tracking Results 76

Table 5.5: Case C-3, Motion Tracking Results 77

Table 5.6: Case D-3, Motion Tracking Results 78

Table 5.7: Case E-2, Motion Tracking Results 79

Table 5.8: Case F-4, Motion Tracking Results 80

Table 5.9: Slug and Bubble Velocities determined from the Motion Tracking Algorithm 82

Table 5.10: Summary of Figure and Table Numbers for Flow Visualization Results 83

Table 5.11: Case A-1, Velocity Vector Matrix Frames 120-121 85

Table 5.12: Case A-1, Velocity Vector Matrix Frames 121-122 85

Table 5.13: Case A-1, Velocity Vector Matrix Frames 122-123 85

Table 5.14: Case B-1, Velocity Vector Matrix Frames 23-24 88

Table 5.15: Case B-1, Velocity Vector Matrix Frames 24-25 88

Table 5.16: Case B-1, Velocity Vector Matrix Frames 25-26 88

Table 5.17: Case C-3, Velocity Vector Matrix Frames 277-278 91

Table 5.18: Case C-3, Velocity Vector Matrix Frames 278-279 91

Table 5.19: Case C-3, Velocity Vector Matrix Frames 279-280 91

Table 5.20: Case D-3, Velocity Vector Matrix Frames 128-129 94

Table 5.21: Case D-3, Velocity Vector Matrix Frames 129-130 94

Table 5.22: Case D-3, Velocity Vector Matrix Frames 130-131 94

Table 5.23: Case E-2, Velocity Vector Matrix Frames 329-330 97

Table 5.24: Case E-2, Velocity Vector Matrix Frames 330-331 97

Table 5.25: Case E-2, Velocity Vector Matrix Frames 331-332 97

Table 5.26: Case F-4, Velocity Vector Matrix Frames 374-375 100

Table 5.27: Case F-4, Velocity Vector Matrix Frames 375-376 100

Table 5.28: Case F-4, Velocity Vector Matrix Frames 376-377 100

Table 5.29: Slug and Bubble Velocities determined from the Edge Detection Cross-Correlation Algorithm and Comparison with Motion Tracking Results 102

Table 5.30: Slug Velocity from Cross-Correlation Algorithm with Modified Images and Discrepancy with Motion Tracking Results 105

Table 5.31: Comparison of Results Table 5.32: Discrepancy of Average Velocity from Motion Tracking with Edge Detection Cross-Correlation and Hot – Film 111

Table 5.32: Discrepancy of Average Velocity from Motion Tracking with Edge Detection Cross-Correlation and Hot –Film 112

List of Figures

Figure 2.1: Flow Patterns in Vertically Upward Two-Phase Flow 9

Figure 2.2: Generic Flow Regime Map 11

Figure 2.3: Hot-Film Anemometry Voltage Signal and Bubble-Probe Interaction in Bubbly Flow (Kirouac et al., 1999) 14

Figure 2.4: Typical Hot-Film Signal in Air-Water Slug Flow: (a) Hot-Film Signal; (b) Void Fraction Function 14

Figure 2.5: U-Shaped Optical Fiber Sensor Probe and its Principle of Operation 17

Figure 2.6: Schematic of Gamma Densitometer 24

Figure 3.1: Pictorial Representation of the Flow Loop Layout 26

Figure 3.2: Flow Loop Schematic 26

Figure 3.3: Operational Section of Flow Loop 27

Figure 3.4: Flow Metering Section of Flow Loop 28

Figure 3.5: Control Equipment for Flow Loop and Equipment for Hot-Film and Flow Visualization Systems 29

Figure 3.6: Schematic of Flow Loop Control/Data Acquisition and Hot-Film and Flow Visualization Systems 30

Figure 3.7: Top View of Flow Visualization System 31

Figure 3.8: Flow Visualization Test Section 32

Figure 3.9: Laser Light Sheet and Illuminated Calibration Scale 34

Figure 3.10: Back Light Illumination and Calibration Scale 35

Figure 3.11: Hot-Film Test Section 36

Figure 3.12: Schematic of Hot-Film Probe Setup 37

Figure 3.13: Schematic of Trigger Operation 38

Figure 3.14: Camera Positions for Simultaneous Flow Visualization and Hot-Film Measurements 38

Figure 4.1: Mesh Tracking User Interface 43

Figure 4.2: Camera Software User Interface 44

Figure 4.3: Outline of MATLAB edge detection cross correlation routine 46

Figure 4.4:Edge Detection Cross-Correlation Algorithm (a) Consecutive Frames with Polygon Bounding Slug; (b) Processed Image 49

Figure 4.5: Edge Detection Cross-Correlation Algorithm (a) Consecutive Frames; (b) Processed Image without Manual Indication of Slug 49

Figure 4.6: Edge Detection Cross-Correlation Algorithm (a) Consecutive Frames; (b)Application of Edge Detection; (c)Application of Morphological Operations 51

Figure 4.7: Cross-Correlation between Images from Figure 3(c) 56

Figure 4.8: Segmentation Grid and Velocity Vector Plot generated using the Cross-Correlation Algorithm 58

Figure 4.9: Velocity Vector Locations for an Assumed Circular Slug or Medium Bubble Geometry 59

Figure 4.10: Schematic of Velocity Estimation Procedure 63

Figure 4.11: Typical Hot-film Signal and Wavelet Transformation: (a) Hot-Film Signal; (b) Wavelet Transformation Plot 64

Figure 4.12: Fifth Order Symlet Wavelet Mother Function and Scale Function 66

Figure 4.13: Hot-Film Signal and Corresponding Wavelet Decomposition Approximations: (a) Original Hot-Film Signal; (b) Level Two Wavelet Approximation; (c) Level Three Wavelet Approximation 66

Figure 4.14: Wavelet Approximation and its Phase Indicator Function: (a) Level Three Wavelet Approximation; (b) Phase Indicator Function 68

Figure 4.15: Separated Slug and Bubble Signals: (a) Original Signal; (b) Slug Signal; (c) Bubble Signal 69

Figure 4.16: Typical Cross Correlation Function 70

Figure 5.1: Bubble and Slug Identification for Motion Tracking Analysis 74

Figure 5.2: Case A-1, Original Images Frames 120-123 84

Figure 5.3: Case A-1, Filled Images Frames 120-123 84

Figure 5.4: Case A-1, Velocity Vector Plots Frames 120-123 84

Figure 5.5: Case A-1, Bubble Size Histogram Frames 120-121 86

Figure 5.6: Case A-1, Bubble Size Histogram Frames 121-122 86

Figure 5.7: Case A-1, Bubble Size Histogram Frames 122-123 86

Figure 5.8: Case B-1, Original Images Frames 23-26 87

Figure 5.9: Case B-1, Filled Images Frames 23-26 87

Figure 5.10: Case B-1, Velocity Vector Plots Frames 23-26 87

Figure 5.11: Case B-1, Bubble Size Histogram Frames 23-24 89

Figure 5.12: Case B-1, Bubble Size Histogram Frames 24-25 89

Figure 5.13: Case B-1, Bubble Size Histogram Frames 25-26 89

Figure 5.14: Case C-3, Original Images Frames 277-280 90

Figure 5.15: Case C-3, Filled Images Frames 277-280 90

Figure 5.16: Case C-3, Velocity Vector Plots Frames 277-280 90

Figure 5.17: Case C-3, Bubble Size Histogram Frames 277-278 92

Figure 5.18: Case C-3, Bubble Size Histogram Frames 278-279 92

Figure 5.19: Case C-3, Bubble Size Histogram Frames 279-280 92

Figure 5.20: Case D-3, Original Images Frames 128-131 93

Figure 5.21: Case D-3, Filled Images Frames 128-131 93

Figure 5.22: Case D-3, Velocity Vector Plots for Frames 128-131 93

Figure 5.23: Case D-3, Bubble Size Histogram Frames 128-129 95

Figure 5.24: Case D-3, Bubble Size Histogram Frames 129-130 95

Figure 5.25: Case D-3, Bubble Size Histogram Frames 130-131 95

Figure 5.26: Case E-2, Original Images Frames 329-332 96

Figure 5.27: Case E-2, Filled Images Frames 329-332 96

Figure 5.28: Case E-2, Velocity Vector Plots Frames 329-332 96

Figure 5.29: Case E-2, Bubble Size Histogram Frames 329-330 98

Figure 5.30: Case E-2, Bubble Size Histogram Frames 330-331 98

Figure 5.31: Case E-2, Bubble Size Histogram Frames 331-332 98

Figure 5.32: Case F-4, Original Images Frames 374-377 99

Figure 5.33: Case F-4, Filled Images Frames 374-377 99

Figure 5.34: Case F-4, Velocity Vector Plots Frames 374-377 99

Figure 5.35: Case F-4, Bubble Size Histogram Frames 374-375 101

Figure 5.36: Case F-4, Bubble Size Histogram Frames 375-376 101

Figure 5.37: Case F-4, Bubble Size Histogram Frames 376-377 101

Figure 5.38: Manual Modification of Flow Images for Case B-1: (a) Original Images; (b) Bubbles Cropped from Images; (c) Edge Detection; (d) Slug Identification 106

Figure 5.39: Dynamic Hot-Film Response to the Passage of a Gas Slug 109

Figure 6.1: A Time Sequence Showing the Passage of a Gas Slug obtained using the Laser Light Sheet Technique 119

Figure 6.2: A Time Sequence Showing the Passage of Gas Bubbles obtained using the Laser Light Sheet Technique 119

Chapter 1

Introduction

Gas-liquid multiphase transport in pipe networks has become a key technological feature in the oil and gas industry. The accurate prediction of multiphase flow characteristics is important in this complex field of study. Gas-liquid flows, characterized by turbulence, deformable phase interface, phase interaction and slip are extremely difficult to model. Despite its complexity, the distribution of gas and liquid in vertical-up flows can be classified into a few dominant flow patterns or regimes: bubble flow, slug flow, churn flow and annular flow (Hetsroni, 1982). The accurate measurement of phase velocities in each of these flow regimes is necessary to develop and validate mechanistic models of the flow. Both intrusive and non-intrusive flow measurement techniques have been used with varying degrees of success to measure phase velocity, bubble size distribution and void fractions. It is still a challenge, however, to accurately measure local phase velocities and void fraction distributions. In this thesis, a new technique has been developed to measure gas bubble and slug velocities using a high speed flow visualization system. The gas bubble velocity measurements are corroborated using hot-film anemometry and an algorithm to obtain bubble size information from the flow images has also been developed. This study has been motivated by a project to develop a Multi-Phase Flow Meter (MPFM) to measure the individual oil-water-gas flow rates of unprocessed production oil-well streams.

1.1 Background

The unprocessed oil-well stream from a petroleum reservoir consists of a multi-phase mixture of crude oil, brine and natural gas. Real-time information of the gas-oil-water production rates of each well is expected to result in improved reservoir management, and thereby maximize the recovery from the reservoir; however, this data is currently not available. Presently, on a monthly or semi-monthly basis, the output from each well is diverted to a test separator system, and the flow rates are estimated from measurements on the separated components. Extrapolating the data outside the measurement interval has a high degree of uncertainty as the flow rate sampling is effectively done over a small fraction of the total production time of a well.

INSTRUMAR Ltd., with the assistance of C-CORE/Memorial University of Newfoundland (MUN), is developing an in-line oil-water-gas Multi-Phase Flow Meter (MPFM) to measure the individual oil-water-gas flow rates of unprocessed production oil well streams. The MPFM operates by measuring a sequence of impedances at two streamwise locations. Using advanced signal analysis and pattern recognition techniques, the impedance signals are processed to estimate the individual volume fractions and local phase velocities of each component (oil-water-gas). Because several different flow regimes with complex interfacial patterns may be present in the multi-phase flow, the estimation must be preceded by an identification of the flow regime. The flow identification is based on information extracted from different electrode patterns, and the signals are then compared to pattern-specific features that have been previously

identified. Due to the complexity and large number of flow regimes that are likely to be encountered in the practical situation, accurate identification and modeling of the flow regimes are essential for correct signal analysis.

The complexity of oil-water-gas multiphase flows makes it improbable that a complete analytical (theoretical) model of the flow can be obtained. A number of semi-empirical models can be used to develop a composite model for use in the velocity inversion algorithm of the MPFM. The models, however, will need to be refined and validated by testing the prototype MPFM over the different flow regimes. These tests are essential to validate the fluid modeling, and to meet the specification requirements of the meter.

A research program in Multiphase flows has been initiated at MUN to support the development of the MPFM through a Natural Sciences and Engineering Research Council (NSERC) collaborative research and development grant. The overall objective of the research program is to develop innovative flow identification and velocity estimation techniques for gas-oil-water multiphase pipeline flows. A multiphase flow loop facility was designed and constructed at MUN to investigate oil-water-gas flows. Test sections for both flow visualization and hot-film anemometry measurements are incorporated into the flow loop. The signal and image processing algorithms to elicit quantitative information from the flow visualization and hot-film anemometry measurements have been developed. The data from these measurements will be used to

develop mechanistic models of the flow that can be incorporated in the velocity inversion algorithms of the MPFM.

1.2 Objectives

Flow visualization is a powerful and versatile experimental tool, which has been used to obtain some of the most significant insights into the behavior of complex fluid flow phenomena. When flow visualization is complemented by quantitative measurements, it provides a powerful tool to deduce much of the physics associated with the flow. With the rapid technological improvements in digital image recording and processing over the last few years, it is now possible to obtain quantitative information directly from flow visualization images. The main objective of the present study is to develop a quantitative flow visualization system to measure the gas bubble velocities and size in vertical-up gas-liquid flow. The specific objectives of the research are:

1. To design, procure and install a high-speed flow visualization system in the MUN flow loop facility to study gas-liquid flows.
2. To investigate the utility of motion tracking algorithms to determine gas bubble velocities from the flow images.
3. To develop image processing algorithms to obtain velocity and bubble size information from the flow images.
4. To corroborate the quantitative flow visualization measurements with corresponding hot-film anemometry measurements.

5. To obtain gas bubble and slug velocities over a range of gas-liquid flow rates.

1.3 Outline of Thesis

This thesis is sub-divided into five additional chapters. An overview of vertical-up gas-liquid multiphase flow is presented in Chapter 2. Intrusive and non-intrusive multiphase flow measurement techniques are also reviewed in this chapter. In Chapter 3, the experimental facilities and instrumentation are described. This includes a description of both the flow visualization and hot-film anemometry measurement systems. The data reduction techniques for the flow visualization and hot-film anemometry measurements are presented in Chapter 4. The quantitative flow visualization results from several test cases are compared with simultaneous hot-film anemometry results in Chapter 5. Concluding remarks and recommendations for future work are given in Chapter 6

Chapter 2

Literature Review

Although many different flow measurement techniques are available in the chemical, petroleum and nuclear industries, there still exists a lack of instrumentation for accurate multiphase flow measurements. This is primarily due to a poor understanding of such flows. The accurate design of any multiphase flow measurement system is, in part, contingent upon a good understanding of multiphase flow behavior. The measurement of multiphase flows is an area of active research at many academic institutions and in the power and process industries. There is an industrial need for effective multiphase flow meters that can operate in real-time and produce accurate measurements. The development of such a meter, however, requires an extensive understanding of the flow physics. An overview of vertical-up multiphase flow and some of the associated measurement techniques are reviewed in this chapter. Although the scope of this research is limited to vertically upward two-phase gas-liquid flows, many of the fundamentals apply to other types of multiphase flows. Vertical-up gas-liquid flows are discussed in Section 2.1 and intrusive and non-intrusive flow measurement techniques are reviewed in Sections 2.2 and 2.3 respectively.

2.1 Vertically Upward Gas-Liquid Two-Phase Flows

The interfacial interaction between the gas and liquid phases determines the shape of the gas bubbles in a multiphase flow. Instantaneous bubble shape and size are important,

because they reflect the dynamic changes in pressure inside the bubble and in the surrounding fluid. This can have a significant effect on the velocity field of the surrounding fluid. The bubble shape and size also play an important role in heat and mass transfer between the two phases, since they determine the interfacial area available for such phenomena. The bubble dimensions directly affect the drag coefficient, and hence the velocity and path. Despite the flow complexity, the distribution of gas and liquid in two-phase vertical-upward flows falls into four dominant flow patterns (regimes).

Flow regimes for vertical and horizontal flows have their own distinct characteristics because of the different influence of gravity. Flow regimes in horizontal flow tend to be somewhat more complex than those in vertical flow due to the asymmetry in the flow induced by the gravitational force acting normal to the direction of flow. There are four basic flow regimes for vertical upward flow: bubble flow, slug flow, churn flow and annular flow (Fig. 2.1). The flow transitions from one regime to the other as the volume fraction of gas increases. Hewitt's (1970) description of these flow regimes might be the most accurate and recognized. A brief description of each of the four regimes is given below:

1. Bubble Flow – Characterized by a dispersion of approximately uniformly distributed gas bubbles within the continuous liquid phase. The bubbles and the continuous liquid phase move at similar velocities.

2. Slug or Plug Flow – Characterized by the appearance of large, bullet-shaped bubbles, which have diameters nearly equal to the pipe diameter and move uniformly upward. Although the net flow of both the liquid and gas is in the upward direction, the liquid can flow locally down outside of the bubble in a falling film.

3. Churn Flow – Characterized by the appearance of bullet-shaped bubbles, as for the slug flow regime, but is much more unstable, foamy and disordered. It occurs at a higher gas flow rate compared with that of the slug flow. It is typically observed as an oscillatory motion of the liquid upward and downward with increasing flow velocity.

4. Annular Flow – Characterized by the presence of a continuous column or core of gas along the pipe, which is surrounded by a continuous annulus of the liquid phase. The liquid phase moves upwards partly as a wavy liquid film and partially in the form of droplets entrained in the gas core at a sufficiently high gas velocity. A wispy-annular flow regime describes annular flows with a liquid phase in the form of large lumps or wisps.

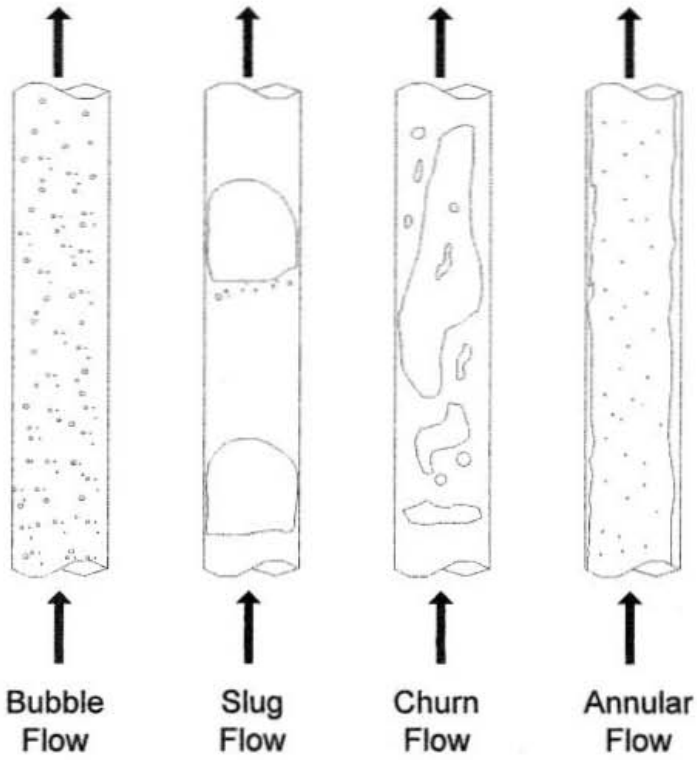

Figure 2.1: Flow Patterns in Vertically Upward Two-Phase Flow

Mcquillan and Whalley (1985) provide a much more detailed description of the four flow regimes that includes the transition flow regimes between each of the main flow regimes. Slug/churn flow occurs when the flow pattern oscillates between slug and churn and churn/annular flow occurs when the flow appears as annular flow but with occasional intermittent churn flow. Although the problem of two-phase flow modeling can be greatly simplified by only dealing with these specific flow regimes, the flow behavior within a given flow regime is very complex and not susceptible to any direct calculation.

This has led to a variety of phenomenological models that have been used with varying degrees of success (Hetsroni, 1982).

One of the most important tasks in two-phase flow modeling is to predict flow regimes under various flow conditions. Two-phase flow regimes are very complex and their formations depend on phase flow rates, fluid physical properties, and flow geometry. The usual way of modeling two-phase flow regimes is to form a so-called flow regime map in which the flow patterns are plotted on two axes representing certain physical characteristics of the two phases. Kosterin (1949) was probably the first to suggest the use of a flow regime map. The most common maps are plotted with superficial velocities as the mapping coordinates, or as a combination of parameters that include velocities (Baker, 1954; Lin and Hanratty, 1987). The superficial velocity is defined as the average velocity in the absence of the second phase and is a measure of the individual phase volume flow rate. The flow regimes are presented as specified areas on the graph with transition boundaries separating the individual flow regimes. Figure 2.2 shows a generic flow map based on the superficial gas and liquid velocities with lines representing the transition boundaries between the different flow regimes.

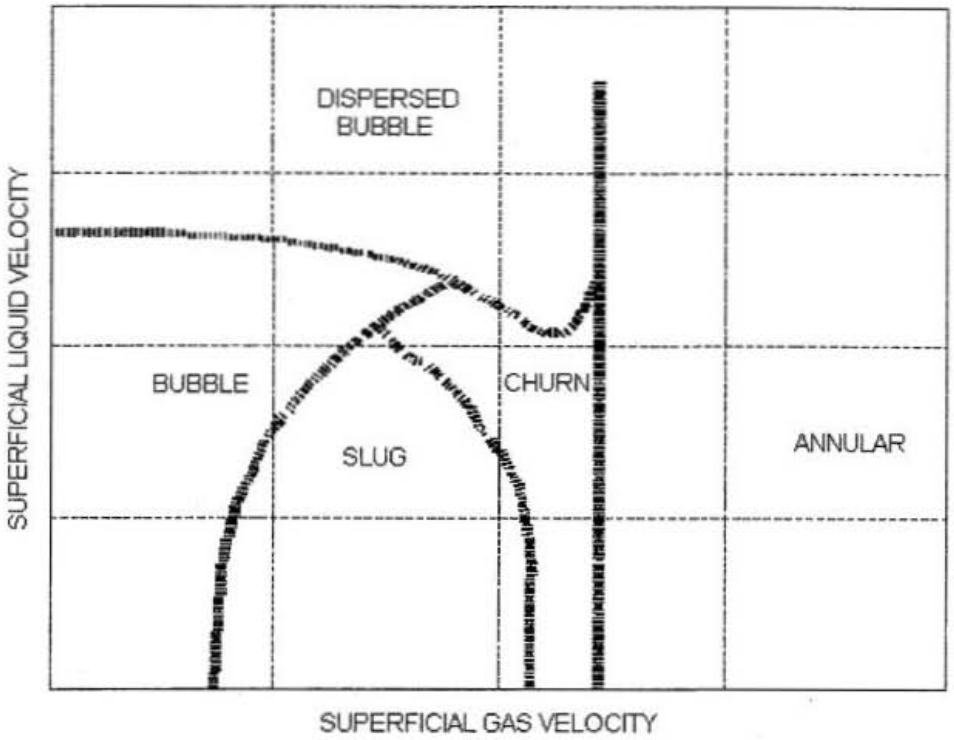

Figure 2.2: Generic Flow Regime Map

2.2 Intrusive Multiphase Flow Measurement Techniques

Quantitative information of the flow, such as local phase velocity, void fraction, phase distribution, bubble size distribution and bubble velocity are required to develop and validate accurate flow models. Several intrusive and non-intrusive methods have been developed to perform such measurements. Intrusive measurement techniques have been frequently used in laboratory settings to measure void fraction, gas bubble size and velocities. The three most common techniques for such measurements use resistivity probes, optical probes and hot-film probes. Each method is based on an operating

principle of phase detection using variations of the local fluid properties of the two phases. Gas bubble velocities are usually estimated by measuring the time for a bubble to travel the distance between two probes spaced apart in the streamwise direction. A direct cross-correlation between the signals from two probes spaced apart in the streamwise direction yields an average time-difference-of-arrival at the two probes. The three methods, which provide local information, are only accurate provided the sampling times are sufficiently long to provide statistically accurate results.

In hot film anemometry, an electronic feedback circuit is used to maintain the sensing element/probe at a constant temperature higher than the surrounding fluid. The output voltage is proportional to the heat transfer from the sensor to the surrounding fluid. Multiphase flow measurements using hot film anemometry exploit the large difference in heat transfer from the sensor to the liquid and gas to discriminate the signal between the two phases. For a sufficiently long observation, the fraction of time the probe detects the gas can be interpreted as the local void fraction (Serizawa, 1974). In order to discriminate the hot film signal into the gas and liquid phases, the dynamic response of the anemometer output to the passage of a gas bubble across the sensor needs to be well understood. For the case of a direct hit on the sensor by a gas bubble, two events must be identified in order to interpret the signal correctly: the points at which the bubble front and back make first contact with the probe (Farrar & Bruun, 1989). Figure 2.3 details a sample hot-film anemometry voltage signal and bubble-probe interaction (Kirouac et al., 1999). The passage of the gas bubble across the sensor corresponds to the time interval

between these two events. In early research, an amplitude threshold was used to discriminate the signal into the gas and liquid phases (Resch et al., 1974; Abel & Resch, 1978; Jones & Zuber, 1978). Data points below the threshold are associated with the gas bubbles, and those points above are associated with the liquid phase. While this method is simple in both concept and application, it cannot correctly identify either of the two events described above. Serizawa et al. (1983) proposed an improved threshold detection technique based on the first time derivative of the signal. Misinterpretation of the signal can, however, occur in this case when film breakage occurs across the sensor. To overcome this, Farrar et al. (1988 and 1995) developed a combined amplitude threshold and slope analysis scheme. It consists of an initial amplitude threshold for bubble detection, followed by a search method to locate the two events associated with the bubble passage. In addition, the optimal amplitude and slope thresholds are determined from the probability density function. Liu and Bankoff (1993a) also developed a combined amplitude and slope threshold phase discrimination scheme using the amplitude, forward and backward slopes of the signal. This method has the advantage of incorporating more of the real physics of bubble-probe interaction. The discrimination techniques usually map the hot film signal into a binary signal representing the two phases (Fig. 2.4). The local void fraction is calculated as the fraction of time the probe is in the gas phase (Farrar et al., 1995). The mean phase velocities can also be estimated from the void fraction distribution and individual phase volume flow rates (Ching et al., 1999a).

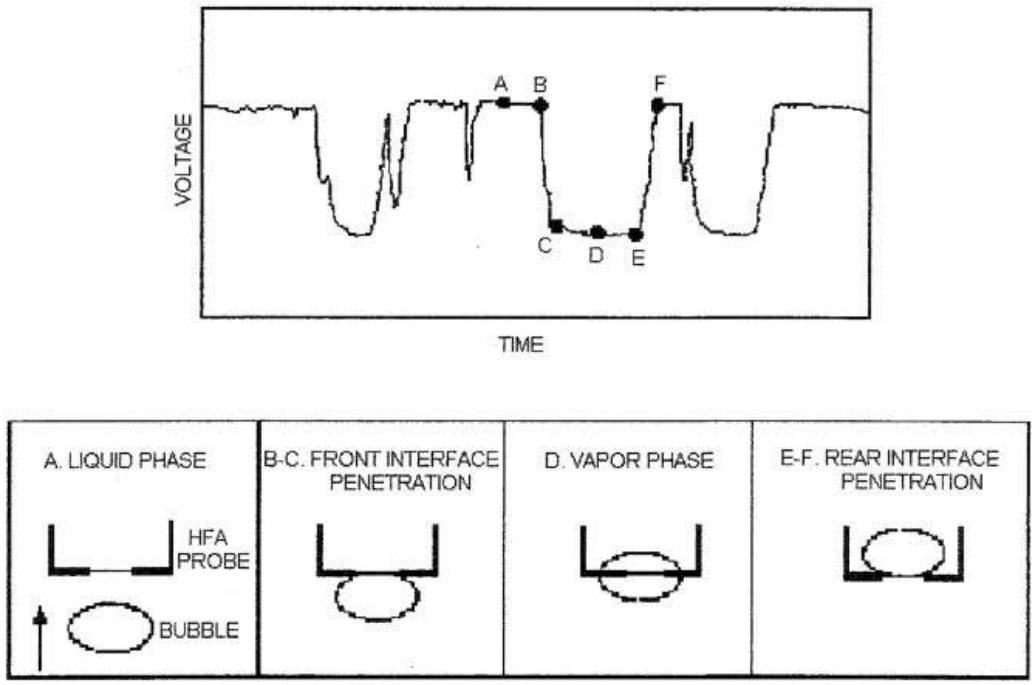

Figure 2.3: Hot-film Anemometry Voltage Signal and Bubble-Probe Interaction in Bubbly Flow (Kirouac et al., 1999)

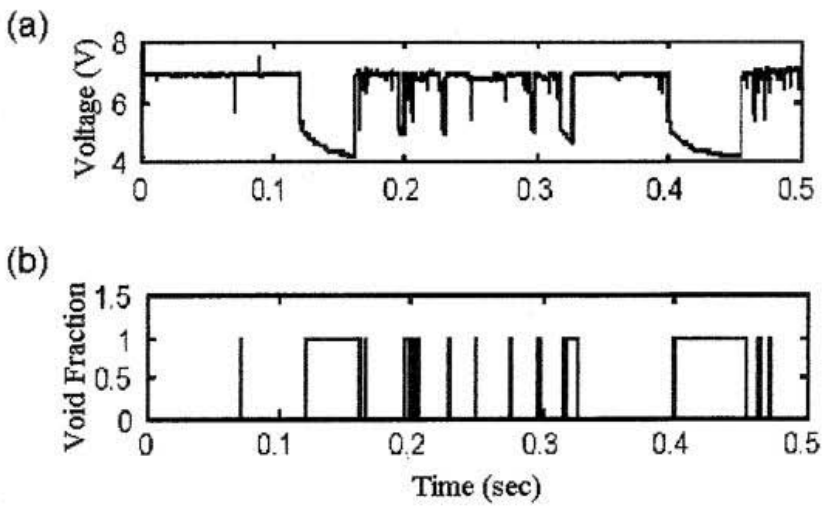

Figure 2.4: Typical Hot-Film Signal in Air-Water Slug Flow: (a) Hot-Film Signal; (b) Void Fraction Function

The principle of two-phase flow measurements by resistivity probes is based upon the difference in conductivity between the gas and liquid phases. The probe yields a two-state signal indicative of the phase because the gas phase behaves like an electrical insulator. Many of the early investigators (Uga, 1972; Herringe & Davis, 1974 and 1976; Serizawa et al., 1987) transformed the original analog signal into a binary data series using a preset voltage trigger level. The accuracy of the trigger level setting directly affects the accuracy of the measurements because of the finite response time of the probe to the gas bubbles. Welle (1985) devised a system using two self-adjusting trigger levels for bubble detection, where the levels are updated according to the last measurement and the minimum and maximum values. Liu and Bankoff (1993b) used a miniature dual-sensor resistivity probe to measure void fraction, bubble velocity and bubble size distribution using an iterative routine of self-adjusted amplitude and slope thresholds for phase identification. The local bubble size and distribution were determined from the measured bubble chord length spectrum based on the statistics of the bubble residence time.

The operation of an optical fiber probe is based on sensing changes in the refractive index of the surrounding medium. In a two-phase flow, the probe is able to discriminate between the two phases only if their refractive indices are sufficiently different. As with other types of intrusive probes, gas bubbles passing the probe are represented by rising and falling slopes on the output signal. Several types of optical probes are available,

however the U-shaped optical fiber probe is generally considered to have the fastest response time due to its small size (Delhaye, 1981). The U-shaped optical probe has a light source and detector (Fig. 2.5). When light reaches the tip of the probe it is forced to either reflect or refract depending on the refractive index of the surrounding multiphase flow. A gas present at the probe tip causes the light to be reflected and a high signal is detected, whereas a liquid present at the tip causes the light to be refracted producing a low signal. Cartellier (1990) and Cartellier and Barrau (1998) investigated the response of various optical probes to the passage of a gas bubble, and introduced the concept of latency length. The latency length is defined as the spatial resolution of the interface detection by a given probe, and can be used as a criterion for comparing various probes. The latency length is calculated as the product of the signal rise time and the interface velocity. By associating the signal rise time with the liquid/gas transition, Cartellier (1992) developed a technique to measure the bubble velocity and size simultaneously using a single optical probe. Moujaes and Sparks (1998) used optical probes at two streamwise locations to obtain profiles of the void fraction, gas velocity, gas bubble diameter and bubble passage frequency in a rectangular channel.

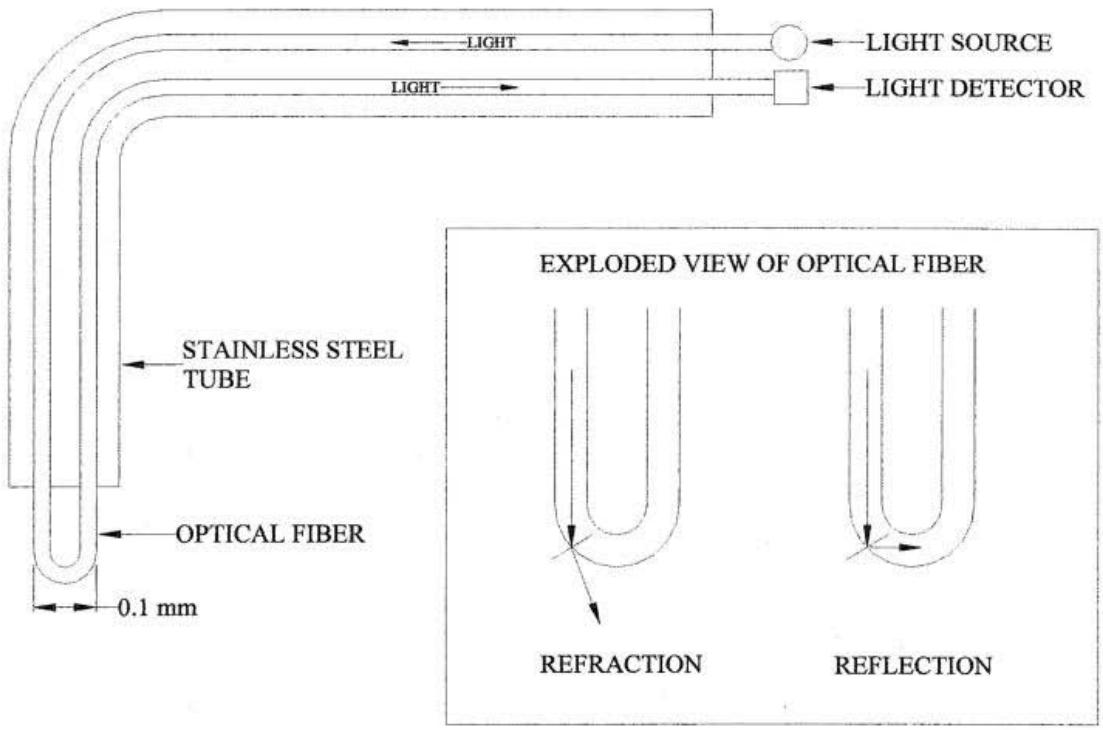

Figure 2.5: U-Shaped Optical Fiber Sensor Probe and its Principle of Operation

2.3 Non-Intrusive Multiphase Flow Measurement Techniques

A significant achievement of recent experimental fluid mechanics is the development of non-intrusive flow measurement techniques. These techniques have the obvious advantage over intrusive techniques of not disturbing the flow. Common non-intrusive flow measurement techniques for multiphase flow include Pulsed Light Velocimetry (PLV), Holography, Laser Doppler Velocimetry (LDV), Nuclear Magnetic Resonance (NMR), Electrical Impedance Tomography (EIT) and Gamma Densitometers. The optical techniques, however, typically involve the addition of reflective seed particles

into the flow. The seed particles are selected to ensure they follow the motion of the fluid and have a negligible effect on the fluid flow properties. In addition, the test section has to be constructed to allow optical access to the flow.

Pulsed Light Velocimetry is a technique that tracks fluid flow by imaging regions of the fluid within the flow field at two or more known times (Adrian, 1991). The PLV measurements yield a collection of Lagrangian vectors describing the fluid motion. Common PLV measurement techniques include Particle Image Velocimetry (PIV), laser speckle velocimetry and Particle Tracking Velocimetry (PTV).

Particle Image Velocimetry is an optical technique for measuring the instantaneous two-component velocity field across a planar region of a seeded flow field (Adrian, 1991). A pulsed laser light sheet is used to illuminate the seed particles entrained in the flow field at two instances in time. The time between the light sheet pulses and either the individual particle displacements or the average displacement of particles over a small sub-region of the recorded image is used to calculate the fluid velocity. In PIV the camera is placed normal to the light sheet so that the dispersed particles scatter light onto the photographic device. Typically autocorrelation or cross-correlation analysis is used to resolve the magnitude and direction of the displacement of the particles between the images. The complete velocity vector field is obtained by analyzing the local velocities in small sub-regions or interrogation areas of the acquired image (Adrian, 1991).

Laser speckle velocimetry makes use of the speckle pattern formed when coherent light is scattered from the surfaces of seed particles (Adrian, 1991). The analysis of these speckle fields became possible only with the development of the Young's fringe method of interrogation (Burch and Tokarski, 1968). An analysis of the fringe pattern spacing and orientation provides the magnitude and direction of displacement respectively. The method statistically compares the speckle fields between two consecutive exposures. Dudderar and Simpkins (1977), Grousson and Mallick (1977) and Barker and Fourney (1977) used the Young's fringe method of interrogation to measure velocity in simple, steady laminar flows.

Particle Tracking Velocimetry uses an extremely low density of seed particles to produce streaks or tracks in each image using either long duration exposures or multiple short duration exposures (Adrian, 1991). Displacement and velocities are determined by tracking individual particles between images or exposures. Velocity measurements by this method has been typically a slow and tedious process but recent advances in computing and camera technology have made this a viable alternative to other methods.

Several hybrid PIV techniques have been developed to study multiphase flows. Gopal and Jepson (1998) developed a novel digital image analysis technique to study the dynamic slug flow characteristics in gas-liquid flows. The flow is recorded using two cameras at right angles to the pipe, and the digital image processing algorithm tracks coordinates of specified points on the image. The slug dimensional characteristics are

determined from the first camera, while slug translational velocity is determined from the second camera. Hay et al. (1998) used a backlighted imaging technique for drop size measurements in annular two-phase flows with small concentrations of drops in the gas phase. A CCD camera, with direct digital image acquisition and an adjustable strobe light source, was used to reduce data collection times and information loss through data transfer. Meng et al. (1995) developed an optical system to obtain shadow-photographs of bubbles in a high-pressure forced convection evaporator tube. The photographs are used to obtain bubble size, velocity and longitudinal position information. Size and velocity information are obtained from multiple exposure images using a measured bubble shift and a timed pulsed light source.

Peterson et al. (1983) and Hawighorst (1983) developed holographic measurement techniques to measure bubble size and velocity. In holography, two-dimensional images are reconstructed to produce a complete three-dimensional hologram. The two-dimensional images were obtained by synchronizing a pulsed laser with a rotating turntable containing photographic plates but recent advancements in camera technology have replaced this technique. Peterson et al. (1983) developed a process of measuring bubble size and position by using an electronic circuit capable of recording two-dimensional spatial coordinates selected on a magnified video screen. The size, position and velocity of a bubble within a viewing volume was determined by selecting coordinates at various locations throughout the image. The method was especially useful for nonspherical bubbles that often pose problems for intrusive probe measurement

techniques. Peterson's technique is best suited to multiphase flow systems with relatively low velocities and low void fractions. Hawighorst (1983) used a technique of digital image analysis to measure bubble size and velocity in a three-phase fluidized bed system. The analysis uses a gradient calculation to determine the outline of each bubble. If a bubble outline results in an open contour, the bubble is eliminated and the remaining bubbles are fitted with a theoretical bounding circle. The theoretical circles are filled and used to determine the individual drop size and drop size distribution. The holographic technique offers the added advantage of obtaining information in three-dimensions. Despite this, holography is often replaced by two-dimensional photographic techniques that are much simpler and more readily achievable for experimental work.

Laser Doppler Velocimetry (LDV), which makes use of the coherent wave nature of laser light and light scattering interferometry, has been used to the study multiphase flows (Bachalo, 1994). The crossing of two coherent laser beams of the same wavelength produces a measurement volume of interference patterns or fringes of high and low intensity light. As particles pass through the measurement volume, the intensity of scattered light varies. The frequency of the scattered light intensity variations is directly proportional to the particle velocity. The scattered light from the particles as they move through the measurement volume is collected by a photodetector. The frequency of the scattered light is referred to as the Doppler frequency of the flow, and is proportional to the velocity component perpendicular to the planar fringe pattern produced by the beam crossing. The advantage of LDV is that it requires no calibration because the velocity

depends only on the laser wavelength and optical setup. To obtain liquid velocity, the signal due to the bubbles crossing the measurement volume must first be removed. Ohba et al. (1987) used LDA to measure the bubble and liquid mean velocities in a square duct two-phase flow.

Nuclear magnetic resonance (NMR) imaging is a recently established non-invasive technique that can be used to study multiphase flow. This technique can provide detailed flow data and reveal significant information about the flow structure of two-phase flow (Lemonnier, 1997). In NMR, a constant high intensity magnetic field is applied followed by two constant gradient fields aligned with the pipe direction. The magnetic field produces a magnetic moment in the fluid on a molecular level and the gradient field helps sensitize the measurements to the axial region of the flow. A radio frequency is used to excite and monitor the response of the fluid while influenced by the magnetic field. This information is used to generate a NMR spectrum that reveals the structure of the fluid flow. Lemonnier investigated the use of NMR in two-phase air-water flows and determined that the technique can provide detailed information on the turbulence of both phases. The technique also produced accurate measurements of the volume fraction, volumetric flux and phase flow rate for each individual phase of the mixture. Despite the requirement for expensive and complex equipment, the NMR technique has significant potential for local phase measurements in multiphase flows

In comparison with NMR, Electrical Impedance Tomography (EIT) is an emerging technology that provides an inexpensive alternative to multiphase flow measurements (Seleghim and Hervieu, 1998). EIT determines the cross-sectional phase distribution according to the variation of the local electrical conductivity of the two phases. The principles of EIT rely on detecting different component conductivities and thus the method can be extended to analyze three phase systems. The reconstruction of the cross-sectional phase distribution from EIT requires the solution of an inverse problem, where the measurements obtained at the periphery of the pipe must be manipulated to produce a cross section profile of the flow pattern. Seleghim and Hervieu (1998) used this method to detect large structures such as slugs and plugs in air-water two-phase flow and some finer details including the wavy or rugged interface in stratified flow. Lemonnier (1997) performed similar work with air-water two-phase flows and found EIT extremely difficult to implement.

Gamma densitometers are generally considered the most practical method for measuring volumetric phase fractions in multiphase flowlines (Lunde et al., 1998). A typical gamma densitometer setup consists of a radioactive source on one side of the test section and a detector on the other side (Fig. 2.6). The beam of photons emitted from the source propagates through the flow and is attenuated differently as it passes through either gas or liquid. The varied attenuation can be measured by the detector and is used to determine the phase fraction in the flow. Lunde et al. successfully used a single energy gamma densitometer to make field measurements in the North Sea. Kirouac et al. (1999) used a

gamma densitometer to obtain line-averaged and cross-sectional averaged void fractions in two-phase flow. The primary limitations of gamma densitometers are long measurement times, limited spatial resolution and near wall measurement difficulty.

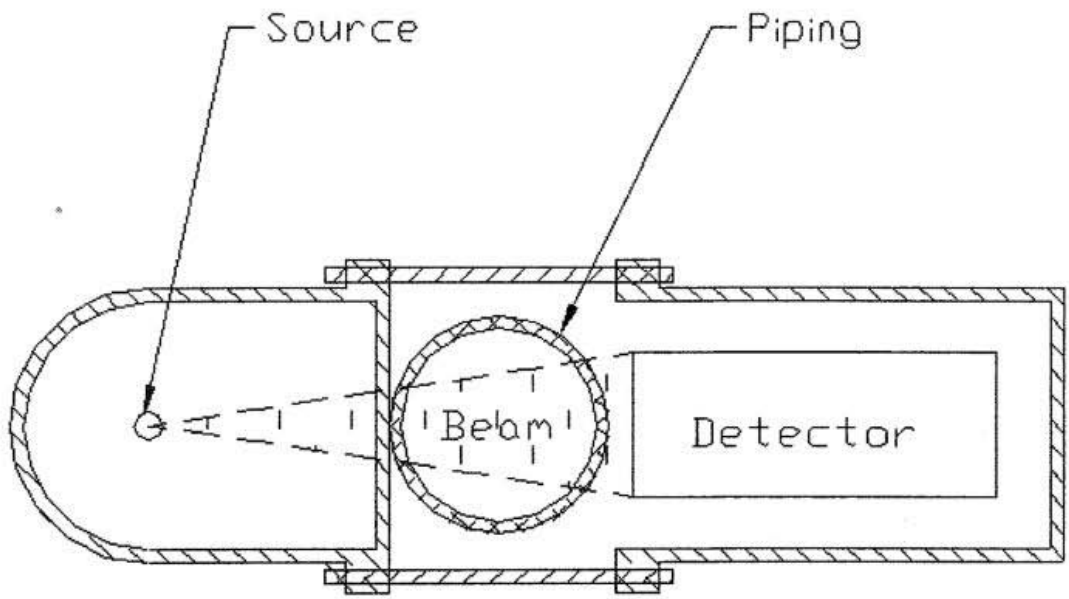

Figure 2.6: Schematic of Gamma Densitometer

Chapter 3

Flow Loop Facility

A new multiphase flow loop facility has been designed and constructed at MUN to investigate oil-water-gas flows (Ching et al., 1998). Two measurement systems are installed in the loop to investigate the different flow regimes: a flow visualization system and a hot-film anemometry system. The major contribution of this research to the flow loop facility was the design and implementation of the flow visualization system.

3.1 Description of the Flow Loop

The loop is designed to generate the different flow regimes characteristic of unprocessed production oil well streams. The loop is constructed to study both horizontal and vertical flows by incorporating clear PVC sections into the flow loop. The flow loop is a 76mm diameter open loop re-circulating system, and has a total length of 65 m. Long radius elbows are used in the construction to minimize flow disturbances and pipe supports are designed to minimize the influence of system vibrations. Figures 3.1 and 3.2 show a pictorial layout and a schematic of the flow loop respectively. The flow loop specifications are detailed in Table 3.1. To facilitate tests with oil-water mixtures, a 750 liter mixing tank and a 630 liter settling/transfer tank are incorporated into the operational section of the loop. The oil-water mixture is transferred between the two tanks using a 1.1 kilowatt centrifugal pump. The liquid is pumped from the mixing tank through the flow loop using a 3.7 kilowatt, 76 mm centrifugal pump. The mixing tank also serves as

a reservoir where the gas (air) can be separated naturally into the atmosphere. A picture of the operational section of the flow loop is provided in Figure 3.3

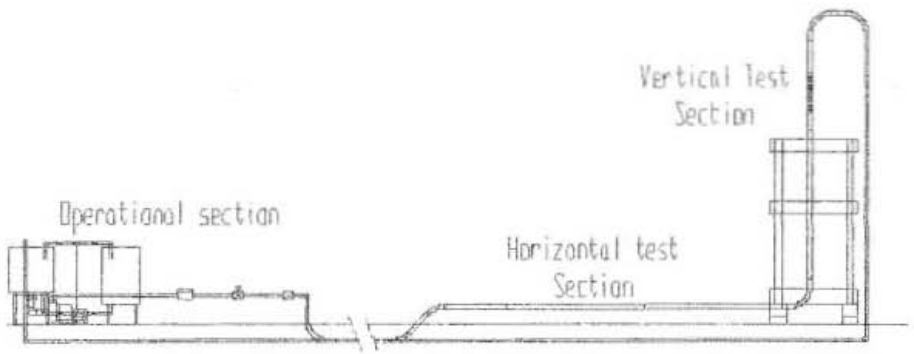

Figure 3.1: Pictorial Representation of the Flow Loop Layout

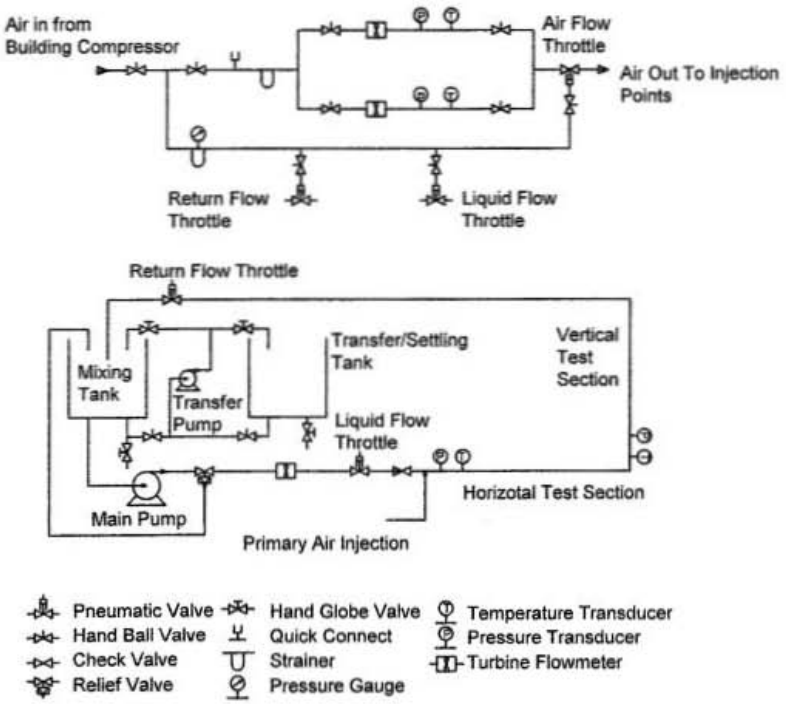

Figure 3.2: Flow Loop Schematic

Table 3.1: Flow Loop Specifications

Item	Specification
Mixing Tank	0.75 m^3
Separation Tank	0.63 m^3
Flow Loop Dimension	76 mm diameter and 65 m long
Horizontal Test Section	6 m
Vertical Test Section	5.5 m
Transfer Piping	38 mm diameter
Liquid Flow Rate	0.6 – 16.4 l/s
Air Flow Rate	21.2 – 3964.2 Standard Liters per minute
Maximum Working Pressure	Max. 414 kPa/60psia
Main Pump	Jacuzzi RSEM3-1 with 3.7kW motor
Transfer Pump	Dynesco with 1.1 kW mootor
Compressed Lines	12.7 mm and 25.4 mm dia. steel pipes

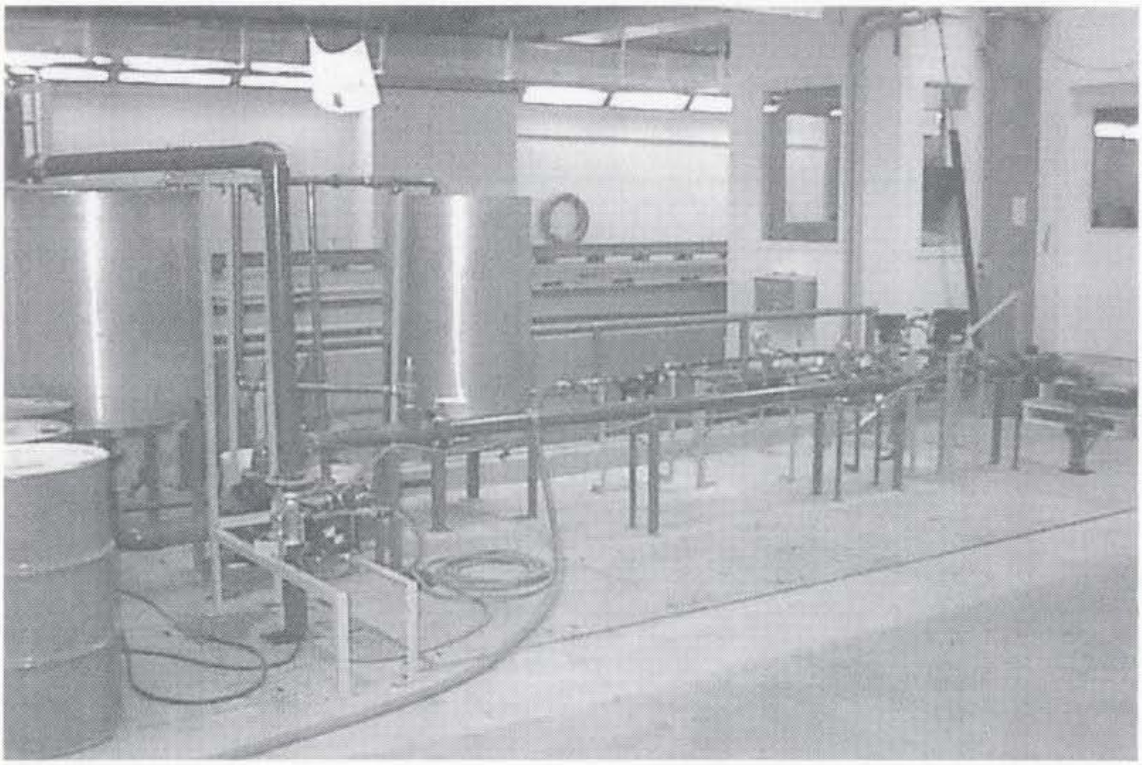

Figure 3.3: Operational Section of Flow Loop

The air is injected downstream of the liquid flow metering section, and separated from the liquid on the return line as it enters the mixing tank. Turbine flow meters are used to measure the individual phase flow rates before the mixing section. Since the MUN flow loop will be used for preliminary testing of the MPFM, accurate instrumentation had to be installed in the loop. A 76 mm turbine flow meter (FTB-730, Omega) is used to measure liquid flow rates and either a 25 mm (FTB-936, Omega) or a 12 mm (FTB-931, Omega) turbine flow meter is used to monitor the air flow rates. Two separate air flow meters are necessary to obtain a good resolution over the entire range of air flow rates required to generate the necessary flow regimes. Figure 3.4 shows a picture of the flow metering section of the flow loop.

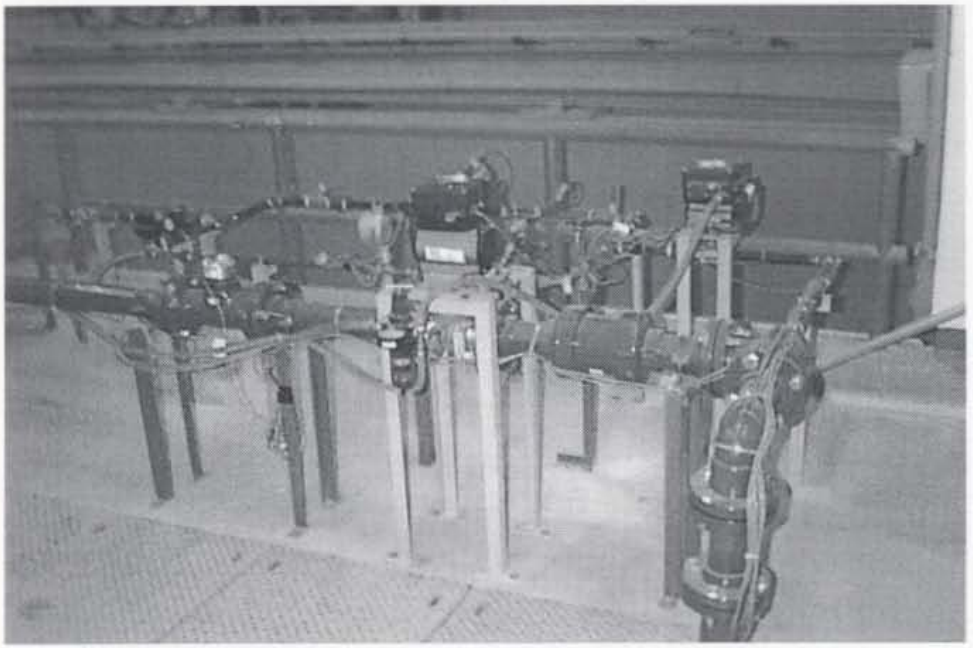

Figure 3.4: Flow Metering Section of Flow Loop

Operational control of the loop is implemented through a fully integrated computer system, which also handles the data acquisition from the flow meters and pressure and temperature transducers. The system consists of a signal conditioner (CYEXP 32 Multiplexor), an analog to digital converter (CYDDA08I), all integrated in a PC. The data acquisition and control is accomplished using the *Labtech Notebook Pro* software. The flow loop control equipment and the measurement equipment for both the hot-film anemometry and flow visualization systems are shown in Figure 3.5. A schematic of the system is given in Figure 3.6.

Figure 3.5: Control Equipment for Flow Loop and Equipment for Hot-Film and Flow Visualization Systems

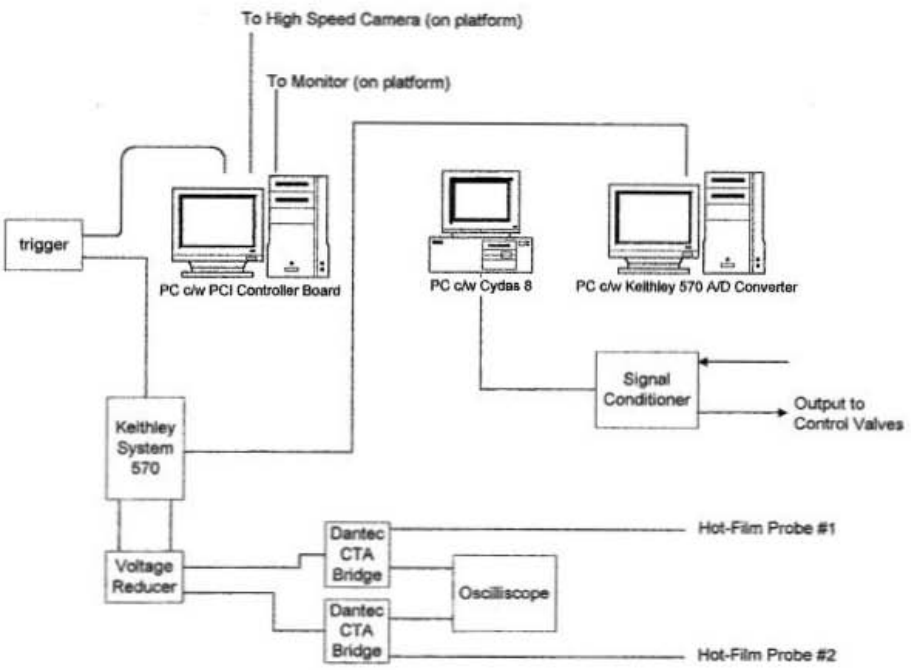

Figure 3.6: Schematic of Flow Loop Control/Data Acquisition and Hot-Film and Flow Visualization Systems

3.2 Flow Visualization System

The test section for the flow visualization is located 50 pipe diameters downstream of the nearest elbow in the flow loop and is constructed of clear optical grade acrylic tubing. The images are obtained using a high-speed digital imaging system and are subsequently analyzed using either a motion tracking or a cross-correlation routine.

3.2.1 Digital Imaging System

The flow images are obtained using a high-speed digital imaging system (MotionScope PCI 1000s) that consists of a CCD camera, PCI interface card and digital image memory

with a maximum frame rate of 1000 frames per second (fps). The camera is mounted on a positioning stand and located on an elevated platform with a remote monitor (Figs. 3.7 and 3.8), while the computer control is located adjacent to the flow loop and hot-film control systems (Fig. 3.5). Complete control of the camera including shutter speed, frame rate and triggering adjustment is facilitated through the PC.

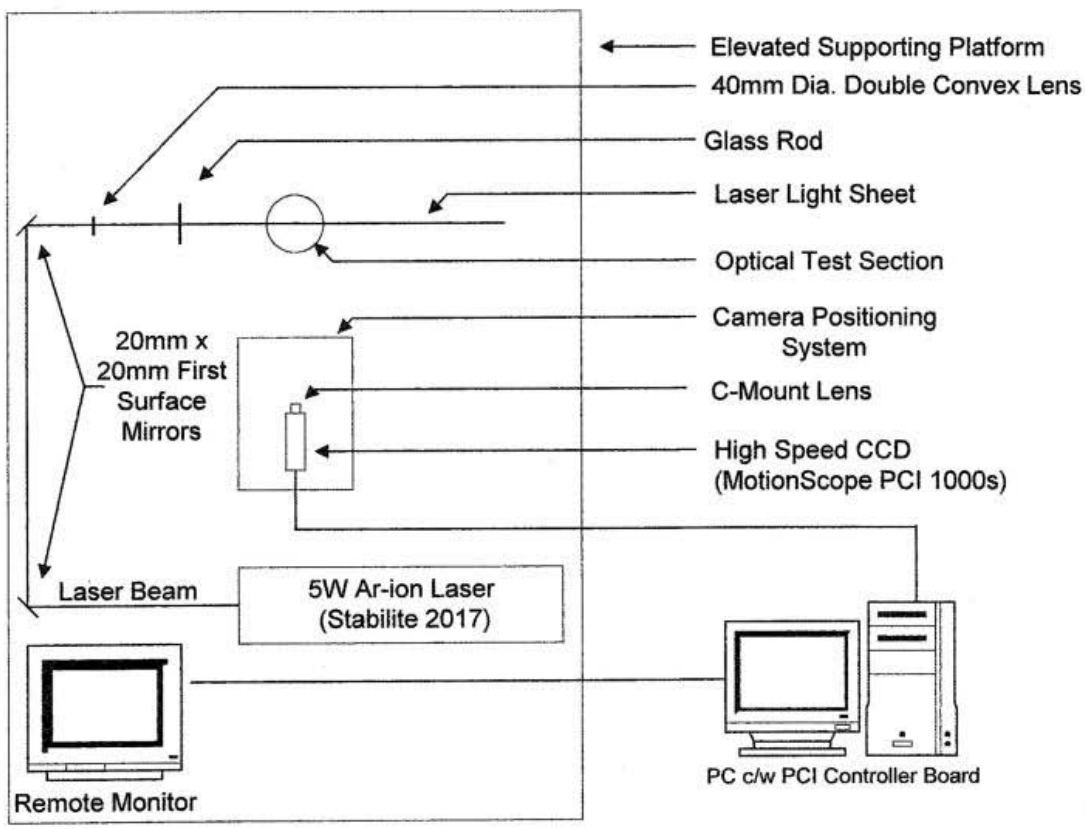

Figure 3.7: Top View of Flow Visualization System

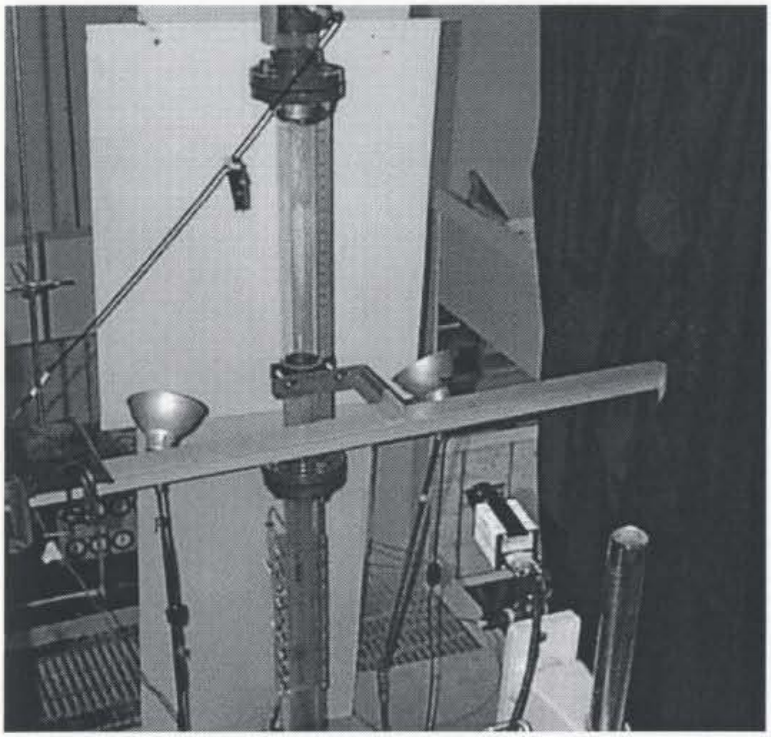

Figure 3.8: Flow Visualization Test Section

The digital imaging system records a sequence of digital images of the flow at a pre-selected frame rate between 60 and 1000 fps, and stores the frames in an image memory on the controller unit. The images can be viewed forward or reverse at pre-selected frame rates (1, 2, 3, 4, 5, 10, 30, 60, 125, 250, 500 or 1000 frames per second), frame-by-frame or freeze frame, to analyze flow motion and time during the sequence. The CCD sensor has a resolution of 656 x 496 pixels with each pixel occupying 7.4 square microns. The electronic shutter operates at rates of 1X to 20X the set recording rate with exposure times shown in Table 3.2. Details of the frame rate, image resolution, number of stored frames and record time are provided in Table 3.3. Although the high-speed imaging

system is capable of recording images at 1000 fps, frame rates of 250 and 500 fps were optimum for the present test flow conditions. With an increase in frame rate, picture resolution is reduced; consequently, it is necessary to optimize the frame rate with the flow conditions.

Table 3.2: Exposure Times for Set Shutter Speeds

Frame Rate	**60**	**125**	**250**	**500**	**1000**
Exposure (s) @ 1X Shutter Speed (sec)	1/60	1/125	1/250	1/500	1/1000
Exposure (s) @ 2X Shutter Speed (sec)	1/120	1/250	1/500	1/1000	1/2000
Exposure (s) @ 3X Shutter Speed (sec)	1/180	1/375	1/750	1/1500	1/3000
Exposure (s) @ 4X Shutter Speed (sec)	1/240	1/500	1/1000	1/2000	1/4000
Exposure (s) @ 5X Shutter Speed (sec)	1/300	1/625	1/1250	1/2500	1/5000
Exposure (s) @ 10X Shutter Speed (sec)	1/600	1/1250	1/2500	1/5000	1/10000
Exposure (s) @ 20X Shutter Speed (sec)	1/1200	1/2500	1/5000	1/10000	1/20000

Table 3.3: Camera Specifications

Frame Rate (fps)	**Resolution (Pixels)**	**No. of Frames Stored**	**Total Record Time (s)**
60	480 x 420	512	8.5
125	480 x 420	512	4.1
250	480 x 420	512	2.0
500	320 x 280	1024	2.0
1000	240 x 210	2048	2.0

3.2.2 Lighting Techniques

A 5W Ar-Ion laser (Stabilite 2017) is used in conjunction with an optic setup to create a laser light sheet for the flow visualization. Space restrictions on the elevated platform necessitate a unique optic setup to create an adequately thin light sheet (Prenel et al., 1989). The optic setup consists of two first surface mirrors, a double convex lens and a glass rod. The two first surface mirrors are mounted at 45° angles to the beam and are aluminized on the surface closest to the incident light thereby minimizing energy loss. The double convex lens is used to converge the beam before it passes through the glass rod to obtain a thin sheet of light. A scale illuminated with a separate point light source, recorded as part of the flow image, is used to calibrate the image pixel resolution (Fig. 3.9).

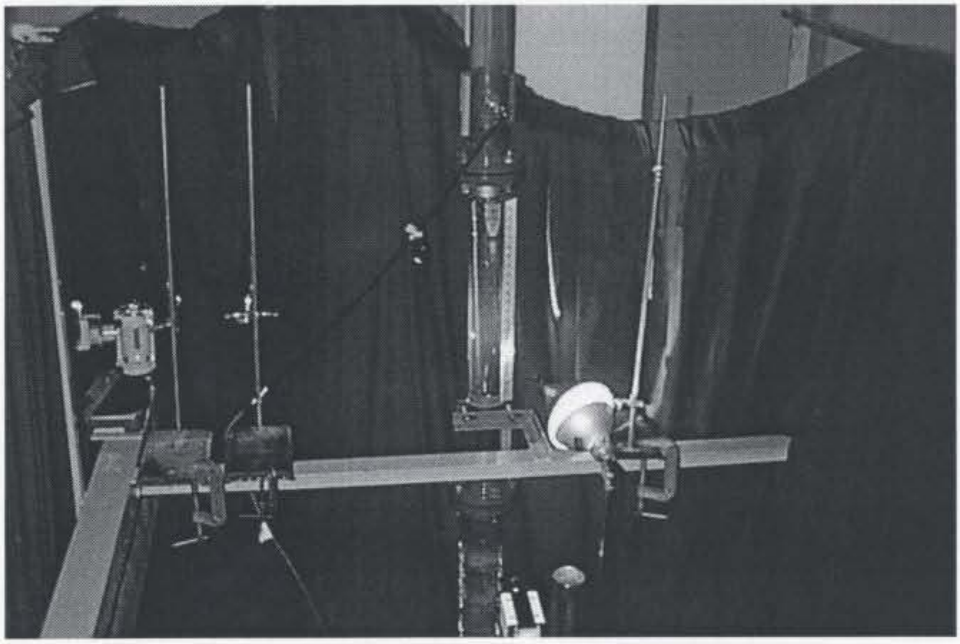

Figure 3.9: Laser Light Sheet and Illuminated Calibration Scale

Images were also obtained using a backlighted technique that consisted of two 500 W halogen photography lamps reflected off a matt finish white screen (Fig. 3.10). Since the entire test section is illuminated, this technique does not require a point light source to illuminate the calibration scale. Lamp position is critical in this technique to prevent shadowing and to ensure optimum image quality.

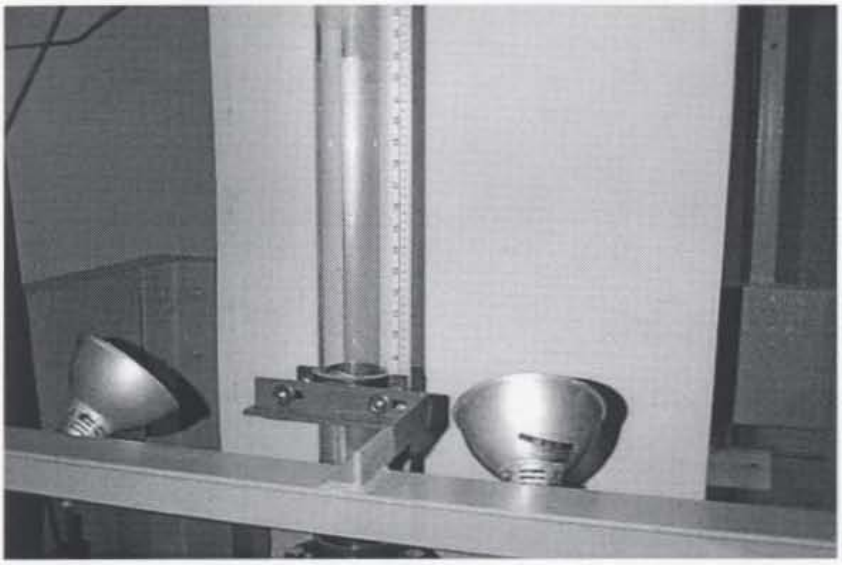

Figure 3.10: Back Light Illumination and Calibration Scale

3.3 Hot-Film Anemometry System

The test section for the hot-film measurements is located immediately upstream of the flow visualization test section (Figs. 3.11 and 3.12). The hot-films are mounted on a traverse that allows the probes to be moved in a radial direction along a diameter of the pipe with an accuracy of ±0.01 mm (Ching et al., 1999b). Heavy-coated cylindrical

DANTEC 55R11 hot-film probes (spaced 18mm apart), operated at an overheat ratio of 1.1 were used with a DISA 55M10 Constant Temperature Anemometer (CTA) system. The hot-film signals are sampled directly at 7000Hz into a dedicated personal computer using a KEITHLEY S570 A/D converter.

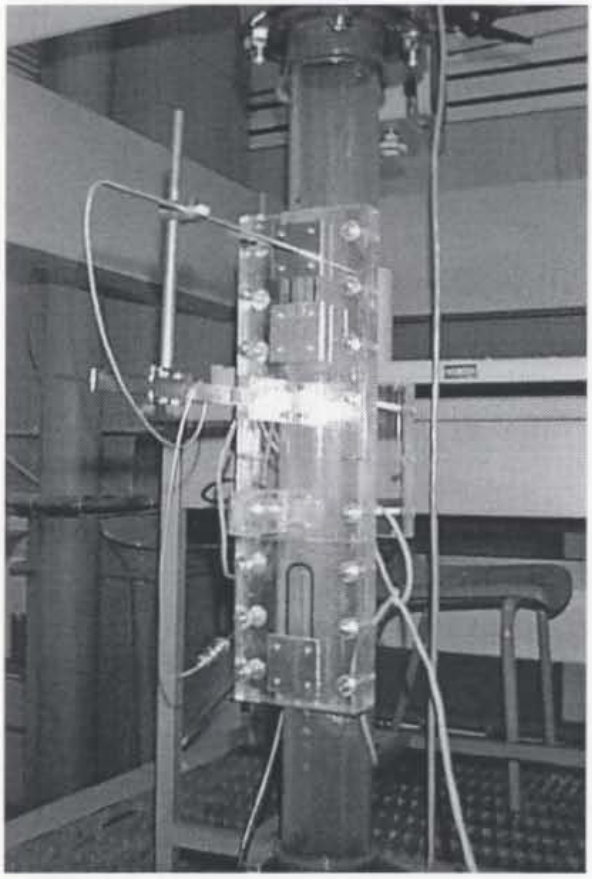

Figure 3.11: Hot-Film Test Section

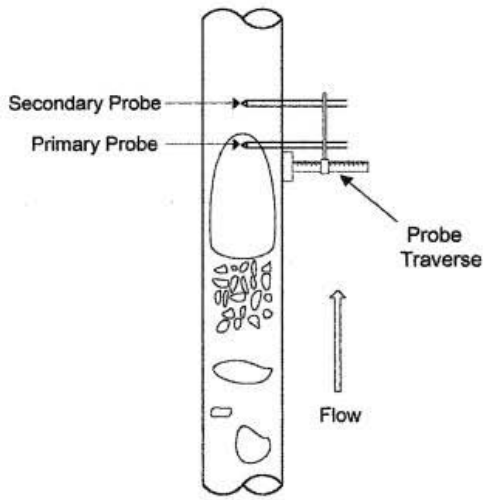

Figure 3.12: Schematic of Hot-Film Probe Setup

3.4 Simultaneous Flow Visualization and Hot-Film Measurements

To obtain simultaneous flow visualization and hot film measurements, a common external trigger circuit with an adjustable time delay on one channel was designed to synchronize the two measurement systems. Upon activation of the hot-film data acquisition system and signal generator, the flow visualization system is triggered after a pre-determined delay. Adjusting the frequency of a square wave from the signal generator controls the time delay. The falling edge of the square wave is used to activate image recording by the flow visualization system (Fig. 3.13). The simultaneous measurements were performed with the camera focused at one of two locations (Fig. 3.14):

1. Camera focused on the flow visualization test section
2. Camera focused on the hot-film probe test section

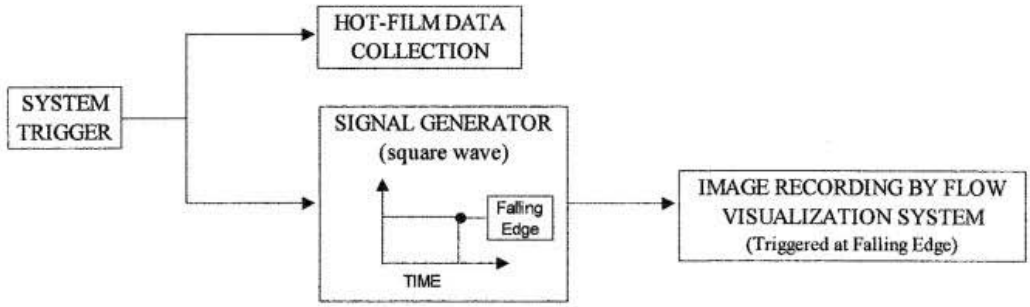

Figure 3.13: Schematic of Trigger Operation

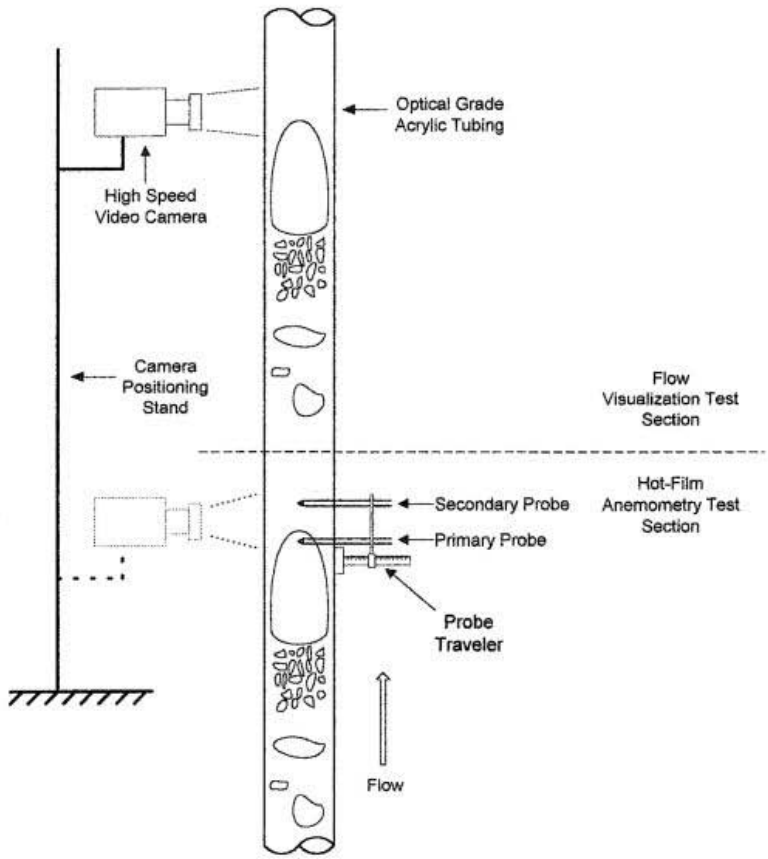

Figure 3.14: Camera Positions for Simultaneous Flow Visualization and Hot-Film Measurements

The majority of the simultaneous flow visualization and hot-film anemometry measurements are performed with the camera focused on the flow visualization test section. This provides a much better quality flow image because the test section is constructed of optical grade acrylic tubing. The major drawback of performing simultaneous measurements in this manner is incorporating the time shift between the two data sets. Although the time shift is initially unknown, the trigger time delay is adjusted based on the flow conditions and the separation between the two measurement systems. The shift in the two sets of data is aligned exactly during post-processing by focusing on key identifiable characteristics of the flow.

The primary purpose of the simultaneous measurements with the camera focused on the hot-film probes is to help understand the relationship between the hot-film and flow visualization data sets. This understanding facilitates data set alignment for the simultaneous measurements with the camera focused on the flow visualization test section. With the camera focused on the hot-film test section, both measurement systems are triggered simultaneously with no time delay. Image analysis is not performed on these images because of the image noise associated with the intrusive nature of the hot-film measurement equipment and the low optical quality of the test section.

Chapter 4

Data Reduction

Two types of image analysis algorithms are used to estimate the gas bubble/slug velocities from the flow images: a supervised motion tracking algorithm and an edge detection cross-correlation algorithm. The supervised motion tracking algorithm was developed in-house at the Multimedia Communications Laboratory (MCL) and the edge detection cross-correlation algorithm was developed as part of this research. A second supervised motion tracking algorithm was provided as a function within the high speed camera software. This software produces similar results to those obtained using the MCL software but requires much less processing time. The camera software is also able to handle the images directly from the recorded avi file as opposed to the individually stored images required by the MCL software. For these reasons the camera software was selected over the MCL software as one method to obtain velocity information from the flow images. There are, however, several disadvantages associated with both supervised motion tracking algorithms:

1. Very laborious and time consuming to obtain quantitative information;
2. Troublesome to process images when bubbles are difficult to distinguish;
3. Difficult to process images when a large cluster of bubbles are present.

To overcome the difficulties of the motion tracking algorithms, a new image processing algorithm based on edge detection and cross-correlation analysis was developed using MATLAB. The edge detection cross-correlation algorithm has the advantage of

removing the subjectivity associated with the supervised motion-tracking algorithm and, in addition, provides bubble size information. This method also provides detailed velocity information over the entire image rather than at selected points. Data reduction methods have also been developed to obtain gas bubble and slug velocities from hot-film anemometry measurements. The hot-film anemometry results are used to validate the flow visualization results. A brief overview of the supervised motion tracking algorithms is presented in Section 4.1 while more detailed descriptions of the cross-correlation algorithm and hot-film data reduction techniques are presented in Sections 4.2 and 4.3 respectively.

4.1 Supervised Motion Tracking Algorithms

The supervised motion-tracking algorithms allow the user to identify the movement of distinguishable gas bubbles and slugs by manually selecting corresponding entity coordinates on consecutive frames of the flow. Gas bubble/slug velocities are estimated using one of two supervised motion-tracking algorithms:

1. Software developed in-house at the Multimedia Communications Laboratory (MCL), titled 'Mesh Tracking';
2. Software developed by the Redlake Imaging Corporation for use with the high speed digital camera.

4.1.1 Mesh Tracking Software

The Mesh Tracking software developed in-house at the MCL requires that corresponding gas bubbles and slugs on consecutive frames of a flow sequence be manually identified by selecting distinguishable points that define the bubble or slug (Cheng, 2000). Figure 4.1 shows the Mesh Tracking user interface for calculating the bubble size and velocities. Gas bubbles and slugs that are being tracked need to be manually selected by placing landmarks on the perimeter of the gas bubbles/slugs on two consecutive frames of a flow sequence. Several landmarks are placed around the perimeter of the bubbles and slugs to improve the accuracy of the velocity estimation. The algorithm segments the identified gas bubbles and slugs using a triangular mesh and tracks the displacement and shape deformation over consecutive frames. The gas bubble/slug velocities are estimated from the displacement and known time step between the frames. Although this algorithm provides an effective method to capture the details of the motion, it is difficult and laborious to accurately determine the corresponding entity coordinates on consecutive frames of the flow (Ching et al., 1999b). This process is also restricted to relatively large distinguishable bubble/slug formations.

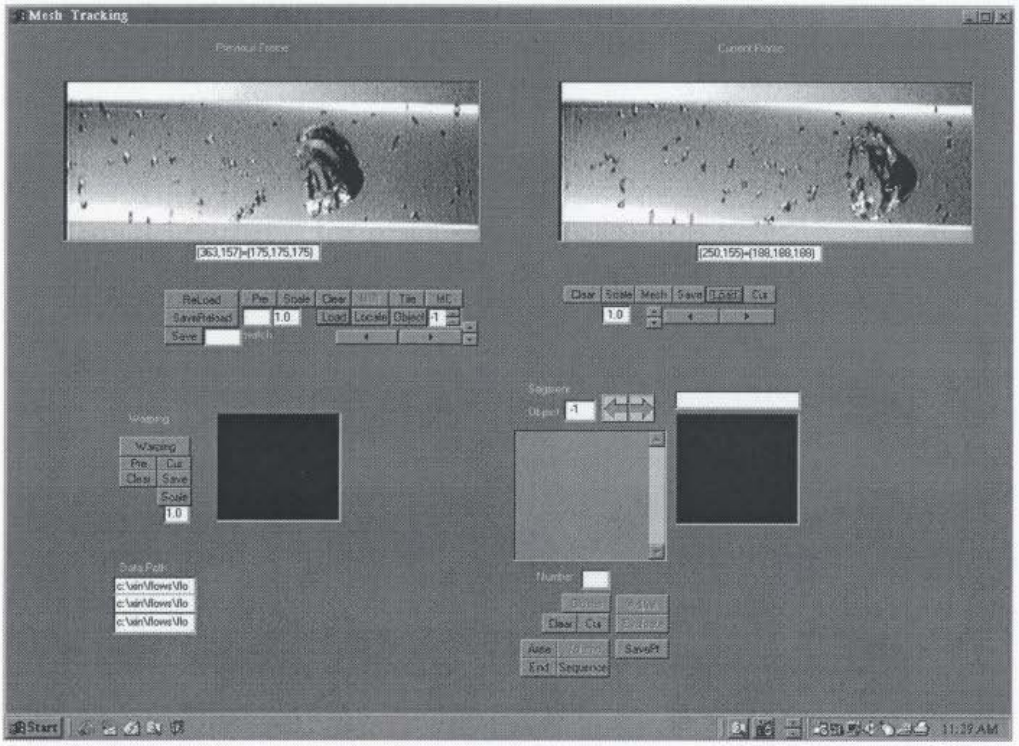

Figure 4.1: Mesh Tracking User Interface

4.1.2 Camera Software

The software included with the high-speed digital camera has a function to measure motion of clearly defined objects (Fig. 4.2). The function allows the user to place reference markers on the defined objects of the recorded video images at points specified with the mouse cursor. For example, the tip of a slug could be identified in ten consecutive frames to determine the displacement of the slug over the ten frames. The function determines the distance between markers and estimates the velocity using the frame rate of the camera. A calibration function is used to convert the displacement in image pixel values to the physical displacement. To calibrate the system accurately the

camera must be positioned perpendicular to the plane of motion and at least two points must be known as a reference for the calibration function. This is achieved by placing a scale in the field of view and using two points on the scale as reference points. Because the system only views the image in two dimensions, the distance and velocity are determined in a plane perpendicular to the camera view.

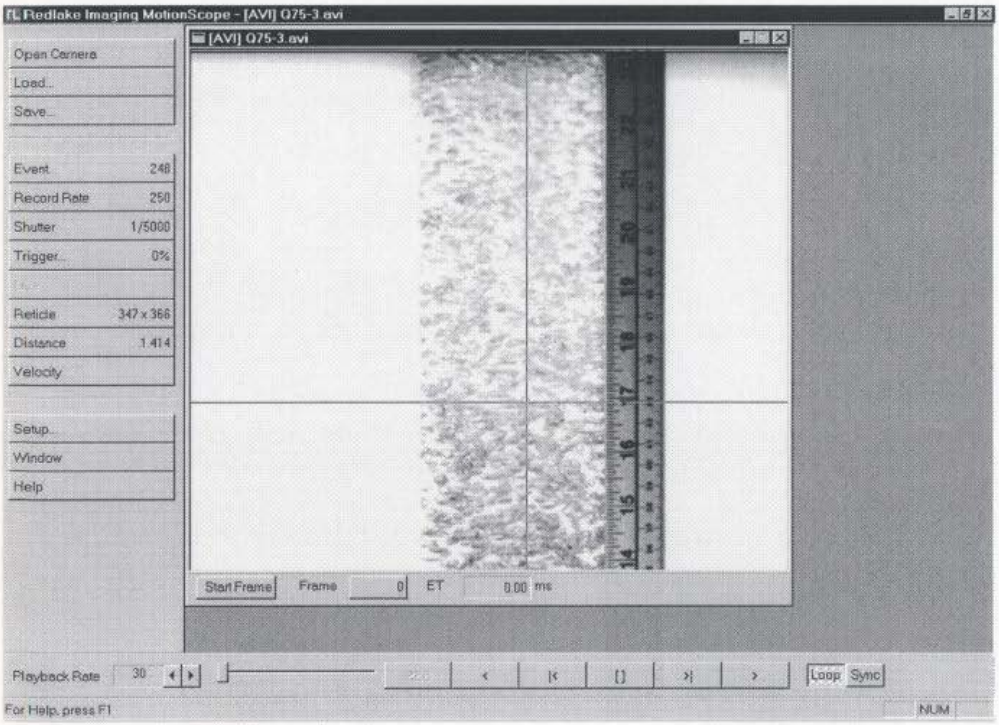

Figure 4.2: Camera Software User Interface

4.2 Edge Detection Cross-Correlation Algorithm

The edge detection cross-correlation algorithm was developed to remove the subjectivity associated with the supervised motion tracking algorithms. It provides detailed bubble velocity information for the entire image by segmenting the image into smaller

interrogation areas. The algorithm defines the boundaries of gas bubbles/slugs and determines size and velocities. The accurate measurement of the gas bubble/slug velocities from this method requires that the bubble/slug features be well defined. The algorithm is developed using standard MATLAB image processing routines and is used on consecutive frames of a flow sequence. The structure of the algorithm follows seven steps:

1. Select image coordinates for cropping and calibration
2. Image enhancement/adjustment as required
3. Determine gas slug/bubble size characteristics
4. Estimate image shift to improve segment match
5. Perform image segmentation
6. Perform cross-correlation to determine displacement of the gas slug/bubbles between consecutive frames
7. Associate a velocity with each bubble size

Figure 4.3 provides an overview of the edge detection cross-correlation routine (a program listing is given in Appendix A). The diagram is structured such that each major block contains a function name followed by a brief description. The cross-correlation function is used to determine the spatial shift of the gas bubbles and slugs between the two images. This function determines the amount of match between two images and is especially amenable to obtaining semi-local measurements by segmenting the image into smaller regions. The image/segment shift, assuming that there is a distinguishable

correlation between the two images, is determined from the location of the cross-correlation peak. The location of the peak indicates the displacement of the bubbles (or distinguishable structures) between the two frames. Details of each function are presented in Sections 4.2.1 to 4.2.6.

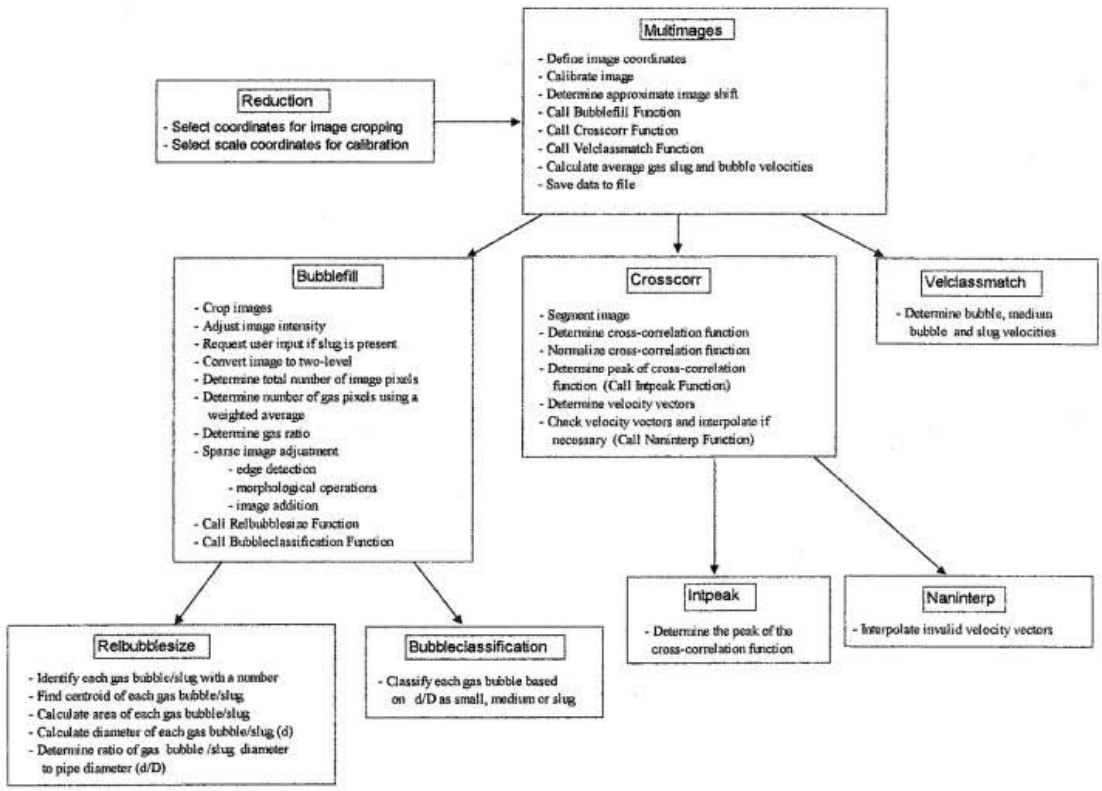

Figure 4.3: Outline of MATLAB edge detection cross correlation routine

4.2.1 REDUCTION Function

The primary purpose of the REDUCTION function is to define the area of the image for the cross-correlation analysis and select coordinates for the displacement calibration.

Two sets of coordinates are required to perform the cross-correlation analysis: image cropping coordinates and scale calibration coordinates. The image cropping coordinates allow unwanted portions of the image that may contain parts of the apparatus or background noise to be removed. These unwanted features are removed by selecting the top left corner and bottom right corner that forms a rectangle encompassing the area of the image required for the analysis. The image area outside of this rectangle is cropped from the original image. The two scale calibration coordinates are selected on the linear scale recorded as part of the flow image. These points are used to convert the image pixel values to a physical distance. To increase the accuracy of the calibration, the two points are selected to have the largest separation possible.

4.2.2 MULTIMAGES Function

The MULTIMAGES function is the main body of the edge detection cross-correlation algorithm. The MULTIMAGES function calls all the other functions and calculates and saves the quantitative information for subsequent post-processing. The input data for the analysis includes a sequence of image frames, segmentation size, camera frame rate, type of lighting (backlighting or laser) and cropping and calibration information obtained from the REDUCTION function.

In order to improve the segmentation and cross-correlation results, the MULTIMAGES function calculates an approximate image shift. The approximate shift is determined by performing a cross-correlation on the first two consecutive images from a sequence using

the full image width. The value of the image shift is used to translate each of the images in the sequence so that during the segmentation process corresponding image segments are aligned as closely as possible. This provides a much better match between the segments and results in a more accurate estimate of the average segment velocity. Without attempting to align the image segments using some prior knowledge of the shift, much of the information in one segment would be shifted to the next higher segment and replaced with information moving upward from a lower segment.

4.2.3 BUBBLEFILL Function

The function BUBBLEFILL is designed to detect and obtain bubble size information for the gas bubbles/slugs. It applies a gamma correction and an intensity adjustment to the image to help highlight slug and bubble characteristics. If a slug is present in the image, the user is asked to indicate its general location by selecting a closed polygon around the slug using the mouse pointer on the image (Fig. 4.4). This helps to alleviate the problem of non-bounded slugs that are incorrectly considered to be part of the liquid phase during cross-correlation. The image is subsequently converted from its original grayscale to a two-level (black and white) image to simplify weighted pixel counting. Figure 4.5 shows the result obtained when the slug region is not manually identified. The slug is represented by a cluster of bubbles rather than a large well defined gas region.

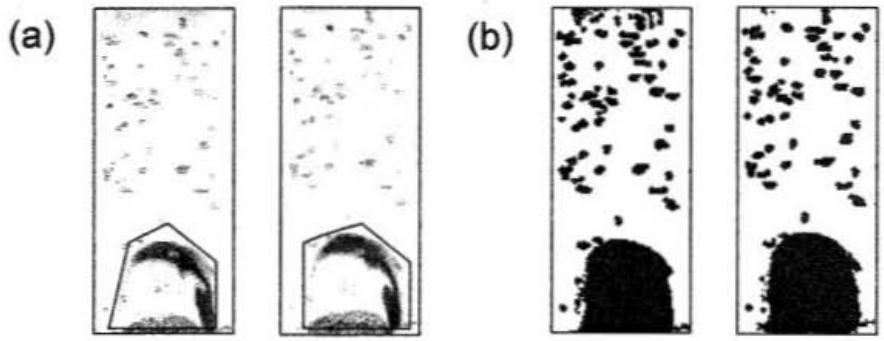

Figure 4.4: Edge Detection Cross-Correlation Algorithm (a) Consecutive Frames with Polygon Bounding Slug; (b) Processed Image

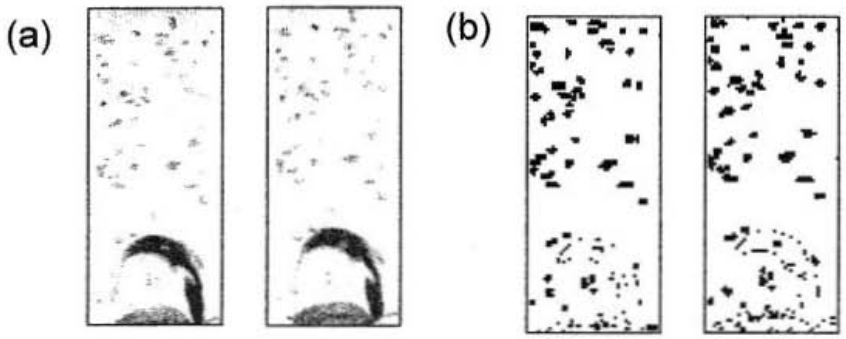

Figure 4.5: Edge Detection Cross-Correlation Algorithm (a) Consecutive Frames; (b) Processed Image without Manual Indication of Slug

Both the total number of image pixels and the number of pixels corresponding to the gas phase are determined for the purpose of calculating the percentage of gas in the image. A method of weighting pixels is performed by the MATLAB function BWAREA to determine the number of pixels corresponding to the gas phase. This function estimates the number of pixels based on their location relative to other pixels. This is especially useful with smaller bubbles that consist of only a few pixels. It helps to smooth the irregular edges of these bubbles and determine a more accurate estimate of the area

corresponding to the gas phase. If the percentage of gas is below a set threshold, which often occurs when gas slugs and bubbles remain as non-bounded regions, an effort is made to improve the gas pixel estimate. In this case, edge detection routines are applied to the images to demarcate bubble and slug boundaries (Fig. 4.6a and b). Morphological operations are then applied to the edge detected images to obtain images with bounded gas regions. Morphological operations are methods for processing binary images based on shapes and are fundamentally neighbor operations that involve adding (dilation) or removing (erosion) pixels from a binary image according to certain patterns or rules. A combination of a dilation operation followed by an erosion operation using the same structuring element is used to close the bubble edges. An iterative morphological operation is used to ensure that each bubble boundary is closed to form an accurate gas bubble/slug region (Fig. 4.6c). As a precaution to ensure that the gas slugs and bubbles have not been oversized an image addition routine is included. This ensures that any black pixels in the adjusted image that do not exhibit some level of grayscale in the original image are removed.

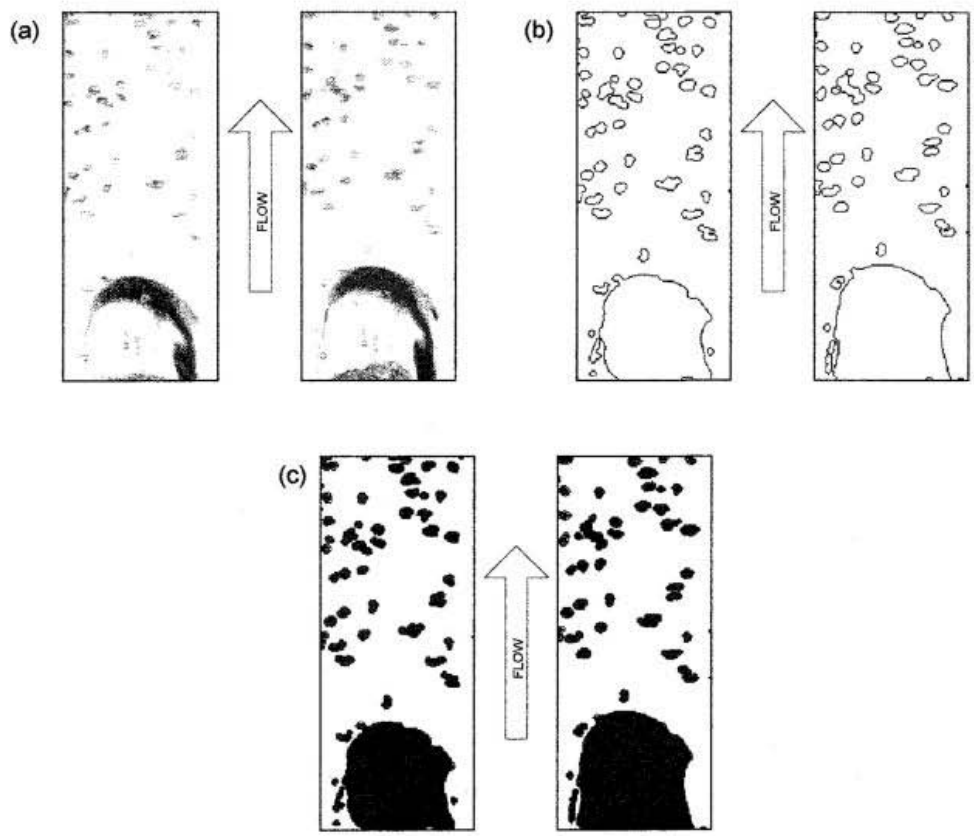

Figure 4.6: Edge Detection Cross-Correlation Algorithm (a) Consecutive Frames; (b)Application of Edge Detection; (c)Application of Morphological Operations

4.2.4 RELBUBBLESIZE and BUBBLECLASSIFICATION Functions

The function RELBUBBLESIZE determines size and position information about the gas bubbles and slugs. This function searches each image for individual gas bubbles/slugs and assigns a unique identifying label (Bubble 1, Bubble 2, etc.). The center of mass (centroid) of each gas bubble/slug is determined as its geometric center based on pixel coordinates. The area of each gas bubble/slug is determined using the weighted pixel

approach described in Section 4.2.3. An estimate for the diameter (d) of each gas bubble/slug is obtained from the area by assuming that each gas bubble/slug has a circular shape. A ratio of the bubble diameter to the pipe diameter (d/D) is used to classify each gas bubble as a small bubble, a medium bubble or a slug according to:

- $d/D \geq 0.5$ Slug
- $0.2 < d/D < 0.5$ Medium Bubble
- $d/D \leq 0.2$ Small Bubble

This classification is used to assign a corresponding average velocity after the image segmentation and cross-correlation is performed. It also provides an indication of the quantity of each bubble size present in the flow image. Table 4.1 shows the bubble size and position information obtained from the analysis of the consecutive frames in Figure 4.6(a). The horizontal and vertical coordinates for the centroid of each bubble are labeled 'xbar' and 'ybar' respectively. These coordinates are measured from the top left corner of the image using the convention that right and down directions are positive.

Table 4.1: Bubble Size and Position Information from the Analysis of Figure 4.6(a)

Bubble No.	xbar (pixels)	ybar (pixels)	Bubble Area (square pixels)	Bubble Diameter (pixels)	d/D	Classification
1	7.19	3.70	84.38	10.36	0.067	Bubble
2	1.56	19.78	9.13	3.41	0.022	Bubble
3	6.27	30.18	77.75	9.95	0.064	Bubble
4	1.00	40.00	1.00	1.13	0.007	Bubble
5	6.29	50.82	67.88	9.30	0.060	Bubble
6	11.12	153.75	182.63	15.25	0.099	Bubble
7	6.26	71.83	76.25	9.85	0.064	Bubble
8	9.07	133.92	91.50	10.79	0.070	Bubble
9	18.51	95.76	154.50	14.03	0.091	Bubble
10	11.83	272.00	36.00	6.77	0.044	Bubble
11	14.52	297.10	162.25	14.37	0.093	Bubble
12	20.96	126.95	100.38	11.30	0.073	Bubble
13	21.08	233.01	102.88	11.44	0.074	Bubble
14	30.94	66.41	391.00	22.31	0.144	Bubble
15	23.95	168.34	100.38	11.30	0.073	Bubble
16	67.80	271.73	8850.88	106.16	0.687	Slug
17	37.50	31.46	75.50	9.80	0.063	Bubble
18	38.37	92.71	85.63	10.44	0.068	Bubble
19	39.26	146.36	88.63	10.62	0.069	Bubble
20	47.00	123.06	88.75	10.63	0.069	Bubble
21	52.34	66.83	95.88	11.05	0.071	Bubble
22	52.44	57.09	92.50	10.85	0.070	Bubble
23	59.98	204.71	83.88	10.33	0.067	Bubble
24	68.55	4.98	90.00	10.70	0.069	Bubble
25	76.26	43.32	111.75	11.93	0.077	Bubble
26	80.43	14.86	142.00	13.45	0.087	Bubble
27	82.75	140.46	205.88	16.19	0.105	Bubble
28	85.51	27.26	137.88	13.25	0.086	Bubble
29	92.68	45.86	108.88	11.77	0.076	Bubble
30	94.79	3.12	45.00	7.57	0.049	Bubble
31	100.54	58.48	147.50	13.70	0.089	Bubble
32	102.26	168.68	133.75	13.05	0.084	Bubble
33	105.32	112.13	94.38	10.96	0.071	Bubble
34	104.19	120.47	94.63	10.98	0.071	Bubble
35	106.79	28.56	77.00	9.90	0.064	Bubble
36	116.54	186.49	172.75	14.83	0.096	Bubble
37	118.20	64.09	137.88	13.25	0.086	Bubble
38	115.81	101.06	89.50	10.67	0.069	Bubble
39	115.81	154.86	59.25	8.69	0.056	Bubble
40	118.70	4.17	56.50	8.48	0.055	Bubble
41	131.27	316.55	11.13	3.76	0.024	Bubble
42	136.50	150.00	6.00	2.76	0.018	Bubble
43	136.50	189.50	4.00	2.26	0.015	Bubble
44	137.00	8.00	1.00	1.13	0.007	Bubble

4.2.5 CROSSCORR Function

The average displacement of the gas slugs and bubbles between two images is determined through the CROSSCORR function. This function incorporates a segmentation routine that allows each image to be divided into smaller interrogation areas to allow velocity estimation in different regions of the pipe. The location of the peak in the cross-correlation function provides the spatial shift of the bubbles between the two areas.

It is important to understand the operation of the cross-correlation function for proper interpretation of the results. MATLAB contains a two-dimensional cross-correlation function that returns the cross-correlation of two matrices with no scaling and has a maximum value when the two matrices are shaped as similarly as possible. Although this function performs an accurate cross-correlation between two images, a much faster version of the function is used in this instance to perform the cross-correlation using the correlation theorem. The correlation theorem states that correlation in the spatial domain is equal to multiplication in the frequency domain of the Fourier transform of the first image with the complex conjugate of the Fourier transform of the second (Jensen, 1999).

In order to obtain accurate information from the cross-correlation function it is necessary to normalize the result and apply a correction to remove any bias error. The cross-correlation function can be normalized by dividing it by the correlation coefficient function; however, to decrease the required calculation time, a first order approximation

is made by dividing the cross-correlation values by the standard deviation of the original image (Jensen, 1999). It is important to note that the flow attributes in one image (or image segment) will be different from those in the next image due to the movement and deformation of the gas bubbles. An attribute at the top of the first image will be shifted off the next image and new attributes will be found at the bottom due to the flow. The degree of change between the two images will vary with changes in flow conditions and camera speed. This shift in flow attributes tends to bias the cross-correlation function, because two identical images are not compared. Since only flow attributes found in both images should contribute to the correlation peak, it is necessary to remove this bias error. Dividing the cross-correlation function by a weighting function reduces the bias error. The weighting function is constructed in Matlab by taking the convolution of two unity matrixes of the same size as the image (Jensen, 1999). A sample cross-correlation plot for the two processed images (Fig. 4.6c) is shown in Figure 4.7.

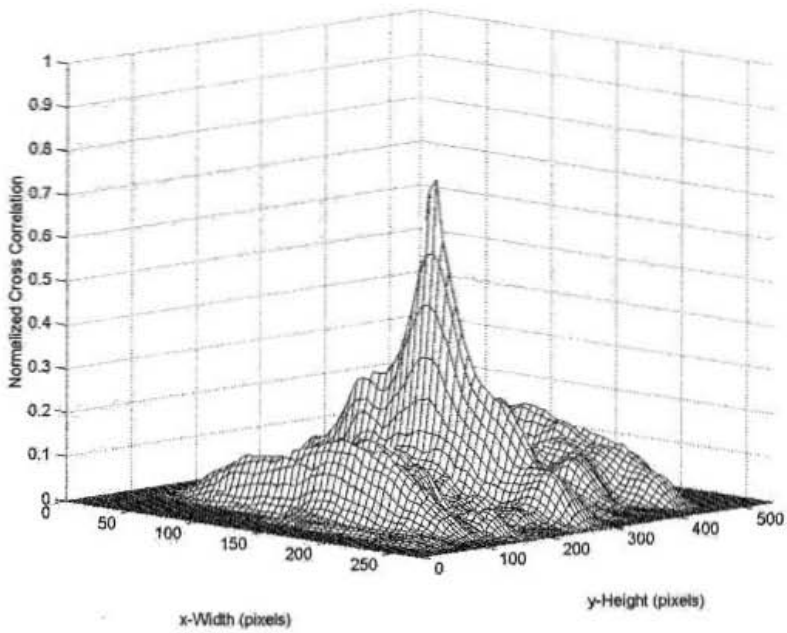

Figure 4.7: Cross-Correlation between Images from Figure 4.6(c)

The location of the peak in the cross-correlation plot corresponds to the displacement of the gas bubbles between the two images. The signal peak is clearly distinguishable from the noise peaks allowing the gas bubble displacement to be estimated. An accurate location of the peak is determined by fitting a three point Gaussian curve using the INTPEAK function. This eliminates the possibility of selecting a point on either side of the peak that may have a correlation value lower than the peak value. The displacement of the peak from the center of the correlation plane provides the horizontal and vertical displacement of the gas bubbles between the two images.

The average velocity of the bubbles in an image is calculated from the displacement and time interval between the two consecutive frames. A velocity vector is determined for each of the segmented regions (Table 4.2) and used to generate a velocity vector plot (Fig. 4.8). To generate this figure the cross-correlation needs to be determined for each of the segmented regions (ie. twenty-one times) because the original image is divided into three vertical and seven horizontal segments. Each velocity vector is representative of the gas velocity in the respective image segment. Any resulting velocity vector not in the dominant direction of flow is automatically replaced by an interpolated value using the NANINTERP function. This function replaces the invalid vectors with interpolated values based on the surrounding velocity vectors. It should be emphasized that these velocity vectors represent the velocity of the gas in each image segment and the VELCLASSMATCH function classifies each of these vectors as a gas bubble, a medium bubble or a slug velocity. Any segment that contains entirely white or black pixels does not show a shift between consecutive images. The value, in this case, of the cross-correlation function is zero and a velocity vector cannot be determined.

Table 4.2: Velocity Matrix showing Segment Velocities (m/s)

Center Coordinates of Segment (pixels)	**22.5**	**67.5**	**112.5**
22.5	0.8343	0.8391	0.8922
67.5	0.9653	0.9107	0.7361
112.5	0.8636	0.8129	0.9315
157.5	0.9676	1.1359	0.7486
202.5	0	0.9310	0.6358
247.5	1.1970	1.2524	1.2472
292.5	1.1436	0	0.2766

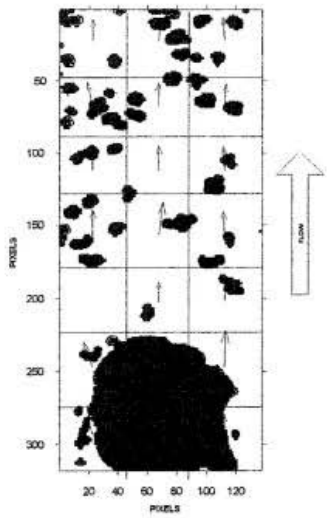

Figure 4.8: Segmentation Grid and Velocity Vector Plot generated using the Cross-Correlation Algorithm

4.2.6 VELCLASSMATCH Function

The VELCLASSMATCH function integrates the gas bubble/slug size and position information of the BUBBLEFILL function with the velocity information of the CROSSCORR function. The function uses the velocity vector matrix (ie. one vector for each image segment) and the coordinates of each vector to associate a velocity with the centroid of each slug and medium bubble. The velocity of either a slug or medium bubble is determined as the average velocity of selected segment velocities surrounding its centroid. Each velocity vector is selected from the velocity vector matrix by assuming that the slug or medium bubble has a circular geometry according to Figure 4.9. Only velocity vectors surrounding the leading edge of the slug or medium bubble are selected for two reasons:

1. The leading edge defines the slug velocity as calculated by the motion tracking and hot-film techniques.
2. The leading edge has a fairly consistent shape as opposed to the turbulent chaotic nature of the trailing edge.

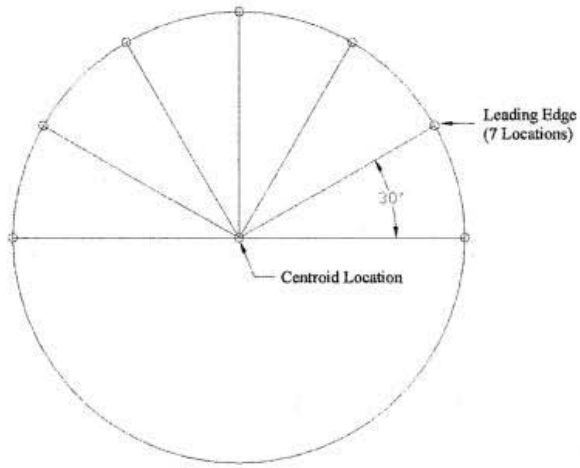

Figure 4.9: Velocity Vector Locations for an Assumed Circular Slug or Medium Bubble Geometry

The centroid and the seven velocity vectors surrounding the leading edge are used to calculate an average velocity for the slug or medium bubble. In the case of the example carried throughout this section, only five velocities are selected (shown in Italics in Table 4.3) due to the segmentation size. If any velocity vector used to calculate the average

velocity exceeds an arbitrary ±30% of the average velocity, the value is removed and the average is calculated again. Section 5.1.2, which describes the results of the edge-detection cross-correlation algorithm, explains why some of the velocity vectors do not accurately represent the slug velocity. These values are discarded in an attempt to better reflect the actual slug velocity. The average of the five selected values in the present example is 1.05 m/s. Only one value falls outside the ±30% threshold (0.6358 m/s), and when removed returns a new average slug velocity of 1.16 m/s. This method requires that the segment size be carefully selected to reflect the bubble/slug attributes of each image sequence. In this example the segment size was selected to be somewhat coarse so that the results could be easily discussed.

Any velocity used in calculating a slug or medium bubble velocity is removed from the velocity vector matrix and the remaining velocity information of the matrix is used to determine an average bubble velocity. In this case the average bubble velocity is determined to be 0.86 m/s. As done when calculating a slug or medium bubble average velocity, small bubble velocity vectors that fall outside an arbitrary threshold are removed and the average is calculated again. In this case the velocity vector 0.2766 m/s is removed because it falls outside an arbitrary ±50% threshold. This threshold is selected to be relatively high so that only very obscure velocity vectors are removed from the matrix. A lower slug threshold is selected because extraneous velocity values often result from performing a cross-correlation between segments that contain large regions of black or white pixels. The new average small bubble velocity is 0.91 m/s.

Table 4.3: Velocity Matrix (m/s) with Selected Slug Velocities (as per Figure 4.9) shown in Italics

Center Coordinates of Segment (pixels)	22.5	67.5	112.5
22.5	0.8343	0.8391	0.8922
67.5	0.9653	0.9107	0.7361
112.5	0.8636	0.8129	0.9315
157.5	0.9676	1.1359	0.7486
202.5	0	*0.9310*	*0.6358*
247.5	*1.1970*	*1.2524*	*1.2472*
292.5	1.1436	0	0.2766

4.3 Hot-Film Data Reduction Technique

A dual-probe hot-film anemometry technique has been developed to measure multiple gas bubble velocities corresponding to different gas bubble size groups in gas-liquid flows. A data reduction scheme using wavelet analysis combined with a phase detection technique is used to discriminate the hot-film anemometer output signals into signals corresponding to different bubble size groups. The phase and bubble size discrimination is based on the magnitude and first time derivative of the signal, and the streamwise length of the gas slugs and bubbles. A cross-correlation between the discriminated signals from the two probes yields the time-difference-of-arrival of the gas bubbles at the two sensor locations. The velocities are estimated from the distance between the sensors and the time-difference-of-arrival. The streamwise length of the bubble is estimated from the velocity and the time duration the sensor is in the gas bubble. The bubble size distribution is obtained by summing the bubbles of each size group present in the output signal.

4.3.1 Data Reduction

Multiple velocities corresponding to different slug/bubble size groups can be estimated from the hot-film output signals through selective discrimination of the signals to reflect the different bubble size groups. The principle of this technique is illustrated schematically in Figure 4.10, and is performed in five steps:

1. Signal decomposition using wavelet transforms to remove high-frequency signal noise.
2. Identification of gas slugs and bubbles using an amplitude and first time derivative of the signal.
3. Discrimination of the signal into signals corresponding to different bubble size groups.
4. Cross-correlation of the discriminated signals from the two sensors to obtain the time-difference-of-arrival of the gas bubbles at the sensor locations.
5. Estimation of velocities and bubble size from time-difference-of-arrival and distance between the sensors.

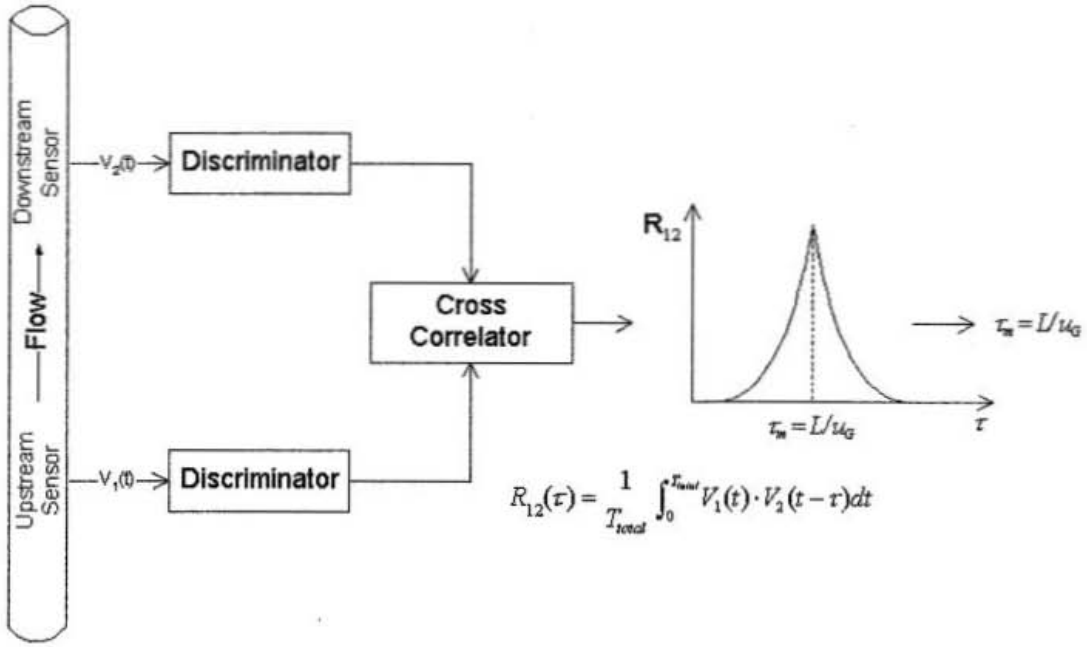

Figure 4.10: Schematic of Velocity Estimation Procedure

4.3.2 Wavelet Signal Decomposition

The passage of a gas slug/bubble over the hot-film is accompanied by a sudden decrease in the output voltage because of the reduced heat transfer from the sensor to the fluid. A slug is distinguished by a longer and deeper trough in the output trace, compared to that of a bubble (Fig. 4.11a). Intuitively it may seem plausible that the signal could be suitably band-pass filtered to elicit the distinguishing features of the slugs and bubbles and remove the signal noise. However, classical Fourier filtering techniques are not suitable in this case, because of the different phase shifts it imposes on the various frequency components. Consequently, the cross-correlation will not reflect the true time shift between the filtered signals.

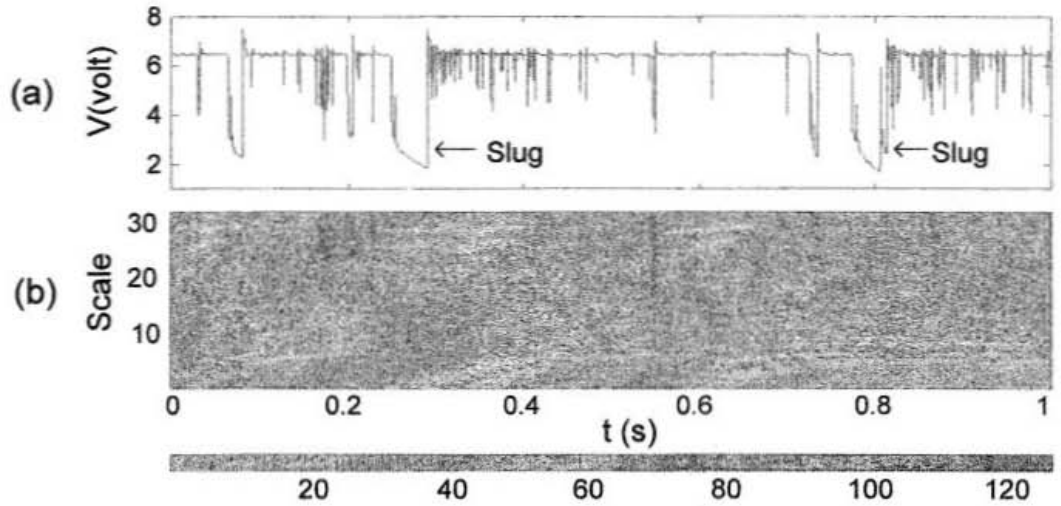

Figure 4.11: Typical Hot-film Signal and Wavelet Transformation: (a) Hot-Film Signal; (b) Wavelet Transformation Plot

Wavelet transforms can be used effectively in this instance to remove the high-frequency noise and facilitate the phase detection. Wavelet transforms are especially useful to analyze non-stationary signals, as in the case of slug flow, because of its ability to preserve both the time and frequency information (Graps, 1995); hence, accurate temporal localization of each event is possible. In addition, a multi-resolution analysis (MRA) allows the signal to be analyzed at different frequencies with different resolutions. Consequently, it is well suited for signals with high frequency components for short duration and low frequency components for long duration. In wavelet analysis, a wavelet prototype function, called mother wavelet, is used to decompose the signal into a scaled and shifted version of the mother function. The temporal analysis is performed with a contracted, high frequency version of the mother wavelet, while frequency analysis is performed with a dilated low frequency version of the same wavelet.

The hot film output signal is first decomposed using a fifth order Symlet wavelet function to facilitate the extraction of the slugs and big bubbles. The fifth order Symlet wavelet function is selected as the mother function because it has a similar profile to that of the slug/bubble (Fig. 4.12). The wavelet decomposition represents the signal as the superposition of the scaled and shifted versions of the mother function. A continuous wavelet transform yields localized frequency information of the hot-film output. The mother function is translated over the time domain and dilated over a range of scales. In this manner, wavelet coefficients are calculated for the scales at each time location of the signal. The wavelet transform plot corresponding to the hot-film signal is presented in Figure 4.11b. It indicates the time localized frequency content of the signal and can also be interpreted as the time series record of the signal frequency (or scale). The magnitudes of the resulting coefficients are reflected through gray level scale as indicated. Figure 4.11b shows that the passages of slugs and bubbles are associated with a substantial frequency change at these instances. Such characteristics can be used to localize the occurrences of those events. For example, the passage of slugs at 0.248 and 0.772 seconds are precisely reflected in the wavelet transform plot at the same temporal locations. The wavelet decomposition is also used to remove the high frequency noise in the signal. Figure 4.13 show levels two and three of the wavelet decompositions of the hot-film signal. While the time information of the local events is well preserved at both levels, the high frequency components are progressively removed. The number of levels for the decomposition is based on the nature of the signal, and is selected to ensure that any component of the signal due to the bubbles is not removed.

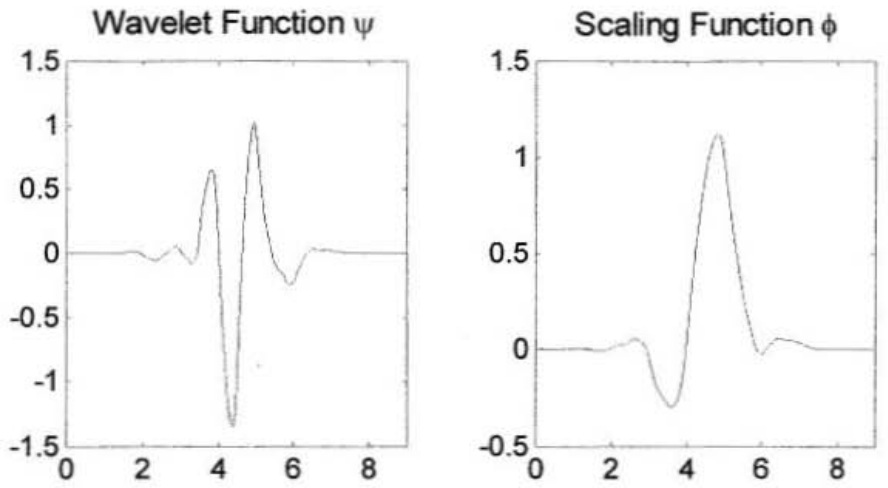

Figure 4.12: Fifth Order Symlet Wavelet Mother Function and Scale Function

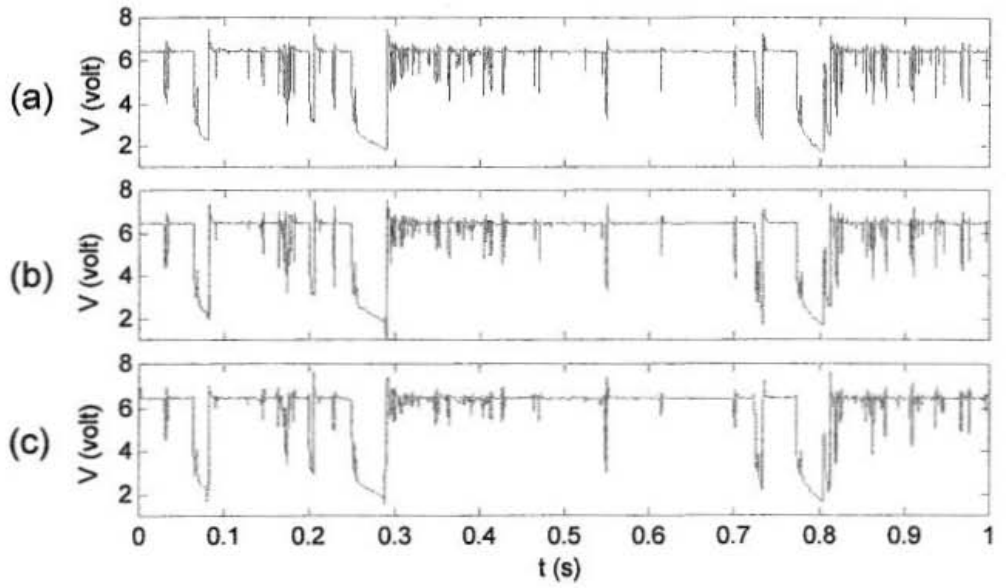

Figure 4.13: Hot-Film Signal and Corresponding Wavelet Decomposition Approximations: (a) Original Hot-Film Signal; (b) Level Two Wavelet Approximation; (c) Level Three Wavelet Approximation

4.3.3 Bubble and Slug Extraction

A combined amplitude and first derivative threshold technique is applied to both the original output signal and the level three approximation to estimate void fraction and detect the slugs and bubbles. The amplitude threshold is calculated using the signal amplitude probability density function (Farrar et al., 1995). Once the intersection points of the signal with the threshold are located, a backward searching scheme is used to locate the front and back of the bubble in the signal. The sign change of the first order time derivative of the signal is deemed to be associated with the event occurrences, and is used as the criteria to detect the two events. This was found to be superior to using a threshold of the first order time derivative. The resulting phase indicator function (Figure 4.14) precisely indicates the temporal locations of the slugs and bubbles. The events associated with very small bubbles are not captured by this scheme. This is expected since the interest is in slugs and big bubbles at this stage. The signal corresponding to the very small bubbles is recovered by removing the slugs and big bubbles from the original signal.

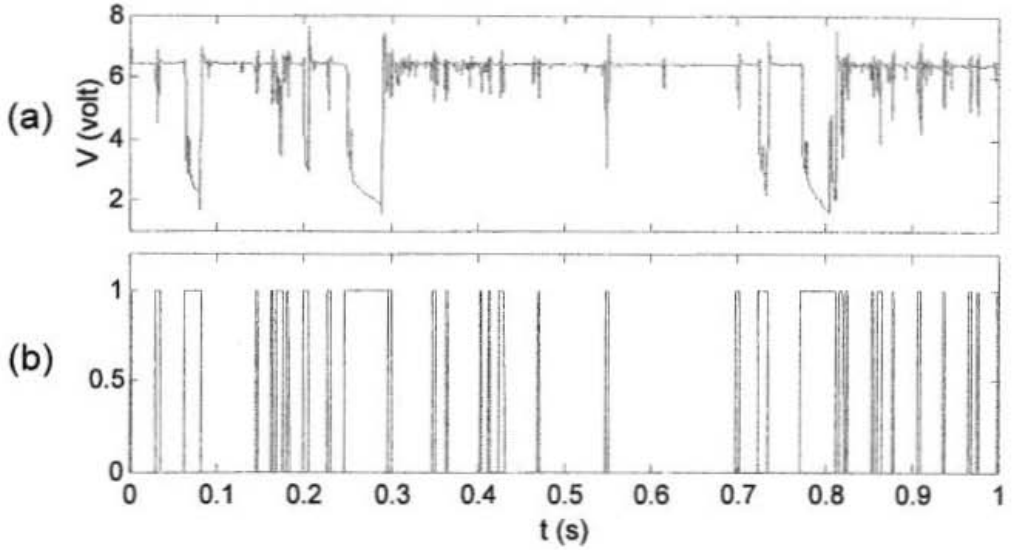

Figure 4.14: Wavelet Approximation and its Phase Indicator Function: (a) Level Three Wavelet Approximation; (b) Phase Indicator Function

In the current study, two velocities corresponding to two bubble size groups have been estimated. The discrimination scheme is based on the slug and bubble streamwise dimension, which is estimated as the product of an average velocity calculated from the original signals and the time duration the slug/bubble is in contact with the probes. The bubbles are delineated as slugs if $L/D \geq 1/3$ and bubbles otherwise, where L and D are the streamwise length of the bubble and diameter of the pipe, respectively. Typical signals corresponding to the slugs and bubbles extracted from the original output signal are shown in Figure 4.15. These representative signals clearly show that it is possible to extract the signal due to different bubble size groups using the method outlined above. The decomposition of the signals allows estimation of velocities of each bubble size group.

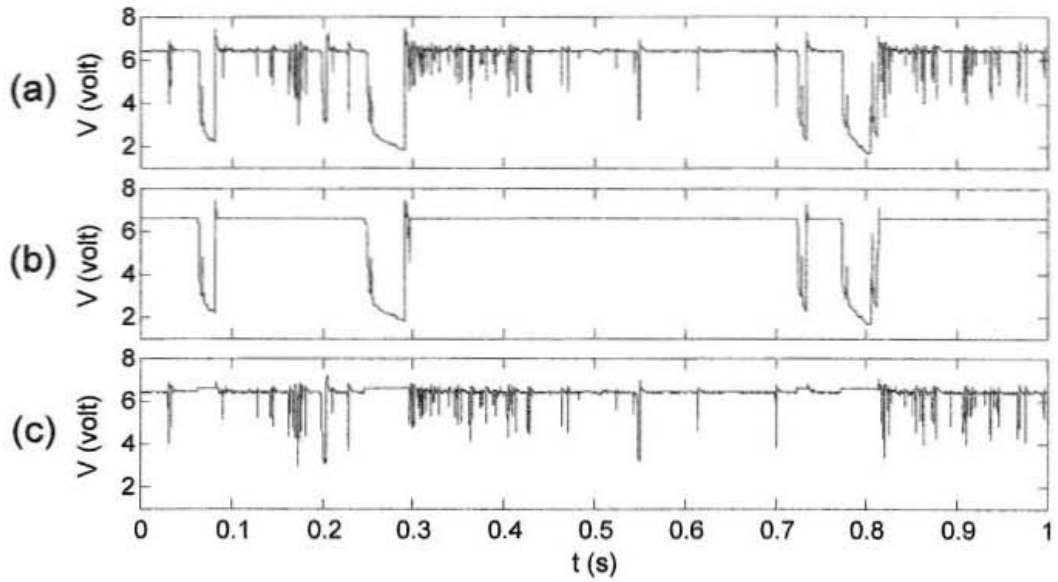

Figure 4.15: Separated Slug and Bubble Signals: (a) Original Signal; (b) Slug Signal; (c) Bubble Signal

4.3.4 Bubble Velocity and Size Estimation

The time-difference-of-arrival of a particular bubble size group is obtained through a direct cross correlation of the discriminated signals from the two probes. The cross-correlation function has a sharp peak (Figure 4.16), which makes it easy to determine the time delay τ. The velocity is estimated using the distance l between the probes and the time delay τ. The peak value of the cross-correlation function is about 0.98, indicating that the signal does not change much over the distance between the probes. The streamwsie length of the slug/bubble groups is calculated from the estimated velocity and the time duration of the slug/bubble passage over the probe. The physical interpretation of the velocities is much easier when they are associated with the bubble size

distributions. This should facilitate the development of physically plausible mechanistic models of the flow.

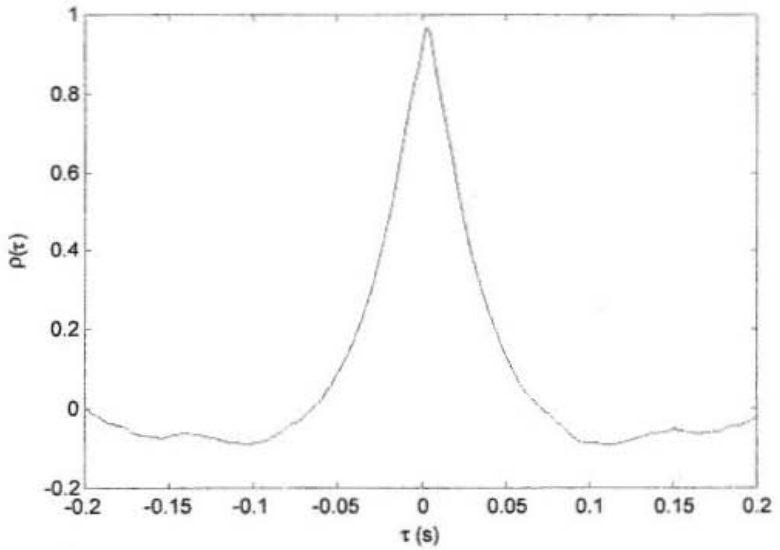

Figure 4.16: Typical Cross Correlation Function

Chapter 5

Results and Discussion

Measurements were performed for vertical-up slug flow with different gas and liquid flow rates. The test conditions are given in Table 5.1 and are hereafter referred to by the case letter. The superficial phase velocity is the flow velocity of one phase of the multiphase flow, assuming that the phase occupies the entire cross-section of the pipe. Several sequences of flow images, using the backlighting technique, were recorded for each flow condition or case and are distinguished with a number following the case letter (eg. A-1, A-2, etc.). For each case, the liquid flow rate was pre-selected and the corresponding gas flow rate was adjusted to obtain a dominant slug flow condition. Section 5.1 details the flow visualization results obtained using both the motion tracking and cross-correlation routines. Section 5.2.1 highlights the dynamic response of the hot film probe to the passage of a gas slug and Section 5.2.2 reviews the results of the simultaneous flow visualization and hot-film anemometry measurements.

Table 5.1: Test Conditions

Test Case	Liquid Flow Rate (gpm)	Gas Flow Rate (CFM)	Liquid Superficial Velocity, U_L (m/s)	Gas Superficial Velocity, U_G (m/s)
A-(1-4)	30	1.5	0.40	0.15
B-(1-4)	50	1.5	0.66	0.15
C-(1-5)	100	1.8	1.32	0.18
D-(1-5)	125	1.8	1.65	0.18
E-(1-5)	150	1.8	1.98	0.18
F-(1-5)	100	2.4	1.32	0.24

5.1 Flow Visualization Results

The slug and bubble velocities obtained using the supervised motion tracking and the cross-correlation algorithms are average velocities determined from four consecutive frames of the flow sequence. Four frames are chosen to calculate an average velocity because of computer processing time, memory and storage limitations when using the MATLAB cross-correlation algorithm. Table 5.2 indicates the camera recording parameters and lighting technique for each test case.

Table 5.2: Camera Recording Parameters

Test Case	Frame Rate (fps)	Shutter Speed	Lighting
A-(1-4)	250	1/5000	Back Lighting
B-(1-4)	250	1/5000	Back Lighting
C-(1-5)	250	1/5000	Back Lighting
D-(1-5)	250	1/5000	Back Lighting
E-(1-5)	500	1/7500	Back Lighting
F-(1-5)	250	1/5000	Back Lighting

5.1.1 Motion Tracking Algorithm Results

The slug and bubble velocities obtained using the supervised motion tracking algorithm are velocities of slugs and bubbles selected manually using the mouse cursor. The bubbles are manually selected to be readily identifiable over four consecutive frames of the flow and to capture details of the velocity near the pipe wall, close to the slug and at the center of the pipe. The location of each point selected to represent a gas bubble/slug

is included with the motion tracking results as x and y coordinate values. These values can be used to locate the position of each gas bubble and slug as identified in Figure 5.1. The tip of the line for each callout in the figure represents the point selected using the mouse cursor on the fourth image for each selected test case. Each image of Figure 5.1 has a unique appearance because of variations in slug geometry and variations in the liquid and gas velocities. The density and orientation of the gas bubbles also affect the appearance of each image, because of variations in the amount of reflected light.

A sample of the results obtained from the motion tracking algorithm for each test case is presented in this section. The results of the motion tracking algorithm are presented in tables that contain position and velocity information for each bubble/slug tracked over the four frames. Tables 5.3 to 5.8 detail the velocity results for Cases A-1, B-1, C-3, D-3, E-2 and F-4, respectively. The results of the remaining test cases are summarized in a subsequent section.

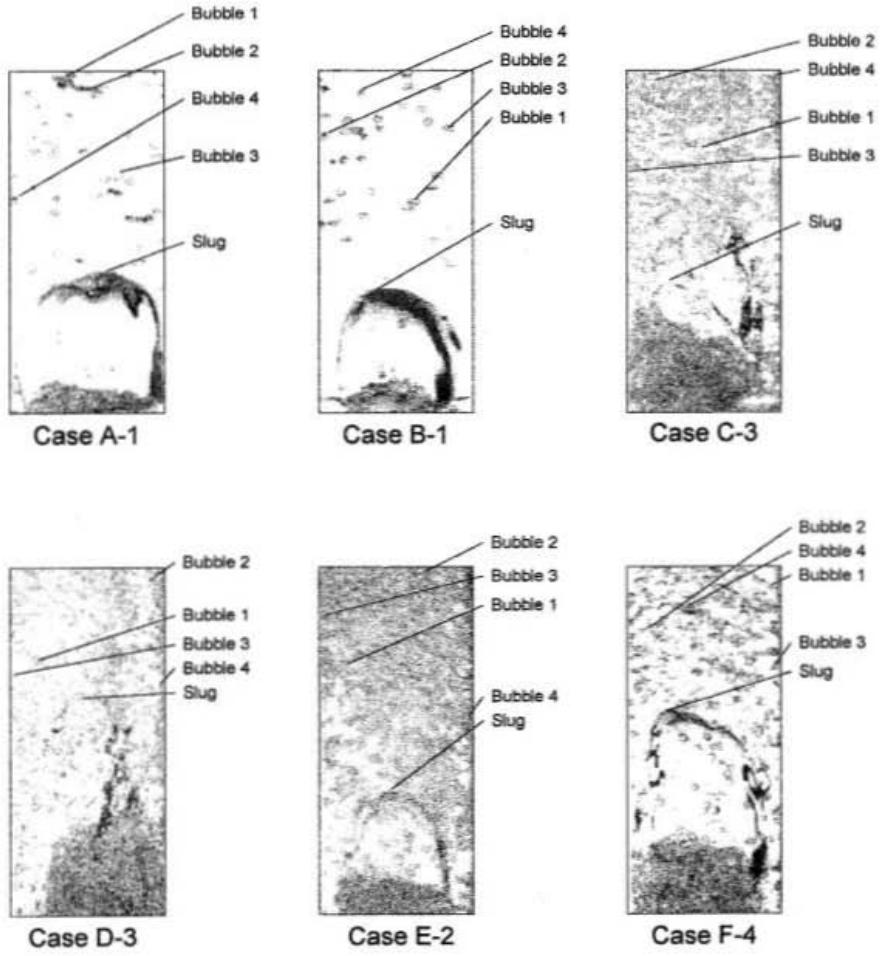

Figure 5.1: Bubble and Slug Identification for Motion Tracking Analysis

Table 5.3: Case A-1, Motion Tracking Results

x coordinate (inches)	y coordinate (inches)	Frame Number	Time Interval(s)	Delta Y (inches)	Velocity (in/s)	Velocity (m/s)
Slug						
6.083	6.364	120	0	0	0	0
6.066	6.231	121	0.004	0.133260	33.315	0.84620
6.066	6.083	122	0.004	0.148760	37.190	0.94463
6.066	5.950	123	0.004	0.132231	33.058	0.83967
					Average	**0.88**
Bubble 1						
5.223	2.182	120	0	0	0	0
5.223	2.066	121	0.004	0.115702	28.926	0.73472
5.207	1.917	122	0.004	0.149676	37.419	0.95044
5.190	1.802	123	0.004	0.116877	29.219	0.74216
					Average	**0.81**
Bubble 2						
5.785	2.397	120	0	0	0	0
5.769	2.264	121	0.004	0.133260	33.315	0.84620
5.769	2.132	122	0.004	0.132231	33.058	0.83967
5.769	2.017	123	0.004	0.115702	28.926	0.73472
					Average	**0.81**
Bubble 3						
6.944	3.814	120	0	0	0	0
6.960	3.699	121	0.004	0.116877	29.219	0.74216
6.944	3.599	122	0.004	0.100542	25.135	0.63843
6.960	3.500	123	0.004	0.100542	25.135	0.63843
					Average	**0.67**
Bubble 4						
4.380	4.678	120	0	0	0	0
4.380	4.579	121	0.004	0.099174	24.793	0.62974
4.347	4.479	122	0.004	0.104538	26.135	0.66383
4.331	4.364	123	0.004	0.116877	29.219	0.74216
					Average	**0.68**

Table 5.4: Case B-1 Motion Tracking Results

x coordinate (inches)	y coordinate (inches)	Frame Number	Time Interval(s)	Delta Y (inches)	Velocity (in/s)	Velocity (m/s)
Slug						
5.583	6.866	23	0	0	0	0
5.583	6.666	24	0.004	0.199984	49.996	1.26990
5.583	6.483	25	0.004	0.183319	45.830	1.16408
5.583	6.300	26	0.004	0.183319	45.830	1.16408
					Average	**1.20**
Bubble 1						
6.150	4.983	23	0	0	0	0
6.150	4.783	24	0.004	0.199984	49.996	1.26990
6.150	4.600	25	0.004	0.183319	45.830	1.16408
6.150	4.400	26	0.004	0.199984	49.996	1.26990
					Average	**1.23**
Bubble 2						
5.133	3.066	23	0	0	0	0
5.133	2.916	24	0.004	0.150911	37.728	0.95829
5.133	2.783	25	0.004	0.134360	33.590	0.85319
5.133	2.650	26	0.004	0.133323	33.331	0.84661
					Average	**0.89**
Bubble 3						
6.899	3.216	23	0	0	0	0
6.883	3.083	24	0.004	0.134360	33.590	0.85319
6.866	2.983	25	0.004	0.101371	25.343	0.64371
6.866	2.850	26	0.004	0.133323	33.331	0.84661
					Average	**0.78**
Bubble 4						
5.400	1.617	23	0	0	0	0
5.383	1.467	24	0.004	0.149988	37.497	0.95242
5.400	1.317	25	0.004	0.149988	37.497	0.95242
5.400	1.183	26	0.004	0.133323	33.331	0.84661
					Average	**0.92**

Table 5.5: Case C-3, Motion Tracking Results

x coordinate (inches)	y coordinate (inches)	Frame Number	Time Interval(s)	Delta Y (inches)	Velocity (in/s)	Velocity (m/s)
Slug						
5.147	6.983	277	0	0	0	0
5.147	6.753	278	0.004	0.229477	57.369	1.45717
5.163	6.524	279	0.004	0.230062	57.516	1.46091
5.163	6.278	280	0.004	0.245869	61.467	1.56126
					Average	**1.49**
Bubble 1						
5.655	3.918	277	0	0	0	0
5.655	3.672	278	0.004	0.246414	61.604	1.56474
5.639	3.409	279	0.004	0.262772	65.693	1.66860
5.655	3.147	280	0.004	0.262772	65.693	1.66860
					Average	**1.63**
Bubble 2						
5.180	2.147	277	0	0	0	0
5.163	1.934	278	0.004	0.213716	53.429	1.35710
5.163	1.705	279	0.004	0.229477	57.369	1.45717
5.147	1.475	280	0.004	0.230062	57.516	1.46091
					Average	**1.43**
Bubble 3						
4.688	4.376	277	0	0	0	0
4.672	4.147	278	0.004	0.229477	57.369	1.45717
4.655	3.885	279	0.004	0.262772	65.693	1.66860
4.639	3.639	280	0.004	0.246414	61.604	1.56474
					Average	**1.56**
Bubble 4						
7.360	1.869	277	0	0	0	0
7.343	1.656	278	0.004	0.213716	53.429	1.35710
7.343	1.426	279	0.004	0.229477	57.369	1.45717
7.343	1.180	280	0.004	0.245869	61.467	1.56126
					Average	**1.46**

Table 5.6: Case D-3, Motion Tracking Results

x coordinate (inches)	y coordinate (inches)	Frame Number	Time Interval(s)	Delta Y (inches)	Velocity (in/s)	Velocity (m/s)
Slug						
5.875	4.806	128	0	0	0	0
5.842	4.509	129	0.004	0.298057	74.514	1.89266
5.842	4.164	130	0.004	0.345606	86.401	2.19459
5.842	3.851	131	0.004	0.312691	78.173	1.98559
					Average	**2.02**
Bubble 1						
5.349	3.703	128	0	0	0	0
5.349	3.390	129	0.004	0.313124	78.281	1.98834
5.332	3.045	130	0.004	0.345997	86.499	2.19707
5.332	2.748	131	0.004	0.296234	74.058	1.88107
					Average	**2.02**
Bubble 2						
6.813	1.893	128	0	0	0	0
6.813	1.580	129	0.004	0.312691	78.173	1.98559
6.813	1.284	130	0.004	0.296234	74.058	1.88107
6.797	0.971	131	0.004	0.313124	78.281	1.98834
					Average	**1.95**
Bubble 3						
4.427	2.864	128	0	0	0	0
4.411	2.551	129	0.004	0.312691	78.173	1.98559
4.394	2.304	130	0.004	0.247409	61.852	1.57104
4.394	1.991	131	0.004	0.312691	78.173	1.98559
					Average	**1.85**
Bubble 4						
4.740	3.357	128	0	0	0	0
4.723	3.094	129	0.004	0.263833	65.958	1.67533
4.723	2.798	130	0.004	0.296234	74.058	1.88107
4.723	2.485	131	0.004	0.312691	78.173	1.98559
					Average	**1.85**

Table 5.7: Case E-2, Motion Tracking Results

x coordinate (inches)	y coordinate (inches)	Frame Number	Time Interval(s)	Delta Y (inches)	Velocity (in/s)	Velocity (m/s)
Slug						
7.640	7.422	329	0	0	0	0
7.623	7.238	330	0.002	0.185058	92.529	2.35024
7.606	7.054	331	0.002	0.185058	92.529	2.35024
7.606	6.869	332	0.002	0.184298	92.149	2.34058
					Average	**2.35**
Bubble 1						
6.802	4.591	329	0	0	0	0
6.786	4.423	330	0.002	0.168380	84.190	2.13843
6.786	4.256	331	0.002	0.167544	83.772	2.12781
6.786	4.088	332	0.002	0.167544	83.772	2.12781
					Average	**2.13**
Bubble 2						
7.875	2.480	329	0	0	0	0
7.858	2.312	330	0.002	0.168380	84.190	2.13843
7.858	2.145	331	0.002	0.167544	83.772	2.12781
7.858	1.977	332	0.002	0.167544	83.772	2.12781
					Average	**2.13**
Bubble 3						
6.601	3.736	329	0	0	0	0
6.584	3.585	330	0.002	0.151717	75.859	1.92682
6.584	3.435	331	0.002	0.150790	75.395	1.91503
6.568	3.284	332	0.002	0.151717	75.859	1.92682
					Average	**1.92**
Bubble 4						
9.060	5.730	329	0	0	0	0
9.060	5.579	330	0.002	0.150790	75.395	1.91503
9.060	5.428	331	0.002	0.150790	75.395	1.91503
9.043	5.278	332	0.002	0.151717	75.859	1.92682
					Average	**1.92**

Table 5.8: Case F-4, Motion Tracking Results

x coordinate (inches)	y coordinate (inches)	Frame Number	Time Interval(s)	Delta Y (inches)	Velocity (in/s)	Velocity (m/s)
Slug						
5.091	5.471	374	0	0	0	0
5.091	5.140	375	0.004	0.330567	82.642	2.09911
5.074	4.826	376	0.004	0.314474	78.618	1.99690
5.058	4.463	377	0.004	0.363999	91.000	2.31140
					Average	**2.14**
Bubble 1						
7.041	1.669	374	0	0	0	0
7.025	1.504	375	0.004	0.166108	41.527	1.05479
7.008	1.339	376	0.004	0.166108	41.527	1.05479
6.991	1.157	377	0.004	0.182562	45.640	1.15926
					Average	**1.09**
Bubble 2						
4.876	2.892	374	0	0	0	0
4.859	2.628	375	0.004	0.264970	66.242	1.68255
4.859	2.380	376	0.004	0.247925	61.981	1.57432
4.843	2.149	377	0.004	0.231987	57.997	1.47312
					Average	**1.58**
Bubble 3						
6.991	3.471	374	0	0	0	0
6.975	3.190	375	0.004	0.281468	70.367	1.78732
6.975	2.926	376	0.004	0.264454	66.113	1.67927
6.958	2.678	377	0.004	0.248476	62.119	1.57782
					Average	**1.68**
Bubble 4						
5.471	2.645	374	0	0	0	0
5.454	2.347	375	0.004	0.297969	74.492	1.89210
5.471	2.083	376	0.004	0.264970	66.242	1.68255
5.471	1.785	377	0.004	0.297511	74.378	1.88920
					Average	**1.82**

The bubble/slug velocities from the motion tracking reveal several predominant trends:

1. The bubble velocity is greater in the central region of the pipe flow than at the pipe walls.
2. The slug velocity is greater than the velocities of the smaller bubbles.
3. The slug appears to have a dominant influence on the neighboring smaller bubbles.

The average small bubble velocities for Case A-1, obtained from the motion tracking algorithm, clearly indicate the reduced bubble velocity near the pipe wall. The velocities of Bubble 3 and Bubble 4, located near the pipe wall, are about 17 percent less than the velocities of Bubble 1 and Bubble 2, located in the central region of the flow. Similar results are apparent from the results for Case E-2 where the velocities of Bubble 3 and Bubble 4 are about 10 percent less than the velocities of Bubble 1 and Bubble 2. An average small bubble velocity is determined for each test case from the four small bubble velocities (Table 5.9). In each test case, except for Case C-3, the slug velocity is greater than the average bubble velocity. The percent difference between the slug and bubble velocities is also shown in the table. For Case C-3 the percent difference between the slug and bubble velocities is only 2 percent. The percent difference between the slug and bubble velocities for both cases C-3 and D-3 is smaller than the percent difference for the other four cases. For these two conditions, more mixing is evident, making the slugs less distinguishable and the velocities between the slugs and bubbles closer.

Table 5.9: Slug and Bubble Velocities determined from the Motion Tracking Algorithm

Test Case	Slug Velocity (m/s)	Average Bubble Velocity (m/s)	% Difference in Slug and Bubble Velocities
A-1	0.88	0.74	16
B-1	1.20	0.95	21
C-3	1.49	1.52	2
D-3	2.02	1.92	5
E-2	2.35	2.03	14
F-4	2.14	1.54	28

5.1.2 Edge Detection Cross-Correlation Algorithm Results

The edge detection cross-correlation algorithm is also used to calculate an average gas slug and bubble velocity. This algorithm removes the subjectivity associated with the motion tracking algorithm and provides more detailed bubble velocity and size information. A sample of the results from the edge detection cross-correlation algorithm for each test case is presented in this section. The results for each case are presented in a systematic fashion starting with a figure showing four original cropped images as captured by the camera. The second figure shows the same four images after image processing is applied to detect and obtain bubble size information. The third figure consists of three velocity vector plots superimposed on the segmentation grid and the original image. For Cases A-1 and B-1 the image area is divided into three vertical and seven horizontal segments while for Cases C-3, D-3, E-2 and F-4 the image area is divided into four vertical and ten horizontal segments to better capture details of the higher concentration of gas bubbles. The horizontal and vertical scales are image pixel values. Only three velocity vector plots can be generated from the four original images,

because the cross-correlation function must be applied between two images. Three subsequent tables show the velocity vector matrix values for each vector previously shown in the corresponding velocity vector plot. The velocity vectors are positioned at the geometric center of each segment. Three histograms are presented after the velocity vector matrix tables to show the bubble size distribution for each velocity vector plot. The histograms show the quantity of bubbles in each bubble size category as determined by the ratio of the estimated bubble diameter to the pipe diameter (d/D). To ensure that each histogram has a standard bin structure, a bin labeled 'more' is included to lump bubbles with d/D > 0.9 into one category. Values typically fall in this category when clusters of bubbles appear as a slug or when clusters of bubbles are joined with a slug. Table 5.10 provides a concise summary of the selected flow visualization results presented in the following pages.

Table 5.10: Summary of Figure and Table Numbers for Flow Visualization Results

Test Case	Original Images	Filled Images	Velocity Vector Plots	Velocity Vector Matrices	Bubble Size Histograms
Case A-1	Fig. 5.2	Fig. 5.3	Fig. 5.4	Tables 5.11-5.13	Figs. 5.5-5.7
Case B-1	Fig. 5.8	Fig. 5.9	Fig. 5.10	Tables 5.14-5.16	Figs. 5.11-5.13
Case C-3	Fig. 5.14	Fig 5.15	Fig. 5.16	Tables 5.17-5.19	Figs. 5.17-5.19
Case D-3	Fig. 5.20	Fig. 5.21	Fig. 5.22	Tables 5.20-5.22	Figs. 5.23-5.25
Case E-2	Fig. 5.26	Fig. 5.27	Fig. 5.28	Tables 5.23-5.25	Figs. 5.29-5.31
Case F-4	Fig. 5.32	Fig. 5.33	Fig 5.34	Tables 5.26-5.28	Figs. 5.35-5.37

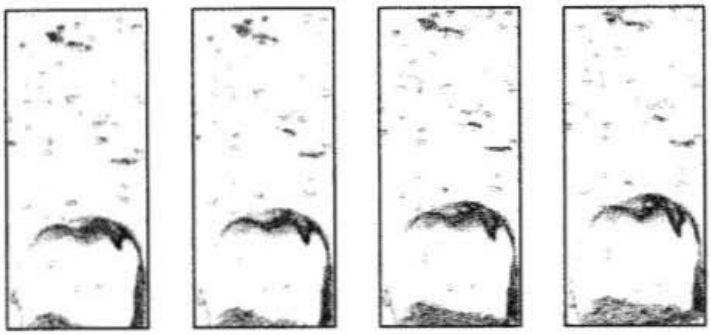

Figure 5.2: Case A-1, Original Images Frames 120-123

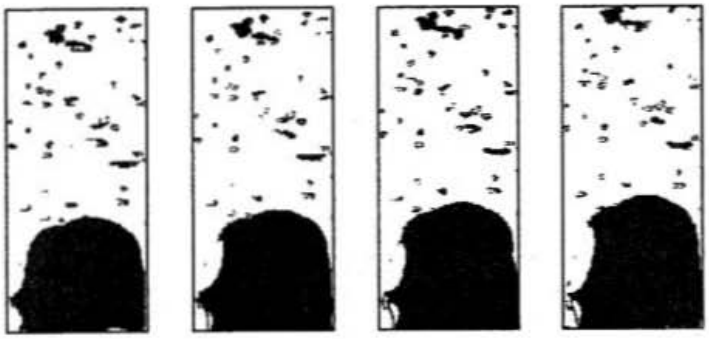

Figure 5.3: Case A-1, Filled Images Frames 120-123

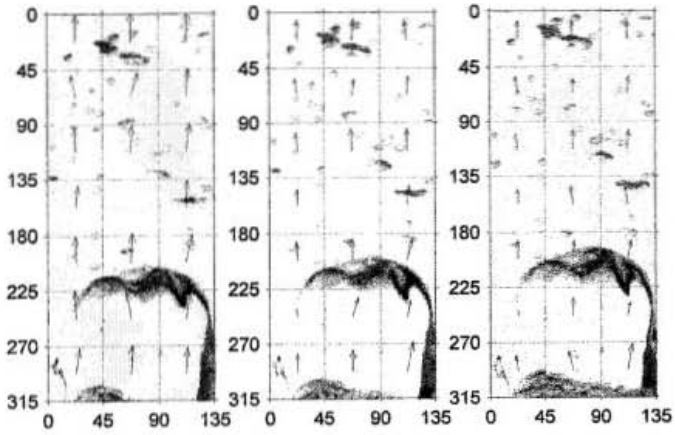

Figure 5.4: Case A–1, Velocity Vector Plots Frames 120-123

Table 5.11: Case A-1, Velocity Vector Matrix Frames 120-121

Center Coordinates of Segment (pixels)	22.5	67.5	112.5
22.5	0.7494	0.8038	0.8154
67.5	0.6012	0.6473	0.7545
112.5	0.6681	0.7184	0.7563
157.5	0.5815	0.0000	0.6984
202.5	0.7154	0.7910	0.7375
247.5	0.7535	0.7360	0.6511
292.5	0.6739	0.7662	0.7011

Table 5.12: Case A-1, Velocity Vector Matrix Frames 121-122

Center Coordinates of Segment (pixels)	22.5	67.5	112.5
22.5	0.7473	0.7868	0.7227
67.5	0.6604	0.6277	0.6944
112.5	0.6654	0.7828	0.8019
157.5	0.5819	0.0000	0.7122
202.5	0.7268	0.8094	0.7699
247.5	0.3023	0.7059	0.5732
292.5	0.6809	0.8166	1.1076

Table 5.13: Case A-1, Velocity Vector Matrix Frames 122-123

Center Coordinates of Segment (pixels)	22.5	67.5	112.5
22.5	0.7474	0.7999	0.7541
67.5	0.7112	0.6127	0.7156
112.5	0.6405	0.7829	0.7813
157.5	0.6004	0.7499	0.7204
202.5	0.7607	0.7691	0.7488
247.5	0.1909	0.6982	0.5260
292.5	0.6023	0.8155	1.0787

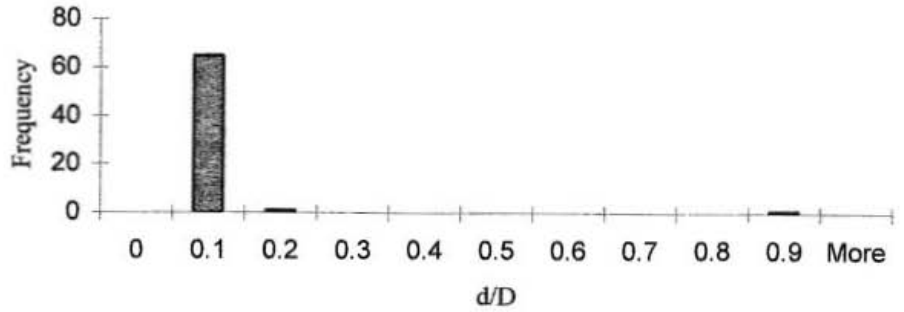

Figure 5.5: Case A_1, Bubble Size Histogram Frames 120-121

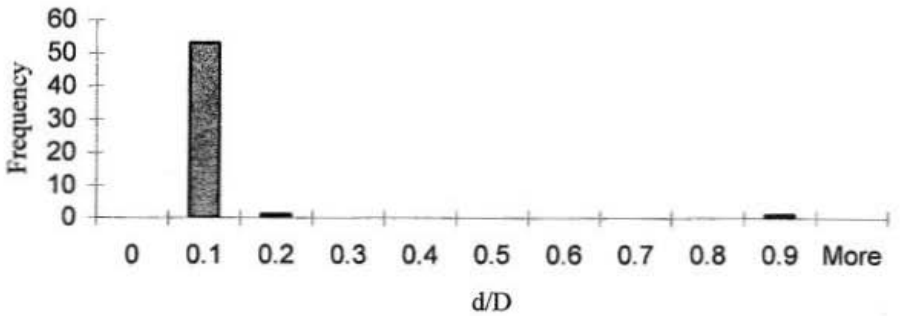

Figure 5.6: Case A-1, Bubble Size Histogram Frames 121-122

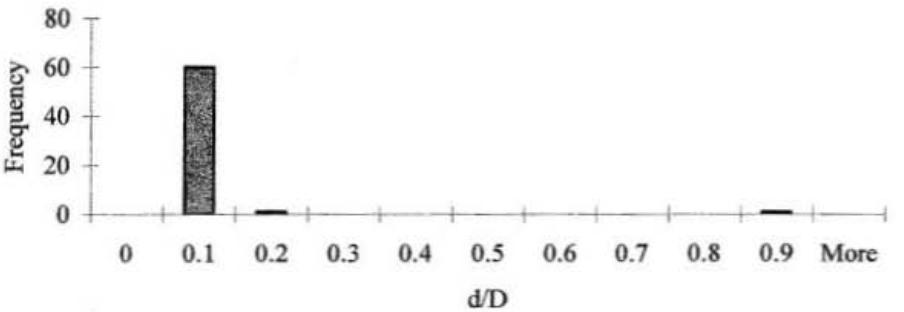

Figure 5.7: Case A-1, Bubble Size Histogram Frames 122-123

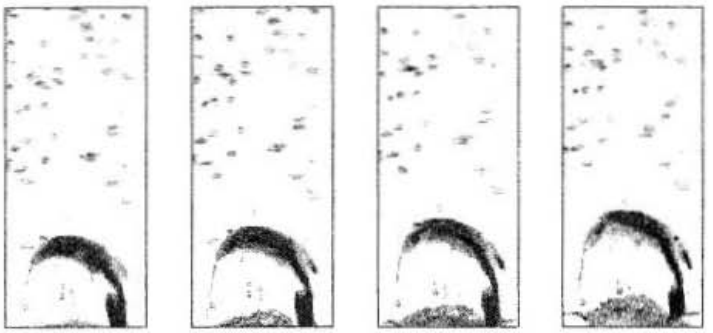

Figure 5.8: Case B-1, Original Images Frames 23-26

Figure 5.9: Case B-1, Filled Images Frames 23-26

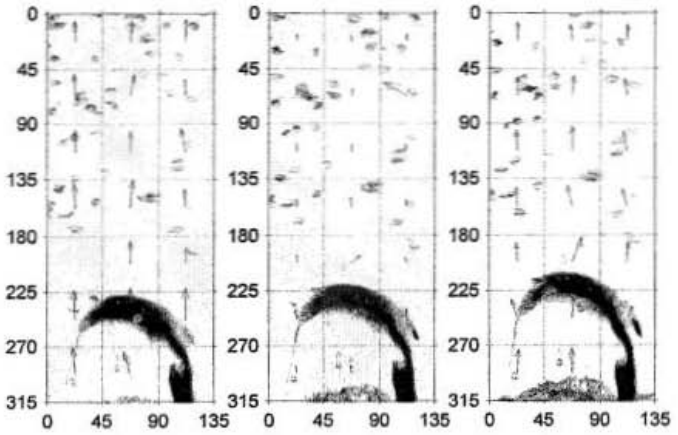

Figure 5.10: Case B-1, Velocity Vector Plots Frames 23-26

Table 5.14: Case B-1, Velocity Vector Matrix Frames 23-24

Center Coordinates of Segment (pixels)	22.5	67.5	112.5
22.5	0.8343	0.8391	0.8922
67.5	0.9653	0.9107	0.7361
112.5	0.8636	0.8129	0.9315
157.5	0.9676	1.1359	0.7486
202.5	0.0000	0.9310	0.6358
247.5	1.1970	1.2524	1.2472
292.5	1.1436	0.9279	0.2766

Table 5.15: Case B-1, Velocity Vector Matrix Frames 24-25

Center Coordinates of Segment (pixels)	22.5	67.5	112.5
22.5	0.8367	0.7500	0.8433
67.5	0.9444	0.8874	1.5192
112.5	0.8877	0.8221	0.8091
157.5	0.9614	1.1124	0.8100
202.5	0.8955	0.9073	0.6533
247.5	1.0619	0.9115	1.1263
292.5	0.9178	0.9818	0.3875

Table 5.16: Case B-1, Velocity Vector Matrix Frames 25-26

Center Coordinates of Segment (pixels)	22.5	67.5	112.5
22.5	0.8400	0.7253	0.7400
67.5	0.8922	0.9397	0.7694
112.5	0.9540	1.1183	0.8806
157.5	0.9034	0.9288	0.8023
202.5	0.9235	1.1461	0.9097
247.5	0.8611	0.9051	0.5200
292.5	1.1385	1.1539	0.9909

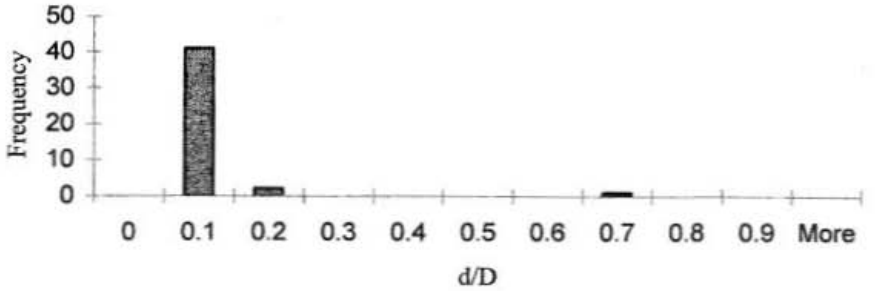

Figure 5.11: Case B-1, Bubble Size Histogram Frames 23-24

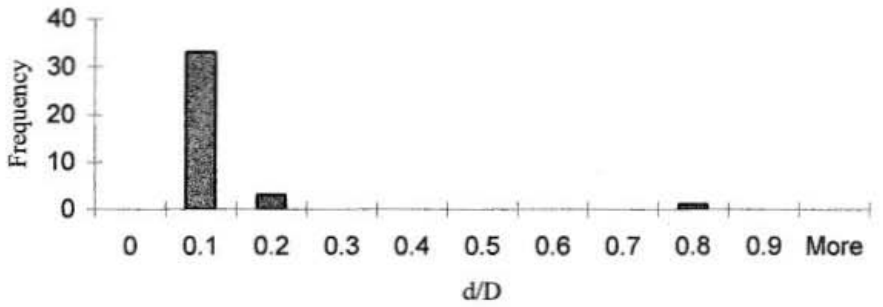

Figure 5.12: Case B-1, Bubble Size Histogram Frames 24-25

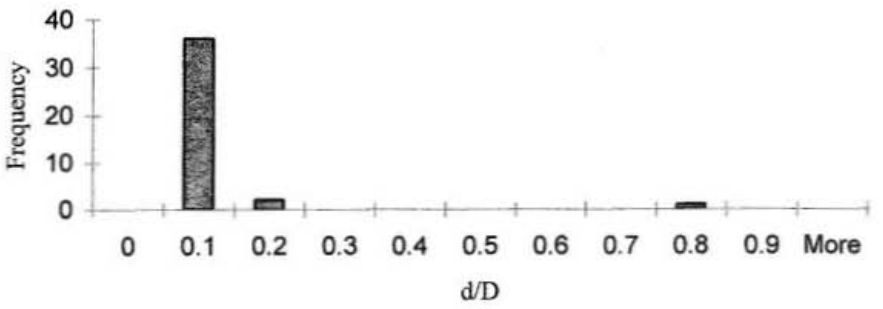

Figure 5.13: Case B-1, Bubble Size Histogram Frames 25-26

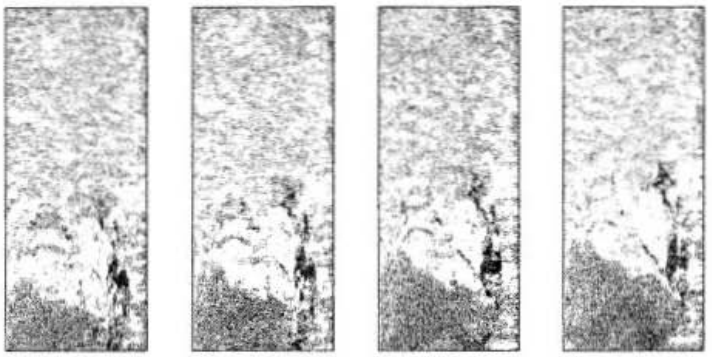

Figure 5.14: Case C-3, Original Images Frames 277-280

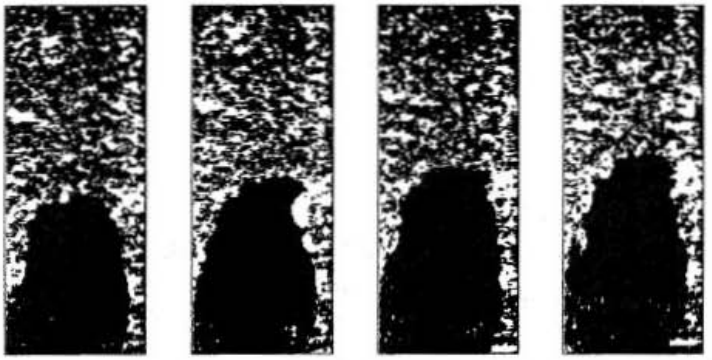

Figure 5.15: Case C-3, Filled Images Frames 277-280

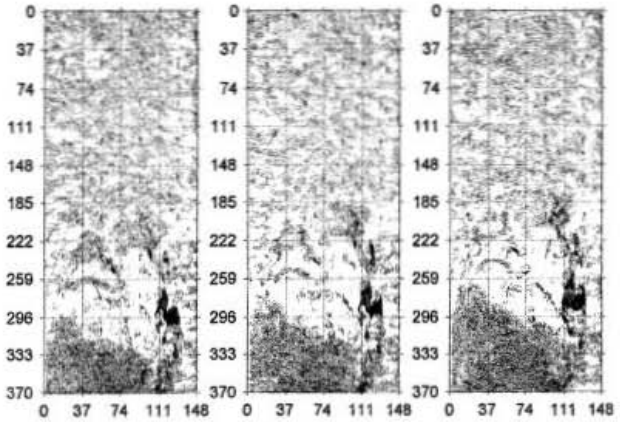

Figure 5.16: Case C-3, Velocity Vector Plots Frames 277-280

Table 5.17: Case C-3, Velocity Vector Matrix Frames 277-278

Center Coordinates of Segment (pixels)	18.5	55.5	92.5	129.5
18.5	1.5471	1.6883	1.7453	1.3763
55.5	1.7267	1.7071	1.5996	1.5506
92.5	1.4590	1.6660	1.6736	1.4527
129.5	1.6538	1.7843	1.7816	1.6006
166.5	1.6210	1.6757	1.7677	1.8543
203.5	1.6949	1.4403	1.7520	1.5914
240.5	1.3766	1.3689	1.4305	1.2843
277.5	1.1695	3.8768	0.8128	0.9586
314.5	1.5797	1.6780	0.7242	0.9194
351.5	2.0472	1.5385	1.5243	0.5887

Table 5.18: Case C-3, Velocity Vector Matrix Frames 278-279

Center Coordinates of Segment (pixels)	18.5	55.5	92.5	129.5
18.5	1.6973	4.3365	1.7127	1.4142
55.5	1.6624	1.6853	1.6143	1.4812
92.5	1.5834	1.6985	1.8826	1.5074
129.5	3.5160	1.7406	1.7214	1.7938
166.5	1.6513	1.6004	1.7322	1.7159
203.5	1.5978	1.4754	1.5115	1.4734
240.5	1.1959	1.3000	1.2119	1.2071
277.5	1.7835	0.9110	0.7478	0.9218
314.5	1.9054	1.9407	2.0283	0.5988
351.5	2.8903	1.9993	1.5401	0.6453

Table 5.19: Case C-3, Velocity Vector Matrix Frames 279-280

Center Coordinates of Segment (pixels)	18.5	55.5	92.5	129.5
18.5	1.6721	1.6796	1.5949	1.4577
55.5	1.6461	1.7051	1.5651	1.5137
92.5	1.5712	1.7182	1.7557	1.7654
129.5	1.5747	1.6834	1.7926	1.4518
166.5	1.6725	1.5552	1.7100	1.5529
203.5	1.3630	1.4285	1.4460	1.4238
240.5	1.0393	1.5633	3.3506	1.1040
277.5	1.5868	1.5861	0.7620	0.7159
314.5	2.1656	1.6013	1.8720	0.6470
351.5	1.0376	1.7000	2.1703	0.8188

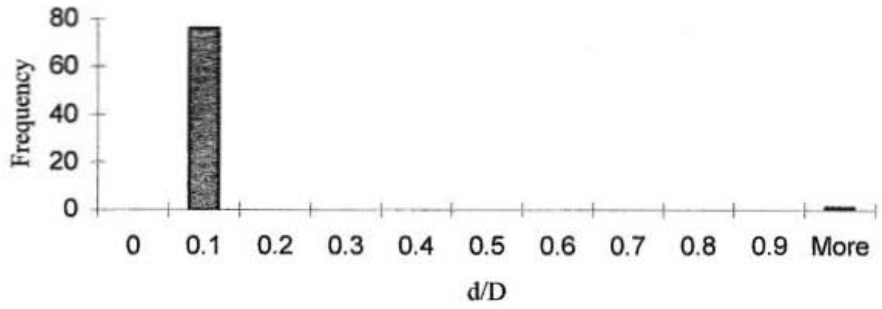

Figure 5.17: Case C-3, Bubble Size Histogram Frames 277-278

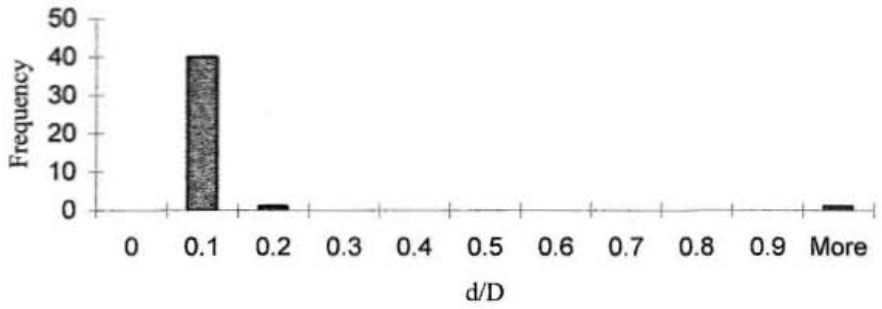

Figure 5.18: Case C-3, Bubble Size Histogram Frames 278-279

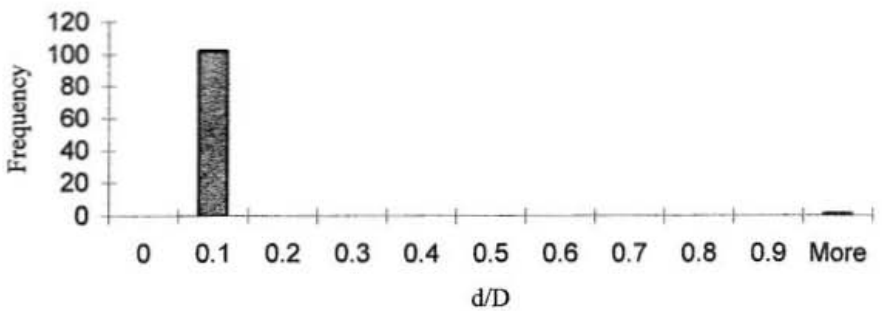

Figure 5.19: Case C-3, Bubble Size Histogram Frames 279-280

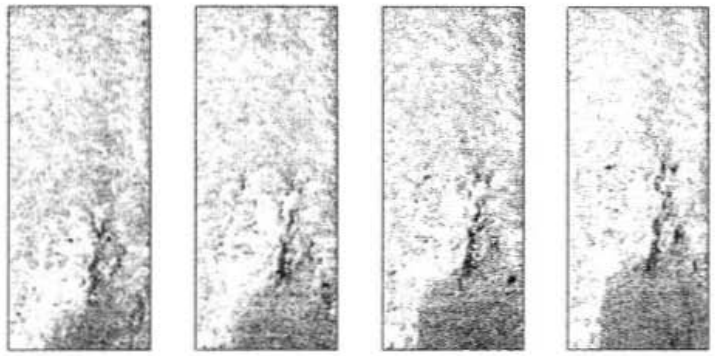

Figure 5.20: Case D-3, Original Images Frames 128-131

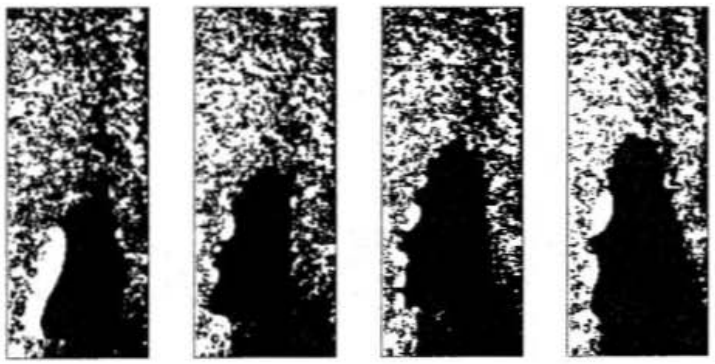

Figure 5.21: Case D-3, Filled Images Frames 128-131

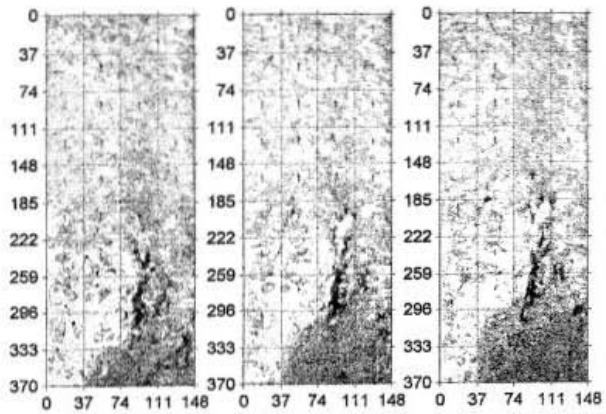

Figure 5.22: Case D-3, Velocity Vector Plots for Frames 128-131

Table 5.20: Case D-3, Velocity Vector Matrix Frames 128-129

Center Coordinates of Segment (pixels)	18.5	55.5	92.5	129.5
18.5	1.7130	1.7147	4.3781	1.8170
55.5	0.2583	2.0943	1.5934	1.7278
92.5	1.8189	2.1243	2.0676	1.7167
129.5	1.8299	1.9990	1.7685	1.7727
166.5	1.7892	1.9691	1.6036	1.5759
203.5	1.6712	1.9015	1.6163	1.7285
240.5	1.5674	1.3038	1.3623	1.5792
277.5	1.2097	1.2392	1.4622	1.3368
314.5	0.9850	0.5839	1.0570	3.1286
351.5	0.8639	1.8019	1.6738	1.0351

Table 5.21: Case D-3, Velocity Vector Matrix Frames 129-130

Center Coordinates of Segment (pixels)	18.5	55.5	92.5	129.5
18.5	1.6678	2.0040	1.9852	1.8237
55.5	3.8932	1.9487	1.5965	1.7003
92.5	1.9015	2.1197	1.9531	1.5643
129.5	1.8448	2.1033	2.7509	1.6205
166.5	1.8378	1.8443	2.2382	1.6109
203.5	1.5582	1.5318	1.6781	1.5948
240.5	1.4921	1.2721	1.4057	1.4576
277.5	1.1538	1.1589	1.3611	1.3735
314.5	4.2838	1.6315	1.0827	1.0861
351.5	0.7460	1.9903	1.1316	3.6979

Table 5.22: Case D-3, Velocity Vector Matrix Frames 130-131

Center Coordinates of Segment (pixels)	18.5	55.5	92.5	129.5
18.5	1.6719	4.6701	1.6910	1.7587
55.5	4.0929	2.0429	1.7371	1.7927
92.5	1.8326	2.0703	1.8823	1.7487
129.5	1.7816	1.9288	1.6907	1.7319
166.5	0.5575	1.7124	1.7918	1.6525
203.5	3.7576	1.7035	3.7030	1.5343
240.5	1.4390	1.2149	1.4590	1.4209
277.5	4.4464	1.1042	1.3018	1.3366
314.5	0.8511	0.9603	1.0926	2.0155
351.5	0.7066	4.2960	1.1766	1.1712

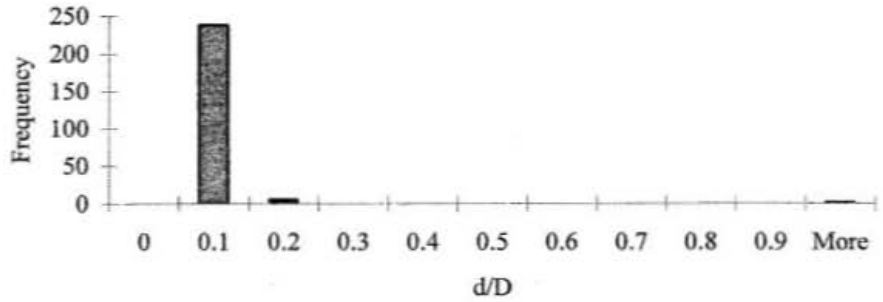

Figure 5.23: Case D-3, Bubble Size Histogram Frames 128-129

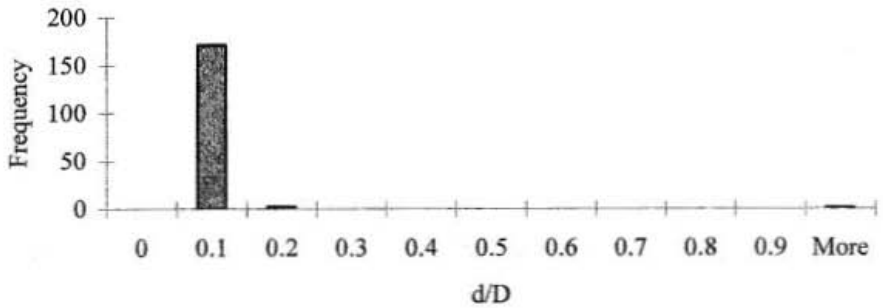

Figure 5.24: Case D-3, Bubble Size Histogram Frames 129-130

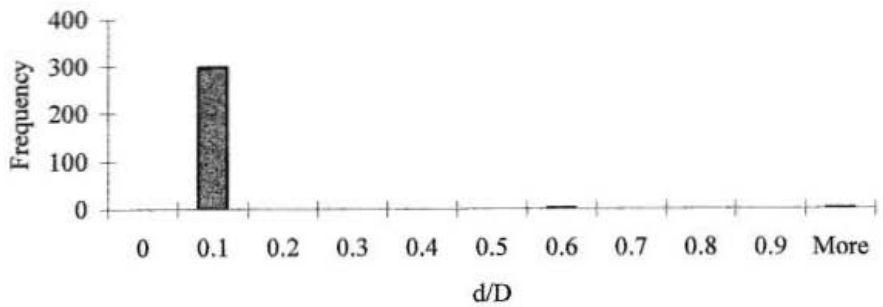

Figure 5.25: Case D-3, Bubble Size Histogram Frames 130-131

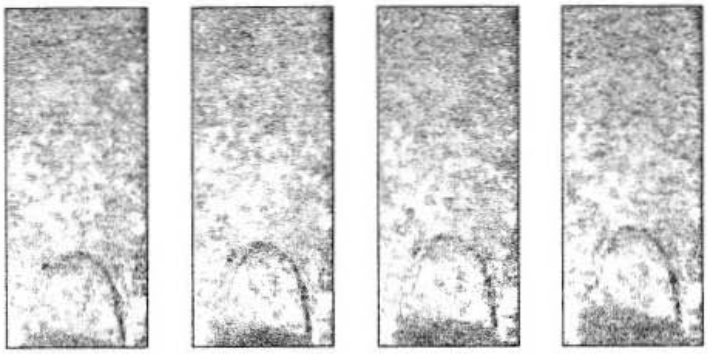

Figure 5.26: Case E-2, Original Images Frames 329-332

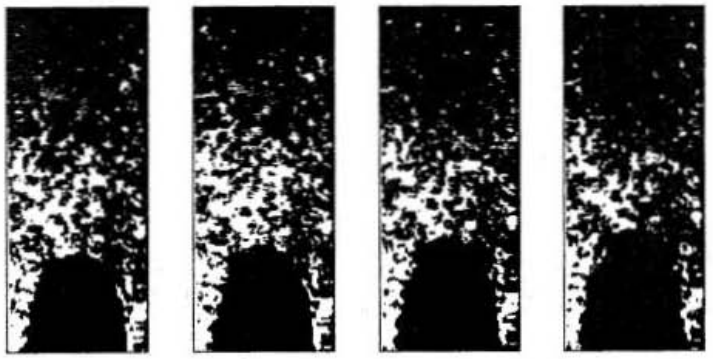

Figure 5.27: Case E-2, Filled Images Frames 329-332

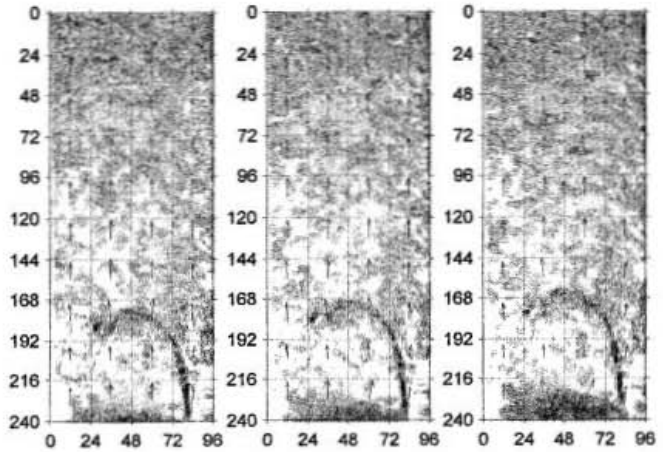

Figure 5.28: Case E-2, Velocity Vector Plots Frames 329-332

Table 5.23: Case E-2, Velocity Vector Matrix Frames 329-330

Center Coordinates of Segment (pixels)	12	36	60	84
12	1.8966	2.0410	2.0001	1.8363
36	1.9347	1.9951	1.9663	1.8120
60	1.9268	1.9281	2.0897	1.7474
84	1.9091	2.1099	2.0203	1.7993
108	1.8328	1.9468	1.9981	1.8679
132	1.8093	1.9777	1.8828	1.7916
156	1.8357	2.1244	1.9223	1.5900
180	1.7023	2.0592	2.2223	1.5639
204	1.4585	1.4832	1.4687	1.4227
228	1.3876	1.7679	1.8187	1.1434

Table 5.24: Case E-2, Velocity Vector Matrix Frames 330-331

Center Coordinates of Segment (pixels)	12	36	60	84
12	1.9187	2.1130	2.0236	1.7952
36	1.8854	1.9835	2.0646	1.8380
60	1.9505	2.0629	2.0693	1.7704
84	1.8256	2.0015	2.0939	1.7755
108	1.8532	1.9911	2.0574	1.8109
132	1.7458	1.9010	1.9085	1.7530
156	1.7365	1.9987	1.9306	1.5702
180	1.6330	1.8546	2.1105	1.5637
204	1.4827	1.4153	1.4393	1.3797
228	1.7584	1.9358	1.9457	1.2413

Table 5.25: Case E-2, Velocity Vector Matrix Frames 331-332

Center Coordinates of Segment (pixels)	12	36	60	84
12	1.9788	2.0768	1.9574	1.8498
36	1.9784	1.8877	2.0950	1.9021
60	1.9106	1.9868	2.0139	1.7781
84	1.8656	2.1138	2.0693	1.6341
108	1.9169	2.0057	2.0464	1.9288
132	1.8818	2.0524	1.9274	1.8330
156	1.6126	2.1010	2.0075	1.5477
180	1.6156	1.9818	1.9575	1.4962
204	1.4215	1.4252	1.3603	1.3687
228	1.6189	1.9662	1.9353	1.3134

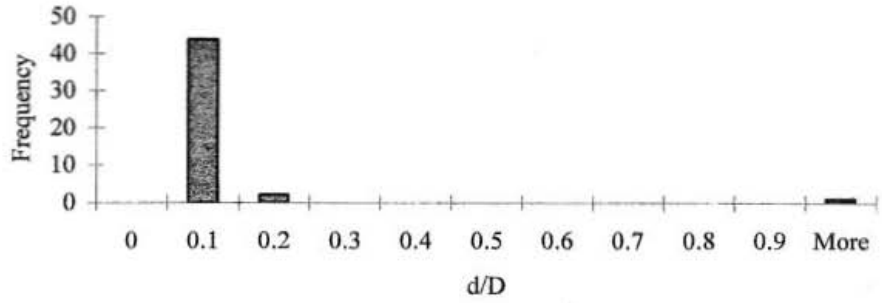

Figure 5.29: Case E-2, Bubble Size Histogram Frames 329-330

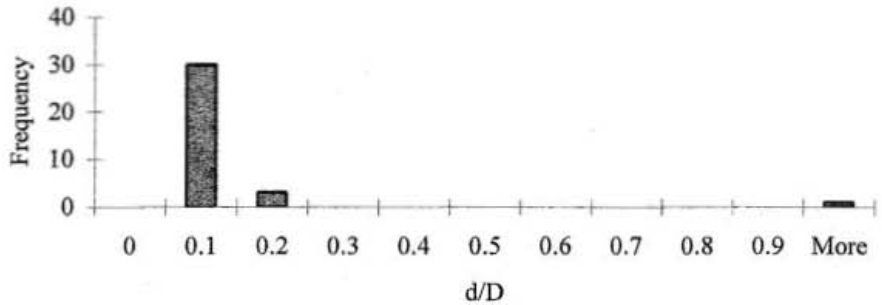

Figure 5.30: Case E-2, Bubble Size Histogram Frames 330-331

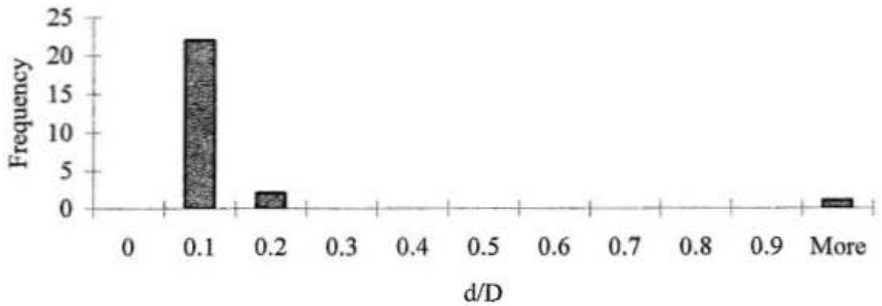

Figure 5.31: Case E-2, Bubble Size Histogram Frames 331-332

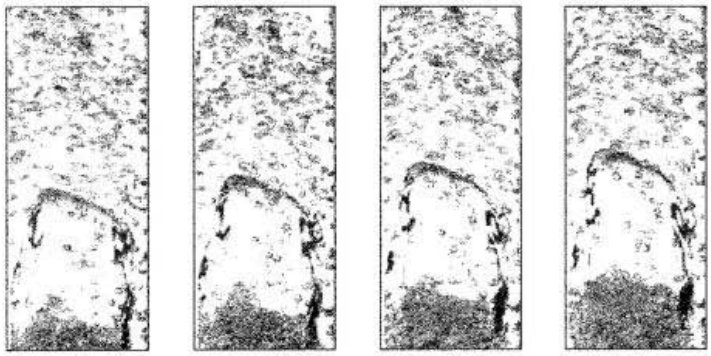

Figure 5.32: Case F-4, Original Images Frames 374-377

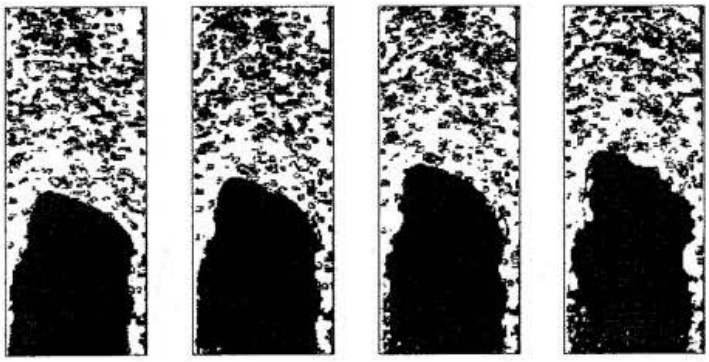

Figure 5.33: Case F-4, Filled Images Frames 374-377

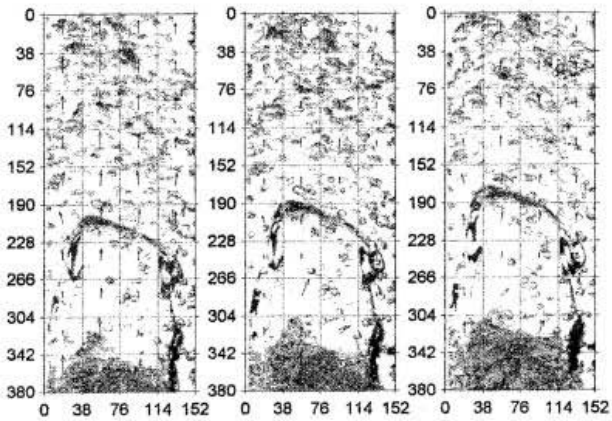

Figure 5.34: Case F-4, Velocity Vector Plots Frames 374-377

Table 5.26: Case F-4, Velocity Vector Matrix Frames 374-375

Center Coordinates of Segment (pixels)	19	57	95	133
19	1.5488	1.5812	1.6014	1.2236
57	1.6631	1.5378	1.5483	1.3461
95	1.7223	1.9531	1.7996	1.4638
133	1.5226	1.9154	1.8198	1.3252
171	1.7050	1.8035	1.6718	1.4322
209	1.4000	1.9687	1.6538	1.3078
247	1.2944	1.3633	1.1291	1.2049
285	0.7910	1.1340	0.8680	0.7927
323	0.6207	2.0368	0.6139	0.5929
361	2.1724	1.6865	1.6100	0.5068

Table 5.27: Case F-4, Velocity Vector Matrix Frames 375-376

Center Coordinates of Segment (pixels)	19	57	95	133
19	1.4989	1.6255	3.3598	1.1782
57	1.4639	1.5814	1.6099	1.7032
95	1.7156	1.6144	1.8044	1.4179
133	1.5661	1.9578	1.8565	1.3850
171	1.5178	1.7982	1.7936	1.3369
209	1.3976	1.7510	2.0105	1.2271
247	1.0726	1.1306	1.0131	1.0806
285	0.7577	3.9181	0.8376	0.9633
323	1.6377	1.7313	1.8502	0.5296
361	2.3389	4.3486	0.5335	0.5660

Table 5.28: Case F-4, Velocity Vector Matrix Frames 376-377

Center Coordinates of Segment (pixels)	19	57	95	133
19	1.5394	1.6163	1.7582	1.1852
57	1.4608	1.6616	1.7527	1.6160
95	1.6408	1.8737	1.7773	1.3856
133	1.1699	1.8711	0.7270	1.3845
171	1.5867	1.9030	1.6309	1.2885
209	1.3053	1.2626	1.5416	1.1506
247	0.9132	1.1035	0.9432	0.9706
285	0.7097	1.1942	0.7569	0.6289
323	2.0067	2.2973	2.1962	0.4771
361	2.1493	1.9287	0.6254	0.5526

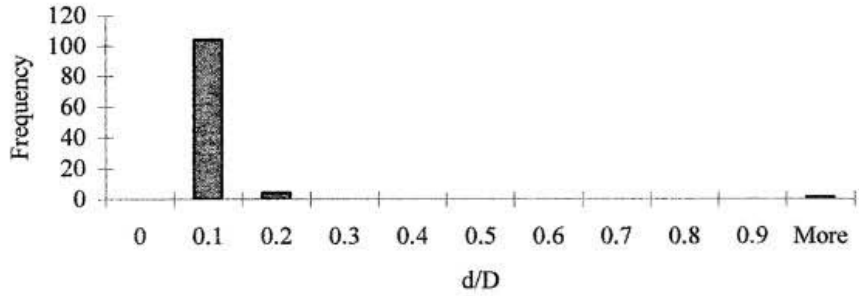

Figure 5.35: Case F-4, Bubble Size Histogram Frames 374-375

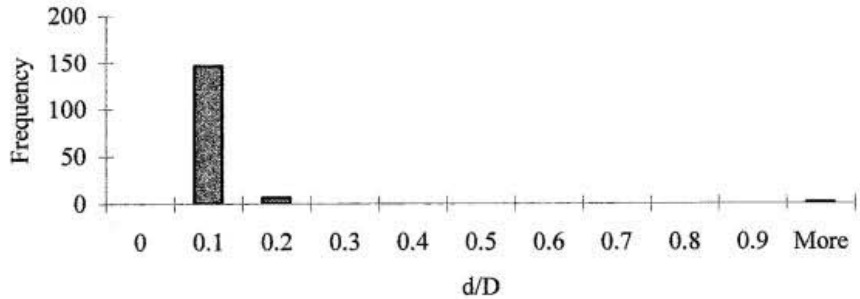

Figure 5.36: Case F-4, Bubble Size Histogram Frames 375-376

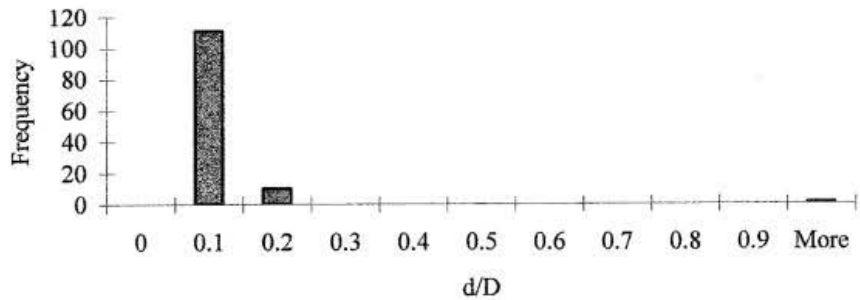

Figure 5.37: Case F-4, Bubble Size Histogram Frames 376-377

Gas bubble and slug velocities are determined systematically from the velocity vector matrix as explained in Section 4.2.6. For the case of a slug, the velocity vector located at the centroid of the slug and seven surrounding velocity vectors, predicted to be located at the tip of the slug, are used to determine an average slug velocity. Any velocity vector assumed to contribute to the average slug velocity is removed from the velocity vector matrix. The remaining velocity vectors are used to calculate an average gas bubble velocity. The average gas bubble and slug velocities, determined from the edge detection cross-correlation algorithm for the six selected test cases and the discrepancy of these values with the motion tracking results, are presented in Table 5.29.

Table 5.29: Slug and Bubble Velocities determined from the Edge Detection Cross-Correlation Algorithm and Comparison with Motion Tracking Results

Test Case	Slug Velocity (m/s)	Average Bubble Velocity (m/s)	Slug Velocity Discrepancy (%)	Bubble Velocity Discrepancy (%)
A-1	0.71	0.73	19	1
B-1	0.90	0.96	25	1
C-3	1.61	1.54	8	1
D-3	1.67	1.93	17	1
E-2	1.87	1.83	20	10
F-4	1.39	1.52	35	1

The bubble velocity results from the edge detection cross-correlation algorithm are in good agreement with the motion tracking results; however, the edge detection cross-correlation algorithm appears to under-predict the slug velocities. The discrepancy of the bubble velocity measurements using the cross-correlation algorithm for five of the six cases is only 1 percent, while for the other case it is 10 percent. The maximum discrepancy for the slug velocities is 35 percent, which suggests an error in the cross-

correlation results for slugs. The motion tracking velocity results and fundamental fluid mechanics theory indicate that the slug velocity should be greater than the small bubble velocity. The buoyancy force associated with large gas slugs in a vertical-up flow should cause the slug to have a greater velocity than the surrounding smaller bubbles. The velocity vector matrices generated from the edge detection cross-correlation algorithm indicate that the calculated slug velocities may not provide an accurate representation of the actual slug velocity. Oftentimes, either a poorly defined slug boundary or the content of the interrogation area produces an inaccurate representation of the slug velocity. The edge detection, on the left of the slug shown in Figures 5.3 and 5.4, indicates a problem that arises with the backlighting technique. An image with a poorly defined slug boundary frequently results in an unfavorable edge detection of the slug. This problem can be overcome by using the laser lighting technique which produces images with more clearly defined slug and bubble boundaries. The content of an interrogation area can also produce an inaccurate representation of the slug velocity. For example, the interrogation area may contain a large percentage of either white or black pixels due to the slug occupying most of the interrogation area. This results in an inaccurate shift of the slug between interrogation areas of consecutive images leading to a poor cross-correlation value. Interrogation areas located on the side of a gas slug typically contain a large quantity of black pixels oriented to form a thick vertical line. The cross-correlation function is also unable to detect a spatial shift in this line because its vertical orientation will remain the same on consecutive images. Also, an interrogation area may contain a

large quantity of small bubbles and only a small portion of a slug. This results in a velocity vector that does not accurately represent either the bubble or slug velocities.

The edge detection cross-correlation results of Case F-4 show many of the problems associated with determining an average slug velocity. The velocity vector matrix for Frames 374-375 (Table 5.26) in conjunction with the corresponding velocity vector plot (Fig. 5.34) illustrates some of these problems. The velocity vector, 1.9687 m/s, located at the vertical coordinate of 209 pixels and the horizontal coordinate of 57 pixels (209, 57) would be the best single segment to represent the slug tip velocity. This segment contains predominately the slug tip with very few smaller bubbles. It also contains a reasonable spread of black and white pixels that allow a close match between corresponding interrogation areas of consecutive images. The velocity vector located to the right, pixel coordinates (209, 95), is dominantly influenced by the presence of many smaller bubbles. This results in a lower velocity vector of 1.6538 m/s, representing a combination of the slug and small bubble velocities. Velocity vectors located on either side of the slug show the problem that arises when the cross-correlation function is applied to black pixels that form a vertical region. Examples include the velocity vectors 0.7910, 0.6207, 0.7927, 0.5929 and 0.5068 located at pixel coordinates (285, 19), (323, 19), (285, 133), (323, 133) and (361, 133), respectively. Due to these erroneous velocity vectors, the estimated average slug velocity is lower than the true slug velocity. This can be corrected by eliminating the false velocity vectors by considering the spatial shift of the entire slug as described below.

Although the edge detection cross-correlation algorithm under-predicts the actual slug velocity, the algorithm accurately estimates the bubble velocities. This indicates that the algorithm can successfully determine the spatial shift of the bubbles. In order to obtain accurate slug velocities from the edge detection cross-correlation algorithm, the images need to be pre-processed to remove the smaller bubbles and isolate the entire slug. Figure 5.38 shows two original images for Case B-1 followed by the corresponding manually modified and processed images. The slugs are first identified and cropped to isolate the slug and remove the bubbles (Fig. 5.38b). The boundary of the slug is then detected and filled (Figs. 5.38c and d). The results obtained using the cross-correlation algorithm with a coarse grid of two vertical segments and three horizontal segments on the pre-processed images containing only a slug are presented in Table 5.30. The discrepancy between the slug velocity results using this method and the results of the motion tracking algorithm are also included.

Table 5.30: Slug Velocity from Cross-Correlation Algorithm with Modified Images and Discrepancy with Motion Tracking Results

Test Case	Slug Velocity (m/s)	Slug Velocity Discrepancy (%)
A-1	0.93	5
B-1	1.24	1
C-3	1.47	3
D-3	1.98	10
E-2	2.30	3
F-4	1.97	8

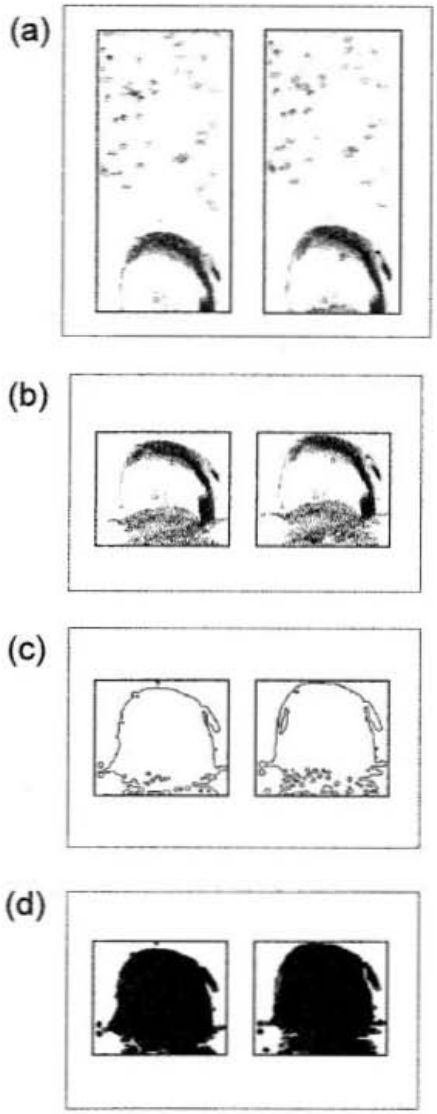

Figure 5.38: Manual Modification of Flow Images for Case B-1 (a) Original Images; (b) Bubbles Cropped from Images; (c) Edge Detection; (d) Slug Identification

The slug velocity results obtained using the modified images show a much better agreement between the two algorithms. The average discrepancy between the two algorithms is now less than 5 percent and the maximum discrepancy is 10 percent. This indicates that the edge detection cross-correlation algorithm can be used to accurately

determine slug velocities with some pre-processing of the images. Several possible modifications to the algorithm to allow accurate estimation of bubble and slug velocities without manually pre-processing the images are discussed in the next chapter.

The bubble size histograms provide information about the quantity and size of the gas bubbles present in each flow image, and are useful to estimate the interfacial areas. For the present flow, the majority of the smaller gas bubbles have a bubble to pipe diameter ratio of about 0.1 while the larger gas slugs have a bubble to pipe diameter ratio in excess of 0.8. For example, the bubble size histograms of Case A-1 indicate the presence of about sixty small gas bubbles, one slightly larger gas bubble and one slug. The results of the bubble size histograms at higher flow rates indicate the presence of additional larger bubbles that are very likely an agglomeration of small gas bubbles. This occurs because the edge detection routine tends to join bubbles that are closely positioned or overlapped. For example, Case E-2 indicates the presence of one large slug along with a small number of gas bubbles. In this example many of the small bubbles have been lumped into the large gas slug. It may be possible to overcome this problem by comparing the slug against a standard geometry and removing portions that fall outside this geometry. The current method assumes that the slug has a circular geometry based on the area of the connected regions. For accurate estimations of the bubble size distribution using this method, a large number of frames need to be analyzed and the results averaged to obtain statistically steady values.

5.2 Simultaneous Flow Visualization and Hot-Film Measurement Results

The results from the quantitative flow visualization techniques were corroborated with simultaneous hot-film anemometry measurements. The simultaneous flow visualization and hot-film measurements were performed with the camera positioned in two separate locations. In the first location the camera was focused directly on the hot-film probes to help discriminate the hot-film signals into the gas and liquid phases. This camera position provides a sequence of images showing the gas bubbles and slugs passing over the hot-film probe. In the second position, the camera was focused on the optical test section to obtain simultaneous velocity information from both measurement techniques.

5.2.1 Dynamic Response of the Hot-Film to the Passage of a Gas Slug

In order to discriminate the hot-film signals into the gas and liquid phases accurately, the dynamic response of the probe to the passage of a gas bubble needs to be clearly understood. This was investigated using simultaneous high-speed flow visualization and hot-film measurements with the camera focused directly on the hot film test section. Figure 5.39 shows the hot-film trace as a slug passes over the probe, with the corresponding flow images. The dynamic response of the probe is similar to that described by Farrar and Bruun (1989). As the slug front approaches the probe (A), the signal output increases because the liquid in front of the slug is moving with a greater velocity than the average liquid velocity. The signal continues to increase until the probe

pierces the slug (B), and this is accompanied by a small overshoot. This is followed by a steep drop (from B to C) due to the evaporation of the liquid film on the sensor surface. At locations D and E the probe is in the gas phase and the signal corresponds to that of the gas phase. When the back of the slug arrives at the probe, the rapid covering of the probe with the liquid results in a steep rise in the signal output (from F to G). At location H, the probe is in the wake region of the slug. The two events, B and F, correspond to the bubble front and back hitting the sensor, and need to be clearly identified to localize the slug passage. The two events are associated with a sign change in the time derivative of the signal, and this is used to facilitate the location of the bubble front and back.

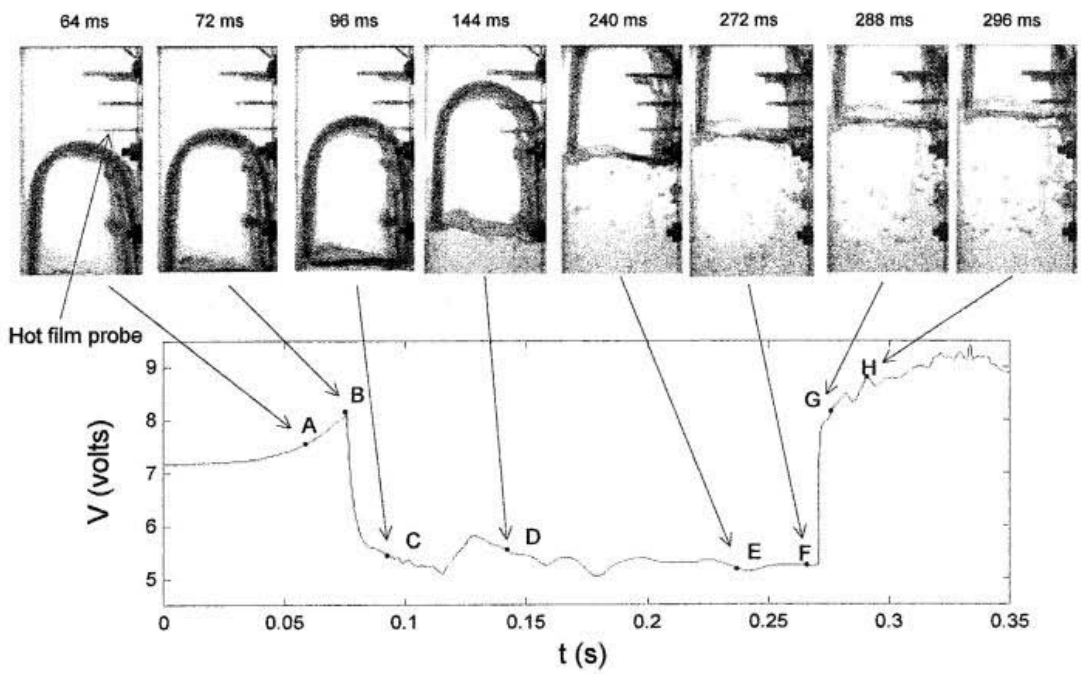

Figure 5.39: Dynamic Hot-Film Response to the Passage of a Gas Slug

5.2.2 Comparison of Flow Visualization and Hot Film Measurement Results

The gas bubble and slug velocities estimated from the flow visualization images are compared against the simultaneous hot-film anemometry results in Table 5.31. The slug velocities from the edge detection cross-correlation algorithm are for the pre-processed images that contain only a slug. The discrepancy in the results from the motion tracking algorithm to those obtained from the edge-detection cross-correlation algorithm and the hot-film data is given in Table 5.32.

Table 5.31: Comparison of Results

Test Case	Frames	Motion Tracking		Cross Correlation		Hot Film	
		Slug Velocity (m/s)	Bubble Velocity (m/s)	Slug Velocity (m/s)	Bubble Velocity (m/s)	Slug Velocity (m/s)	Bubble Velocity (m/s)
A-1	120-123	0.88	0.74	0.93	0.73		
A-2	126-129	1.00	0.74	-	0.76		
A-3	300-303	-	0.92	-	0.86		
A-4	465-468	1.06	0.91	-	0.95		
Average		**0.98**	**0.83**	**0.93**	**0.83**	**1.02**	**1.30**
B-1	23-26	1.20	0.95	1.24	0.96		
B-2	29-32	1.22	0.81	-	0.99		
B-3	100-103	-	1.13	-	1.06		
B-4	145-148	1.33	1.12	-	1.07		
Average		**1.25**	**1.00**	**1.24**	**1.02**	**1.20**	**0.93**
C-1	120-123	-	1.53	-	1.61		
C-2	164-167	1.46	1.51	-	1.49		
C-3	277-280	1.49	1.52	1.47	1.54		
C-4	387-390	1.56	1.56	-	1.47		
C-5	424-427	1.54	1.58	-	1.54		
Average		**1.51**	**1.54**	**1.47**	**1.51**	**1.44**	**1.54**
D-1	1-4	2.48	2.14	-	2.08		
D-2	43-46	2.15	2.10	-	1.86		
D-3	128-131	2.02	1.92	1.98	1.93		
D-4	300-303	-	2.04	-	1.82		
D-5	400-403	2.17	1.91	-	1.86		
Average		**2.21**	**2.02**	**1.98**	**1.91**	**2.16**	**1.97**
E-1	213-216	-	1.88	-	2.03		
E-2	329-332	2.35	2.03	2.30	1.83		
E-3	342-345	2.19	1.93	-	1.84		
E-4	733-736	2.18	2.07	-	2.02		
E-5	900-903	-	2.02	-	2.08		
Average		**2.24**	**1.99**	**2.30**	**1.96**	**2.25**	**1.84**
F-1	15-18	2.17	1.64	-	1.66		
F-2	69-72	-	1.77	-	1.70		
F-3	200-203	-	1.78	-	1.64		
F-4	374-377	2.14	1.54	1.97	1.52		
F-5	381-384	2.13	1.68		1.52		
Average		**2.15**	**1.68**	**1.97**	**1.61**	**2.02**	**1.72**

Table 5.32: Discrepancy of Average Velocity from Motion Tracking with Edge Detection Cross-Correlation and Hot –Film

Test Case	Cross Correlation		Hot Film	
	Slug Velocity (%)	Bubble Velocity (%)	Slug Velocity (%)	Bubble Velocity (%)
A	5	0	4	57
B	1	2	4	7
C	4	2	5	0
D	10	6	2	3
E	3	1	0	7
F	8	4	6	2

The results from the three methods compare favorably for the six flow cases, except for the bubble velocity from the hot films for Case A. In this case, the hot-film bubble velocity measurement yields a considerably higher value than the two flow visualization methods. This is due to the directional insensitivity of the hot-film anemometry system and the small quantity of bubbles present for this flow condition. At low liquid flow rates, the flow visualization indicates a substantial amount of re-circulation (back flow) that makes it difficult to estimate flow velocities using a direct cross-correlation method. This can be overcome by calculating individual bubble velocities and obtaining an average of the individual velocities.

With the exception of Case A, the average discrepancy between velocities for each of the flow conditions is under 10 percent. The average agreement for the bubble velocities from the edge-detection cross-correlation technique is within 2.5 percent of the motion tracking results. The velocities from the motion tracking algorithm are, to an average,

within 3.8 percent of the hot-film results, except for case A. The estimated bubble velocity using the hot-film and edge detection cross-correlation techniques is an average value over a large number of bubbles, whereas the bubble velocity estimated using the motion tracking algorithm is an average of only a few selected bubbles. The accuracy of the bubble velocity using the motion tracking algorithm can be improved by tracking additional gas bubbles. An average velocity obtained from a larger number of bubbles would reduce any error associated with the motion tracking algorithm.

Chapter 6

Conclusions and Recommendations

6.1 Conclusions

A flow visualization system was developed to obtain quantitative information of gas-liquid vertical-up two-phase flows. The system, installed in the MUN Multiphase Flow Loop Facility, uses a high speed digital imaging system that consists of a CCD camera, PCI interface and digital image memory. The images obtained with this system were processed using a motion tracking algorithm and a newly developed edge-detection cross-correlation algorithm. To the best of the author's knowledge, this is the first attempt to obtain quantitative information from multi-phase flow using an edge detection cross-correlation algorithm. The results compare favorably with simultaneous hot-film anemometry measurements.

The flow visualization test section is constructed of clear optical grade acrylic tubing and is located immediately downstream of the hot-film anemometry test section. The selected location for the flow visualization system relative to the hot-film anemometry system makes it ideal for simultaneous flow measurements. The flow visualization system is installed to incorporate the use of two separate lighting techniques: backlighting and laser light. The backlighting technique uses halogen lamps and is ideal for a complete analysis and understanding of the entire flow. The laser light technique uses a 5W Ar-Ion laser and an optic setup to create a thin sheet of light suitable for obtaining a

two dimensional image at a selected location in the vertical plane of the flow. Both techniques incorporate a scale to calibrate the images.

Two image processing algorithms were successfully developed to obtain quantitative and qualitative information of vertical-up gas-liquid two-phase flow. The supervised motion tracking algorithm identifies the movement of manually selected distinguishable fluid entities between consecutive frames of the flow. The edge detection cross-correlation algorithm defines the boundaries of gas bubbles/slugs and determines the individual velocities. The estimated velocities from both methods compare favorably, however, some modifications are required to automate the analysis of images containing slugs using the cross-correlation algorithm. Presently, smaller bubbles must be removed from the original image and the resulting image processed using the cross-correlation algorithm with a coarser grid structure. In general, the edge detection cross-correlation method has the advantages of removing the subjectivity associated with the supervised motion tracking algorithm and reducing the required processing time. Estimating the velocity over several frames of the flow sequence increases the accuracy of both methods. The accuracy of the bubble velocity obtained using the supervised motion tracking algorithm can also be improved by tracking a larger number of gas bubbles. The results obtained from the flow visualization techniques compare favorably with those from hot-film anemometry measurements. The directional insensitivity of the hot-film anemometry system makes it unsuitable for flows with a significant amount of flow recirculation. The edge detection cross-correlation algorithm can also estimate the

bubble size distribution in the flow. This is particularly useful to estimate the interfacial areas, which is an important parameter for modeling two-phase flows.

6.2 Research Contributions

The development of a quantitative flow visualization system to measure gas velocities in two-phase vertical-up flows has significantly enhanced the capabilities of the MUN Multiphase Flow Loop Facility. The flow visualization system includes the equipment necessary to obtain high speed images of the flow and algorithms to extract gas bubble velocity and size information. This research has ensured that the equipment, procedures and processing algorithms are in place to test the INSTRUMAR Multiphase Flow Meter (MPFM). The system will also be an excellent diagnostic tool to troubleshoot problems with the MPFM velocity inversion algorithms. Benchmark testing of the flow visualization system has shown that accurate gas velocities can be achieved using both the motion tracking and edge detection cross-correlation algorithms. Additional work, directed toward the analysis of the laser light images and improvement of the edge detection cross-correlation algorithm can further enhance the flow visualization system. Simultaneous flow visualization, using both lighting techniques, and hot-film anemometry data has been collected, catalogued and archived on compact discs for numerous flow conditions to assist with future development and verification of the edge-detection cross-correlation algorithm.

6.3 Recommendations

It is recommended that additional work be conducted to enhance the operation of the edge detection cross-correlation algorithm and to investigate the information that can be obtained from the laser light sheet images. The current revision of the edge-detection cross-correlation algorithm is able to handle the images obtained using the laser light sheet, but has not been tested or verified. Additional work is required to verify the operation of this code before it can be used to obtain bubble velocity and size information from flow images.

Methods to enhance the edge-detection cross-correlation technique are required. Much of this work should be focused on obtaining a more accurate estimate of the gas slug velocity which can be achieved through several steps:

1. Modify the approximation of a gas slug as a circle to either an oval or elliptical geometry to better model the true shape of the gas slug.
2. Formulate a method to prevent large dense clusters of bubbles from appearing to be slugs.
3. Incorporate a means to automatically adjust the interrogation area to better capture details of the slug tip. A coarser grid structure surrounding the slug appears to produce more accurate slug velocity results.

4. Remove any small gas bubbles surrounding the slug and use a double pass of the CROSSCORR function to capture the details of the gas bubbles and slugs separately.
5. Devise an improved method to select velocity vectors from the velocity vector matrix that better represent the true slug velocity.
6. Replace the threshold method currently used to filter the velocity vectors with a statistical method.

The images obtained using the laser light sheet are essentially two-dimensional and can also be used to obtain quantitative information from the flow. A two-dimensional image of a vertical slice of the flow eliminates problems associated with locating the spatial position of bubbles. This is a problem encountered with the three-dimensional images obtained using the back lighted technique. Accurate velocity information can be obtained from the laser light images using either the motion tracking or edge detection cross-correlation techniques. The reduced concentration of small bubbles in a slice of the flow eliminates many of the problems associated with determining the slug velocity using the edge detection cross-correlation algorithm. Figures 6.1 and 6.2 show sequences of images obtained using the laser light sheet technique for the passage of a gas slug and gas bubbles respectively. In these images the gas phase appears white and the liquid phase black.

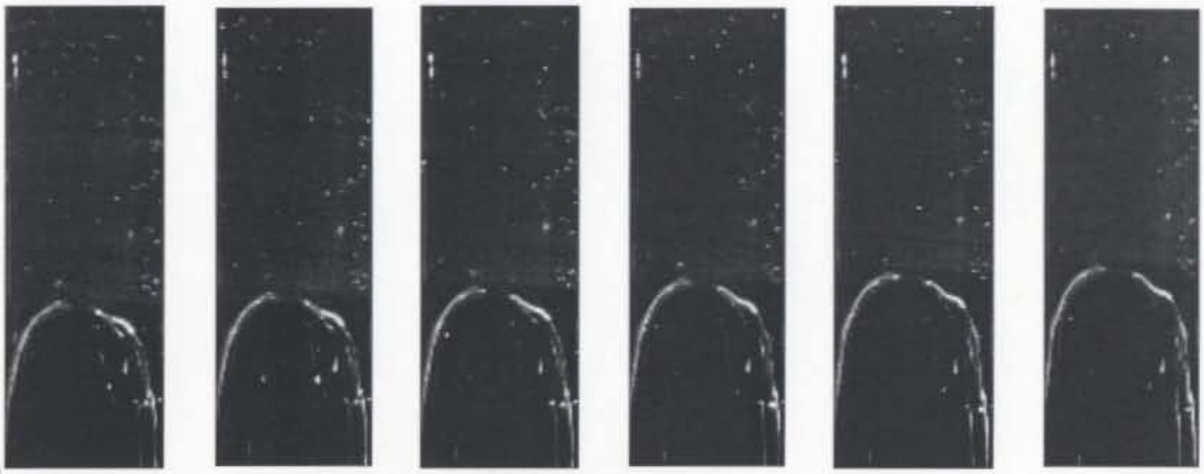

Figure 6.1: A Time Sequence Showing the Passage of a Gas Slug obtained using the Laser Light Sheet Technique

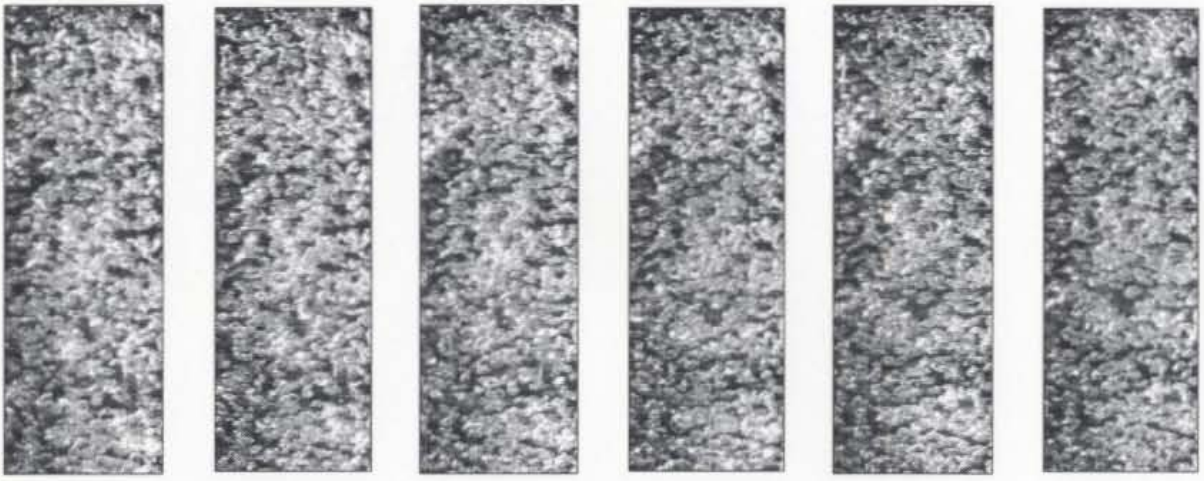

Figure 6.2: A Time Sequence Showing the Passage of Gas Bubbles obtained using the Laser Light Sheet Technique

References

Abel, R. and Resch, F. J., 1978: A Method For The Analysis of Hot-Film Anemometer Signal in Two-Phase Flows, *Int. J. Multiphase Flow*, Vol. 4, 523-533.

Adrian, Ronald J., 1991: Particle-Imaging Techniques for Experimental Fluid Mechanics, *Annual Review of Fluid Mechanics*, Vol. 23, pp.261-304.

Bachalo, W. D., 1994: Experimental Methods in Multiphase Flows, *International Journal of Multiphase Flow*, Vol. 20, pp.261-295.

Baker, O., 1954: Simultaneous Flow of Oil and Gas, *Oil Gas Journal*, 26 July, pp. 185-195.

Barker, D. B. and Fourney, M. E., 1977: Measuring Fluid Velocities with Speckle Patterns, *Opt. Lett.*, Vol. 1, pp. 135-137.

Burch, J. M. and Tokarski, J. M. J., 1968: Production of Multiple Beam Fringes from Photographic Scatters, *Opt. Acta.*, Vol. 15, pp. 101-111.

Cartellier, A. 1990: Optical Probes For Local Void Fraction Measurements: Characterization of Performance, *Rev. Sci. Instrum.* Vol. 61, No. 2, pp. 874-886.

Cartellier, A. 1992: Simultaneous Void Fraction Measurement, Bubble Velocity, and Size Estimate Using A Single Optical Probe in Gas-Liquid Two-Phase Flows, *Rev. Sci. Instrum.*, Vol. 63, No. 11, pp. 5442-5453.

Cartellier, A. and Barrau, E., 1998: Monofiber Optical Probes For Gas Detection and Gas Velocity Measurements: Conical Probes, *Int. J. of Multiphase Flow*, Vol: 24, pp. 1265-1294.

Cheng, Xin, 2000: Feature-Based Motion Estimation and Motion Segmentation, M. Eng Thesis, Memorial University of Newfoundland, Faculty of Engineering and Applied Sciences.

Ching, C. Y., Hiscock, J., Cheng, X. and Robinson, J., 1999b: Estimation of Gas Slug Velocities in Two-Phase Flows using Successive Images of the Flow, CANCAM99, Hamilton, Ontario.

Ching, C. Y., Wang, G. and Marshall A. R., 1998: A Multi-Phase Flow Research Facility to Study Oil-Water-Gas Flow Systems, *Proc. ASME Heat Transfer Division, IMECE98,* HTD-Vol. 361-5, pp. 439-444.

Ching, C. Y., Wang, G. and Marshall A. R., 1999a: Measurement of Mean Liquid and Gas Phase Velocities in Two Phase Flows using Hot-Film Anemometry, *3rd ASME/JSME Joint Fluids Engineering Conference, 7th International Symposium on Gas-Liquid Two-Phase Flows, San Francisco, California.*

Delhaye, J.M., 1981: Two Phase Flow and Heat Transfer in Power and Process Industries, Hemisphere Publishing.

Dudderar, T. D. and Simpkins, P. G., 1977: Laser Speckle Photography in a Fluid Medium, *Nature*, Vol. 270, pp.45-47.

Farrar, B and Brunn, H. H., 1989: Interaction Effects Between A Cylindrical Hot-Film Anemometer Probe And Bubbles in Air/Water And Oil/Water Flows, *J. Phys. E. Sci. Instr.*, Vol. 22, pp. 114-123.

Farrar, B, Samways, A. L., Ali, J. and Brunn, H. H., 1995: A Computer-Based Hot Film Technique For Two-Phase Flow Measurement, *Meas. Sci. Technol.*, Vol. 6, pp. 1528-1537.

Farrar, B. 1988: Hot-Film Anemometry in Dispersed Oil-Water Flows, *Ph.D. Thesis*, Department of Mechanical and Manufacturing Engineering, University of Bradford.

Gopal, M. and Jepson, W. P., 1998: The Study of Dynamic Slug Flow Characteristics Using Digital Image Analysis – Part I: Flow Visualization, *Journal of Energy Resources Technology*, Vol. 120, pp.97-101.

Graps, A., 1995: An Introduction to Wavelets, *IEEE Computational Science and Engineering*, Vol. 2, No. 2, pp. 50-61.

Grousson, R. and Mallick, S., 1977: Study of Flow Pattern in a Fluid by Scattered Laser Light, *Applied Optics*, Vol. 16, pp. 2334-2336.

Hawighorst, A., 1983: Drop Size Measurement in a Vertical Gas-Liquid Flow, *Procedings of the International Union of Theoretical and Applied Mechanics Symposium,* pp. 23-40.

Hay, K. J., Liu, Z. C., Hanratty, T. J., 1998: A Backlighted Imaging Technique for Particle Size Measurements in Two-Phase Flows, *Experiments in Fluids*, Vol. 25, pp.226-232.

Herringe, R. A. and Davis, M. R., 1974: Detection of Instantaneous Phase Change in Gas-Liquid Mixtures, *J. Phys. E. Sci. Instrum.*, Vol. 7, pp. 807-812.

Herringe, R. A. and Davis, M. R., 1976: Structure Development of Gas-Liquid Mixture Flows, *J. Fluid Mech.*, Vol. 73, pp. 97-123.

Hetsroni G., 1982: Handbook of Multiphase Systems, *Hemisphere Publishing.*

Hewitt, G. F. and Hall-Taylor, N. S., 1970: Annular Two-Phase Flow, *Pergamon Press*.

Jensen, A., Huseby, M., Sveen, J. K. and Grue, J., 1999: Measurements of Velocities and Accelerations in Steep Irregular Water Waves, 10th International Symposium on Applications of Laser Techniques to Fluid Mechanics.

Jones, O. C. and Zuber, N., 1978: Use of A Cylindrical Hot-Film Anemometer for Measurement of Two-Phase Void and Volume Flux Profiles in a Narrow Rectangular Channel, *AIChE Symp. Series*, Vol. 74, No.174, pp. 191-204.

Kirouac, G. J., Trabold, T. A., Vasallo, P. F., Moore, W. E. and Kumar, R., 1999: Instrumentation Development in Two-Phase Flow, *Experimental Thermal and Fluid Science*, Vol. 20, pp. 79-93.

Kosterin, S. I., 1949: An Investigation of the Influenence of Diameter and Inclination of a Tube on the Hydraulic Resistance and Flow Structure of Gas Liquid Mixtures, *Izv. Akad. Nauk SSSR, Otdel Tekh. Nauk*, 12, pp. 1824-1830.

Lemonnier, H., 1997: Multiphase Instrumentation: The Keystone of Multidimensional Multiphase Flow Modeling, *Experimental Thermal and Fluid Science*. Vol. 15, pp. 154-162.

Lin, P. Y. and Hanratty, T. J., 1987: The effect of pipe diameter on flow patterns for air water flow in horizontal pipes, *Int. J. Multiphase Flow*. Vol. 13, pp. 549-563.

Liu, T. J and Bankoff, S. G. 1993a: Structure of Air-Water Bubbly Flow in A Vertical Pipe - I. Liquid Mean Velocity And Turbulence Measurements, *Int. J. Heat Mass Transfer*. Vol. 36, No. 4, pp. 1049-1060.

Liu, T. J and Bankoff, S. G. 1993b: Structure of Air-Water Bubbly Flow in A Vertical Pipe - II. Void Fraction, Bubble Velocity and Bubble Size Distribution, *Int. J. of Heat Mass Transfer*. Vol. 36, No. 4, pp. 1061-1072.

Lunde, O., Hustvedt, E. and Linga, H., 1998: Field Measurements of Volumetric Phase Fraction in Multiphase Flowlines.

Mcquillan, K. W. and Whalley, P. B., 1985: Flow Patterns in Vertical Two-Phase Flow, *International Journal of Multiphase Flow*, Vol. 11, No. 2, pp. 161-175.

Meng, H., Boot, P. and Van Der Geld, C. W. M., 1995: High Pressure Optical Measurements of Sizes, Velocities and Longitudinal Positions of Bubbles, *International Journal of Multiphase Flow*, Vol. 21, No. 1, pp.95-105.

Moujaes, S. F. and Sparks, J. C., 1998: Determination of Local Two-Phase Variables And Flow Pattern Characterization in An Upward-Flow Rectangular Channel, *Proceedings of The ASME Heat Transfer Division*, Vol. 5, pp. 281-288.

Ohba, K., Tsutomu, H. and Matsuyama, H., 1987: Simultaneous Measurements of Bubble and Liquid Velocities in Two-Phase Flow using LDA, *Bulletin of JSME*, Vol. 29, pp. 2487-2493.

Peterson, D. A., Tankin, R. S. and Bankoff, S. G., 1983: Holographic Measurements of Bubble Size and Velocity in a Three-Phase System, *Procedings of the International Union of Theoretical and Applied Mechanics Symposium*, pp. 1-22.

Prenel, J.P., Porcar, R. and Rhassouli, A. El, 1989: Three-Dimensional Flow Analysis by means of Sequential and Volumic Laser Sheet Illumination, *Experiments in Fluids*, Vol. 7, pp. 133-137.

Resch, F. J., Leutheussar, H. J., and Alemu, S., 1974: Bubbly Two-Phase Flow in Hydraulic Jump, *J. Hyd. Div. ASCE* 100, No. *HYI*, pp. 137-149.

Seleghim, Paulo Jr. and Hervieu, Eric, 1998: Direct Imaging of Two-Phase Flows by Electrical Impedance Measurements, *Measurement Science Technology*, Vol. 9, pp. 1492-1500.

Serizawa, A., 1974: Fluid Dynamic Characteristics of Two Phase Flow, *Doctoral Thesis,* Kyoto University.

Serizawa, A., Kataoka, I. and Michiyoshi, I., 1987: Phase Distribution in Bubbly Flow, *Second International Workshop on Two-Phase Flow Fundamentals,* Tory, NY.

Serizawa, A., Tsida, K. and Michiyoshi, I., 1983: Real-Time Measurement of Two-Phase Flow Turbulence using Dual-Sensor Anemometry, *Proc. Symp. on Measuring Techniques in Gas-Liquid Two-Phase Flows*, Nancy, France, pp. 495-523.

Taitel, Y., Bornea, D. and Dukler, A. E., 1980: Modeling flow pattern transitions for steady upward gas-liquid flow in vertical tubes, *AIChE J.* Vol. 26, pp. 345-354.

Uga, T., 1972: Determination of Bubble-Size Distribution in A BWR, *Nucl. Engng Design*, Vol. 22, pp. 252-261.

Welle, R., 1985: Void Fraction, Bubble Velocity and Bubble Size in Two-Phase Flow, *Int. J. Multiphase Flow*, Vol. 11, No. 3, pp. 317-345.

Appendix A

MATLAB Program Listing for Edge Detection Cross-Correlation Algorithm
(Ordered Alphabetically)

BUBBLECLASSIFICATION Function

```
function [class]=bubbleclassification(doverD)

% Classify each gas bubble based on the ratio of its calculated diameter
% to the pipe diameter (doverD).
[row,column]=size(doverD);
for z=1:1:column
if doverD(1,z) >= 0.5  %slug
  class(z)=3;
elseif doverD(1,z)>0.2 & doverD(1,z)<0.5  %medium bubble
  class(z)=2;
else  %small bubble
  class(z)=1;
end
end
```

BUBBLEFILL Function

```
function[bw,xbar,ybar,class,doverD,blackpixel,percentgas,bubble_area,bubble_dia]=
bubblefill(im1,n,m,lighting,xorig,yorig,length,height,cal)

% Define image counter
imcount=0;

% Load images from files and define as frame1 and frame2
image=imread(im1);

% Crop image
crop=imcrop(image,[xorig,yorig,length,height]);
figure(1),subplot(1,n,m),imshow(crop,'notruesize'),
title('Cropped');

% Gamma correction and intensity adjustment. The gamma value is weighted
% toward darker output values (gamma > 1) in order to highlight slug and
% bubble characteristics.
[x,map]=imread(im1);
gamma=ind2gray(x,map);
if strcmp(lighting,'backlight')==1
  adjint=imadjust(gamma,[ ],[ ],2.5);
elseif strcmp(lighting,'laser')==1
  adjint=imadjust(gamma,[ ],[ ],0.4);
else
  disp('Not a valid lighting technique!')
end
adjint=imcrop(adjint,[xorig,yorig,length,height]);
figure(2),subplot(1,n,m),imshow(adjint,'notruesize'),
title('Int Adj');

% Ask for user input about the existence of a slug. If a slug is defined,
% smoothly interpolate inward from the pixel values on the boundary of
% a specified polygon.
user=1;
user=input('To select a slug region type s, otherwise to continue type c','s');

if user=='s'
  [x,y,slugfill,BW,xi,yi]=roifill(adjint);
elseif user=='c'
  disp('No slug selected. Continue...');
  slugfill=adjint;
else
```

```
 disp('Not a valid entry!');
end
% Convert image to a two-level image (black and white)
bw=im2bw(slugfill,0.85);
if strcmp(lighting,'backlight')==1
 figure(3),subplot(1,n,m),imshow(bw,'notruesize'),
 title('B&W');
elseif strcmp(lighting,'laser')==1
 figure(3),subplot(1,n,m),imshow(~bw,'notruesize'),
 title('B&W');
else
 disp('Not a valid lighting technique!')
end

% Calculate the total number of pixels in each image
pixelcount=(length)*(height);

% Calculate the number of black pixels(gas). The function bwarea calculates
% the weighted number of on pixels. On pixels are white and designated 1.
if strcmp(lighting,'backlight')==1
 blackpixel = bwarea(~bw);
else
 blackpixel = bwarea(bw);
end

% Calculate the ratio of gas area to the total area using pixel values
percentgas=(blackpixel/pixelcount)*100;

%%%%%%%%%%%%%%%%%%%%%%%%%%%%%%%%%%%%%%%%%%%%%%%%%%%%%%%%%%%%%%%%%%%%%%%
 % The following code is required for sparse images. This helps to completely fill the
bubbles.
 if percentgas<30
  %Find edges in original images (~ inverts black and white)
  disp('sparse mode')
  ed=edge(bw,'log',-10);
  ed=bwperim(ed,8);  %Determines the perimeter of an object

  %Morphological operations to fill bubbles/slugs to create an area
  if strcmp(lighting,'backlight')==1
   morph=bwmorph(ed,'clean',2); %Removes individual pixels
   morph=bwfill(morph,'holes',8); %Fills bounded regions
   %Image Addition
   bw_d=double(bw);
   morph_d=double(morph);
```

```
    fill=(morph_d)+(~bw_d);
    bw=~fill;
    % Display figures
    figure(4),subplot(1,n,m),imshow(bw,'notruesize'),
    title('Sparse');
    figure(5),subplot(1,n,m),imshow(~ed,'notruesize'),
    title('Edge')
    % Calculate new area of black pixels (gas).
    blackpixel = bwarea(~bw);
  else
    morph=bwmorph(ed,'clean',2); %Removes individual pixels
    morph=bwfill(morph,'holes',8); %Fills bounded regions
    %Image Addition
    bw_d=double(bw);
    morph_d=double(morph);
    fill=(morph_d)+(bw_d);
    bw=fill;
    % Display figures
    figure(4),subplot(1,n,m),imshow(~bw,'notruesize'),
    title('Sparse');
    figure(5),subplot(1,n,m),imshow(~ed,'notruesize'),
    title('edge')
    % Calculate new area of balck pixels (gas).
    blackpixel = bwarea(bw);
  end

  % Calculate the ratio of gas area to the total area using pixel values
  percentgas=(blackpixel/pixelcount)*100

 end
%%%%%%%%%%%%%%%%%%%%%%%%%%%%%%%%%%%%%%%%%%%%%%%%%%%%%%%%%%%%%%%%%%%%%%%%%%%%

% Determine the relative size of each bubble as the ratio of each bubble area
% to the total bubble area.  This is done using the relbubblesize function.
% This function also calculates the center of mass for each gas bubble.
[xbar,ybar,doverD,bubble_area,bubble_dia]=relbubblesize(bw,cal);

% Classify each gas bubble as small(1), medium(2) or slug(3) using the
% bubbleclasssification function.
[class]=bubbleclassification(doverD);
```

CROSSCORR Function

```
function[xvel,yvel,xcoord,ycoord,xcorr]=crosscorr(im1,im2,seg,framerate,xorig,yorig,
length,height,cal,n,m,shift)

%Determines horizontal and vertical velocities of bubbles and slugs between
%consecutive frames of a flow sequence using a cross-corrolation algorithm. The
%images are segmented into equal size square regions so that velocities can be
%determined for each region.
%
%im1 and im2 are the filenames of two consecutive images defined as 'filename.ext'
%
%seg is the size of the segmented region in pixels
%
%framerate is the camera speed measured in frames per second(fps)
%
%The following parameters remain constant for an image sequence and are obtained
%from the results of the REDUCTION Function:
%  scale_dist   required for calibration
%  pixel_dist   required for calibration
%  xorig        x coordinate of image upper left corner
%  yorig        y coordinate of image upper left corner
%  length       horizontal width/length of image
%  height       vertical height of image

% Start internal clock to determine processing time
tic

% Read two consecutive images as specified by im1 and im2
im1=imread(im1);
im2=imread(im2);

% Convert calibration to metric units
metcal=cal*0.0254;  %meters per pixel calibration

% Crop images to be exactly the same pixel size in order to remove area outside
% of the test section
im1=imcrop(im1,[xorig,yorig,length,height]);
im2=imcrop(im2,[xorig,(yorig-shift),length,height]);

% Matrix reduction to adjust image coordinates
x_min=1;
x_max=length;
y_min=1;
```

```
y_max=height;
im1=im1(y_min:y_max,x_min:x_max);
im2=im2(y_min:y_max,x_min:x_max);

% Convert images to double precision.  Required for most image processing functions.
im1=double(im1);
im2=double(im2);

% Reset loop counters
counti=1;
countj=1;

% Create a zero array for xvel, yvel, xcoord and ycoord to begin first loop.
xvel=zeros(ceil((size(im1,1)-seg)/((1)*seg)),ceil((size(im1,2)-seg)/((1)*seg)));
yvel=xvel;
xcoord=xvel;
ycoord=yvel;

% Create a nested double loop to accommodate horizontal and vertical segmentation
for jj=1:(1)*seg:size(im1,1)-seg
  for ii=1:(1)*seg:size(im1,2)-seg
    im1seg=im1(jj:jj+seg-1,ii:ii+seg-1);
    im2seg=im2(jj:jj+seg-1,ii:ii+seg-1);

    % Calculate the standard deviation of each of the segmented regions
    im1stad=std2(im1seg);
    im2stad=std2(im2seg);

    % To prevent division by zero during cross-correlation it is necessary to
    % define the standard deviation as NaN if it is identically equal to zero.
    if im1stad==0
     im1stad=NaN;
    end

    if im2stad==0
     im2stad=NaN;
    end

    % Subtract the mean intensity of each region to avoid correlation of the mean.
    im1seg=im1seg-mean2(im1seg);
    im2seg=im2seg-mean2(im2seg);

    % Calculate the cross-correlation using xcorrf2(written by R. Johnson as
    % downloaded from the Mathworks web site).
```

```
% It is necessary to divide by the product of the horizontal segment size,
% vertical segment size, horizontal standard deviation and vertical
% standard deviation to normalize the cross-correlation peak heights. This
% is an approximation to dividing by a calculated correlation coefficient.
if isnan(im1stad)~=1 & isnan(im2stad)~=1  %not equal to operator
 R=xcorrf2(im1seg,im2seg)/(seg*seg*im1stad*im2stad);

 % Create bias correction matrix and use to correct for displacement bias
 bias_cor=conv2(ones(seg),ones(seg))/(seg*seg);
 R=R./bias_cor;

 % Plot 3-D cross-correlation function.
 %figure(2+countj),subplot(1,round(length/seg),counti),
 %mesh(R(round(0.5*seg):round(1.5*seg),round(0.5*seg):round(1.5*seg))),

 % Locate the x and y coordinates of the peak of the cross-correlation
 % function.  Curve is symmetrical therefore to reduce calculation
 % time it is only necessary to search central band.

[y1,x1]=find(R==max(max(R(ceil(0.5*seg):ceil(1.5*seg),ceil(0.5*seg):ceil(1.5*seg)))));

 % If more than one set of coordinates correspond to the same peak, select the first.
 if size(x1,1)>1 | size(y1,1)>1  %Logical or operator
  disp('check, more than one coordinate!!')
  x1=x1(1);
  y1=y1(1);
 end

 % Interpolate using a specified curve fit to find a more accurate estimate of the x
and y coordinates of the peak.  A three point Gaussian fit has been used in the 'intpeak'
function.
 [x0,y0]=intpeak(x1,y1,R(y1,x1),R(y1,x1-1),R(y1,x1+1),R(y1-1,x1),R(y1+1,x1),2);

 % Calculate displacement of peak coordinates in pixels
 xdisp=x0-seg;
 ydisp=(y0-seg)+(shift);

 % Determine x and y coordinates for velocity vector location for velocity vector
plot.
 xcoord(countj,counti)=(seg/2)+ii-1;
 ycoord(countj,counti)=(seg/2)+jj-1;

 % Calculate x and y velocities and store corresponding cross-correlation
 xvel(countj,counti)=-(xdisp/(1/framerate));
```

```
      yvel(countj,counti)=(-ydisp/(1/framerate));
      xcorr(countj,counti)=R(y1,x1);

    end  % End for cross-correlation loop

    % Update counter for nested loop
    counti=counti+1;

  end  % End for nested for loop

  % Reset counter for nested loop for subsequent passes
  counti=1;

  % Update counter for outer loop
  countj=countj+1;

end  % End for outer loop

%Do not execute vector plots and interpolation for pass to calculate the segmentation
%shift.
if shift>0

% Set scale for velocity vector plots
scale=NaN;
if seg<20
  scale=2;
else
  scale=0.5;
end

% Plot velocity vectors laid over original image
figure(6),subplot(1,(n-1),(m-1)),imshow(im1,[],'notruesize'),
title('Vector');
axis on,hold
figure(6),quiver(xcoord,ycoord,xvel,yvel,scale,'g');

end%if

%**********************************************************************
% Check velocity vectors and attempt to replace negative values with vectors interpolated
%from neighbouring velocities. This algorithm uses the interpolation function
%naninterp.m written by J. Kristian downloaded from the Mathworks web site.

 % Clear variables from memory
```

```
clear yy xx nxcoord nycoord nxvel nyvel new_xvel new_yvel

% Search for velocity vectors in the opposite direction to flow
% yy and xx are coordinates of negative velocities
[yy,xx]=find(yvel>0);
new_xvel=xvel;
new_yvel=yvel;

for j=1:size(yy,1)
  nxcoord(j)=xcoord(yy(j),xx(j));
  nycoord(j)=ycoord(yy(j),xx(j));
  nxvel(j)=xvel(yy(j),xx(j));
  nyvel(j)=yvel(yy(j),xx(j));

  % Now asign NotANumber (NaN) to all the points in the matrix that require
  % interpolation of a new velocity vector.
  new_xvel(yy(j),xx(j))=NaN;
  new_yvel(yy(j),xx(j))=NaN;
end

% Interpolate the NaN's
   disp('Interpolating velocity vectors.....')
   [new_xvel,new_yvel]=naninterp(new_xvel,new_yvel);
%*********************************************************************

%Plot velocity vectors if shift > 0.
if shift>0

% Plot corrected velocities.
figure(7),subplot(1,(n-1),(m-1)),imshow(im1,[],'notruesize'),
title('Interp');
axis on,hold
figure(7),quiver(xcoord,ycoord,new_xvel,new_yvel,scale,'r');

end %if

% Calibrate velocity based on pixel to distance scale measurements
new_xvel_cal=(new_xvel)*metcal;
new_yvel_cal=-(new_yvel)*metcal;

% Assign/display variables to be carried by function
xvel=new_xvel_cal;
yvel=new_yvel_cal;
```

```
% Average y-velocity for each vertical segment
%avg_new_yvel_cal=mean(new_yvel_cal)

% Stop internal clok and display processing time
toc
```

INTPEAK Function

```
function [x0,y0]=intpeak(x1,y1,R,Rxm1,Rxp1,Rym1,Ryp1,method)

% function [x0,y0]=intpeak(x1,x2,x3,y1,y2,y3,method,N)
% METHOD =
% 1 for centroid fit,
% 2 for gaussian fit,
% 3 for parabolic fit
% x1 and y1 are maximal values in respective directions.
% N is interrogation window size.

if method==1
  x0=(((x1-1)*Rxm1)+(x1*R)+((x1+1)*Rxp1)) / (Rxm1+ R+Rxp1);
  y0=(((y1-1)*Rym1)+(y1*R)+((y1+1)*Ryp1)) / (Rym1+ R+Ryp1);
elseif method==2
  x0=x1 + ( (log(Rxm1)-log(Rxp1))/( (2*log(Rxm1))-(4*log(R))+(2*log(Rxp1))) );
  y0=y1 + ( (log(Rym1)-log(Ryp1))/( (2*log(Rym1))-(4*log(R))+(2*log(Ryp1))) );
elseif method==3
  x0=x1 + ( (Rxm1-Rxp1)/( (2*Rxm1)-(4*R)+(2*Rxp1)) );
  y0=y1 + ( (Rym1-Ryp1)/( (2*Rym1)-(4*R)+(2*Ryp1)) );
else
('Please include your desired peakfitting function; 1 for 3-point fit, 2 for gaussian fit, 3
for parabolic fit')
end

x0=real(x0);
y0=real(y0);
```

MULTIMAGES Function

```
function multimages(frame,seg,framerate,lighting)

% Start loop timer
tic

% Close all open figure windows
close all

% Count number of input images(n)
nn=length(frame);

% Define image coordinates.  This removes unwanted information such as background
% noise.
xorig=188;
yorig=76;
length=136;
hheight=316;
sseg=seg

% Calibrate image with scale(Y2-Y1)
scale_dist=4;
pixel_dist=176.7;  %(Y2-Y1)
cal=scale_dist/pixel_dist;  %inches per pixel calibration for scale

% Calculate image shift to improve segmentation and cross-correlation results
shift = 0;
im1=frame{1};
im2=frame{2};
m=2;
n=2;
height=length
seg=length
[xvel,yvel,xcoord,ycoord,xcorr]=crosscorr(im1,im2,seg,framerate,xorig,yorig,length,
height,cal,n,m,shift);
yvel
shift=fix(yvel*(1/framerate)*(1/(cal*0.0254)))
n=nn;
height=hheight;
seg=sseg;

for m=1:n
 % Define image im1 for each image in the list defined by frame.
```

```
 im1=frame{m};
[bw,xbar,ybar,class,doverD,blackpixel,percentgas,bubble_area,bubble_dia]=bubblefill
(im1,n,m,lighting,xorig,yorig,length,height,cal);
 bbw(:,:,m)=bw(:,:);

 % Determine matrix positions for each bubble size
 slug=find(class==3);
 medbub=find(class==2);
 smlbub=find(class==1);

 % Count number of slugs, medium bubbles and bubbles
 num_slug=size(slug,2) %2 indicates counting number of columns in matrix
 num_medbub=size(medbub,2)
 num_smlbub=size(smlbub,2);

 % If there are no slugs, medium bubbles or small bubbles, automatically
 % assign a velocity of zero.
 if num_slug==0
   slug_vel=0
 end
 if num_medbub==0
   medbub_vel=0
 end
 if num_smlbub==0
   smlbub_vel=0
 end

 % Determine x and y coordinates of slugs and medium bubbles in 'class' matrix
 for k=1:num_slug
   slug_xbar(k)=xbar(1,(slug(1,k)));
   slug_ybar(k)=ybar(1,(slug(1,k)));
   slug_dia(k)=bubble_dia(1,(slug(1,k)));
 end

 for k=1:num_medbub
   medbub_xbar(k)=xbar(1,(medbub(1,k)));
   medbub_ybar(k)=ybar(1,(medbub(1,k)));
   medbub_dia(k)=bubble_dia(1,(medbub(1,k)));
 end

if m>1
 % Define variables for crosscorr function
 if strcmp(lighting,'backlight')==1
  im1=frame{m-1};
```

```
  im2=frame{m};
 else
  im1=~bbw(:,:,(m-1));
  im2=~bbw(:,:,m);
 end

 % Run crosscorr function and structure results
[xvel,yvel,xcoord,ycoord,xcorr]=crosscorr(im1,im2,seg,framerate,xorig,yorig,length,
height,cal,n,m,shift);

 % Calculate average y velocity of each vertical segment
 %avg_yvel(:,:,m)=mean(yvel(:,:,m));

 % Define yvel_bub to be used in calculating an average bubble velocity.
 % Each velocity used in calculating a slug or medium bubble velocity
 % is replaced with NaN.  This preserves the original velocity array(yvel).
 yvel_bub=yvel

 % Replace any zero value velocities with NaN.  This can be used to omit
 % the zero velocities when calculating average values.
  for p=1:(height/seg)
   for q=1:(length/seg)
    if yvel_bub(p,q)==0;
     yvel_bub(p,q)=NaN;
    end
   end
  end

 % Calculate slug velocity using neighbouring velocity vectors.  Replace
 % each slug velocity with NaN.
if num_slug>=1
   num=num_slug; % Define variables for function
   xxbar=slug_xbar;
   yybar=slug_ybar;
   dia=slug_dia;

   [vel,yvel_bub]= velclassmatch(height,length,seg,num,yybar,xxbar,yvel_bub,yvel,dia);
   slug_vel=vel % Define slug velocity
 end

 % Calculate medium bubble velocity using neighbouring velocity vectors.
 % Replace each medium bubble velocity with NaN.
 if num_medbub>=1
   num=num_medbub; % Define variables for function
```

```
    xxbar=medbub_xbar;
    yybar=medbub_ybar;
    dia=medbub_dia;

    [vel,yvel_bub]= velclassmatch(height,length,seg,num,yybar,xxbar,yvel_bub,yvel,dia);
    medbub_vel=vel % Define medium bubble velocity
  end

  % Calculate average small bubble velocity
  if num_smlbub>=1
    smlbub_vel=nanmean((nanmean(yvel_bub))')%NaN's are ignored in calculating mean

    % Remove any velocity vectors that are 50% greater than or less than the
    %  average and re-calculate average bubble velocity.
    [yy,xx]=find((yvel_bub>(smlbub_vel+0.5*smlbub_vel))|(yvel_bub<(smlbub_vel-
0.5*smlbub_vel)));
    new_yvel_bub=yvel_bub;
    for j=1:size(yy,1)
      new_yvel_bub(yy(j),xx(j))=NaN;
    end
    new_yvel_bub
    smlbub_vel=nanmean((nanmean(new_yvel_bub))')
  end

% Increment variable 'image' for each loop through consecutive frames.  This
% allows the results to have a unique name in a run with more than one image.
filename=['data',num2str(m-1),'_',num2str(m)];

% Structure results and save data to file called 'filename'.
bubble_area=bubble_area';
bubble_dia=bubble_dia';
class=class';
doverD=doverD';
xbar=xbar';
ybar=ybar';
slug_vel=slug_vel';
medbub_vel=medbub_vel';
save (filename,'seg','framerate','lighting','n','xorig','yorig','length','height','yvel','slug_vel',
'medbub_vel','smlbub_vel','xvel','xbar','ybar','class','blackpixel','percentgas','bubble_area',
'bubble_dia','doverD','shift','new_yvel_bub')
disp(['Parameters saved to file:  ', filename)

end %end of if statement
end %end of for loop
```

```
% Stop loop timer and display total processing time
toc
```

NANINTERP Function

```
function [u,v]=naninterp(u,v)
% function [u,v]=naninterp(u,v)
%
% Interpolates NaN's in a vectorfield.

[dy,dx]=size(u);
[py,px]=find(isnan(u)==1);
teller=1;

while ~isempty(py)
 for j=1:size(py,1)
  if py(j)~=1 & py(j)~=dy & px(j)~=1 & px(j)~=dx
   u(py(j),px(j))=nanmean(nanmean(u(py(j)-1:py(j)+1,px(j)-1:px(j)+1)));
   v(py(j),px(j))=nanmean(nanmean(v(py(j)-1:py(j)+1,px(j)-1:px(j)+1)));
  end
  if py(j)==1 & px(j)==1
   u(py(j),px(j))=nanmean(nanmean(u(py(j):py(j)+1,px(j):px(j)+1)));
   v(py(j),px(j))=nanmean(nanmean(v(py(j):py(j)+1,px(j):px(j)+1)));
  end
  if py(j)==1 & px(j)==dx
   u(py(j),px(j))=nanmean(nanmean(u(py(j):py(j)+1,px(j)-1:px(j))));
   v(py(j),px(j))=nanmean(nanmean(v(py(j):py(j)+1,px(j)-1:px(j))));
  end
  if py(j)==dy & px(j)==1
   u(py(j),px(j))=nanmean(nanmean(u(py(j)-1:py(j),px(j):px(j)+1)));
   v(py(j),px(j))=nanmean(nanmean(v(py(j)-1:py(j),px(j):px(j)+1)));
  end
  if py(j)==dy & px(j)==dx
   u(py(j),px(j))=nanmean(nanmean(u(py(j)-1:py(j),px(j)-1:px(j))));
   v(py(j),px(j))=nanmean(nanmean(v(py(j)-1:py(j),px(j)-1:px(j))));
  end
  if py(j)==1 & px(j)~=1 & px(j)~=dx
   u(py(j),px(j))=nanmean(nanmean(u(py(j):py(j)+1,px(j)-1:px(j)+1)));
   v(py(j),px(j))=nanmean(nanmean(v(py(j):py(j)+1,px(j)-1:px(j)+1)));
  end
  if py(j)==dy & px(j)~=1 & px(j)~=dx
   u(py(j),px(j))=nanmean(nanmean(u(py(j)-1:py(j),px(j)-1:px(j)+1)));
   v(py(j),px(j))=nanmean(nanmean(v(py(j)-1:py(j),px(j)-1:px(j)+1)));
  end
  if px(j)==1 & py(j)~=1 & py(j)~=dy
   u(py(j),px(j))=nanmean(nanmean(u(py(j)-1:py(j)+1,px(j):px(j)+1)));
   v(py(j),px(j))=nanmean(nanmean(v(py(j)-1:py(j)+1,px(j):px(j)+1)));
```

```
  end
  if px(j)==dx & py(j)~=1 & py(j)~=dy
    u(py(j),px(j))=nanmean(nanmean(u(py(j)-1:py(j)+1,px(j)-1:px(j))));
    v(py(j),px(j))=nanmean(nanmean(v(py(j)-1:py(j)+1,px(j)-1:px(j))));
  end
  teller=teller+1;
 end
 [py,px]=find(isnan(u)==1);

end
```

NANMEAN Function

```
function y = nanmean(x)
%NANMEAN Average or mean ignoring NaNs.
%   NANMEAN(X) returns the average treating NaNs as missing values.
%   For vectors, NANMEAN(X) is the mean value of the non-NaN
%   elements in X.  For matrices, NANMEAN(X) is a row vector
%   containing the mean value of each column, ignoring NaNs.
%
%   See also NANMEDIAN, NANSTD, NANMIN, NANMAX, NANSUM.

%   Copyright (c) 1993-98 by The MathWorks, Inc.
%   $Revision: 2.8 $  $Date: 1997/11/29 01:45:53 $

if isempty(x) % Check for empty input.
   y = NaN;
   return
end

% Replace NaNs with zeros.
nans = isnan(x);
i = find(nans);
x(i) = zeros(size(i));

if min(size(x))==1,
  count = length(x)-sum(nans);
else
  count = size(x,1)-sum(nans);
end

% Protect against a column of all NaNs
i = find(count==0);
count(i) = ones(size(i));
y = sum(x)./count;
y(i) = i + NaN;
```

REDUCTION Function

```
function select=reduction(frame1,frame2)

%Load images from files and define as frame1 and frame2
im1=imread(frame1);
im2=imread(frame2);

%Define window for displaying images and do not adjust size
figure(1),subplot(1,2,1),imshow(im1,'notruesize');
subplot(1,2,2),imshow(im2,'notruesize');

%Pick two points from original image for calibration purposes
[X1,Y1] = ginput(1)
[X2,Y2] = ginput(1)
```

RELBUBSIZE Function

```
function [xbar,ybar,doverD,bubble_area,bubble_dia]=relbubblesize(bw,cal)

% Label each gas bubble or slug using numbers starting at 1 for the first, 2
% for the second and so on. The background is numbered 0.
bw=uint8(bw);
bubble_number=bwlabel(~bw,8); % use 8 connectivity
[num_row,num_col]=size(bubble_number);

for j=1:1:max(max(bubble_number)) %j represents/counts bubble number
 % Find center of mass(centroid) of each gas bubble
 [y,x]=find(bubble_number==j);
 [numpix]=size(y,1);
 xbar(j)=sum(x)/numpix;
 ybar(j)=sum(y)/numpix;

 % Create separate images for each gas bubble. This provides a means to check
 % function operation and to calculate each gas bubble area as a weighted
 % average (bwarea) instead of simply a pixel count. A straight pixel count
 % could be used to reduce calculation time if necessary.
 new_bubble_number=bubble_number;
 for c=1:1:num_row
  for d=1:1:num_col
   if bubble_number(c,d)==j
    new_bubble_number(c,d)=0;
   else
    new_bubble_number(c,d)=1;
   end
  end
 end

%figure(5),subplot(max(max(bubble_number)),1,j),imshow(new_bubble_number,'notrue
size');

% Calculate gas bubble area and gas bubble diameter
bubble_area(j)=bwarea(~new_bubble_number);
bubble_dia(j)=(4*bubble_area(j)/pi)^(1/2);

% Claculate d/D to determine gas bubble classification (small, medium or slug)
% d is the bubble diameter (bubble_dia). D is the inside pipe diameter.
doverD(j)=((bubble_dia(j))*cal)/3;

end
```

VELCLASSMATCH Function

```
function[vel,yvel_bub]=velclassmatch(height,length,seg,num,yybar,xxbar,yvel_bub,yvel,
dia)

% This function calculates a velocity for each slug or medium bubble based
% on a know classification.  The velocity is determined as an average of
% neighbouring velocity vectors as determind from the cross-correlation
% function.
%
% vel       velocity of the slug or gas bubble
% yvel_bub  velocity matrix with NaN's inserted for velocity values used
%           in calculating the slug and medium bubble velocities
% height    height of the image in pixel units
% length    length of the image in pixel units
% seg       size of square blocks used for segmentation
% num       number of slugs or gas bubbles
% yybar     y coordinates for centroid of slug or gas bubble
% xxbar     x coordinate for centroid of slug or gas bubble
% yvel      velocity matrix beforeNaN's are inserted

% Calculate bubble radius
rad=dia/2;

% Define positions for slug tip boundary location assuming circular geometry. Use 30
% and 60 degree positions.
xthirty=(rad)*(cos(pi/6));
ythirty=(rad)*(sin(pi/6));
xsixty=(rad)*(cos(pi/3));
ysixty=(rad)*(sin(pi/3));

for k=1:num
  % Assign variables to centroid location based on segment number rather
  % than pixel value.  Easier to identify matrix location for velocity.
  y1(k)=round(yybar(k)/seg);
  x1(k)=round(xxbar(k)/seg);
  y2(k)=round(yybar(k)/seg);
  x2(k)=round((xxbar(k)+rad)/seg);
  y3(k)=round((yybar(k)-rad)/seg);
  x3(k)=round(xxbar(k)/seg);
  y4(k)=round(yybar(k)/seg);
  x4(k)=round((xxbar(k)-rad)/seg);
  y5(k)=round((yybar(k)-(ythirty))/seg);
  x5(k)=round((xxbar(k)+(xthirty))/seg);
```

```
y6(k)=round((yybar(k)-(ysixty))/seg);
x6(k)=round((xxbar(k)+(xsixty))/seg);
y7(k)=round((yybar(k)-(ythirty))/seg);
x7(k)=round((xxbar(k)-(xthirty))/seg);
y8(k)=round((yybar(k)-(ysixty))/seg);
x8(k)=round((xxbar(k)-(xsixty))/seg);

% Replace any of the above variables that may potentially fall outside of the
% segmentation grid.

if x2(k)>fix(length/seg)
  x2(k)=fix(length/seg);
end

if y3(k)>fix(height/seg)
  y3(k)=fix(height/seg);
end

if x4(k)<1
  x4(k)=1;
end

if x5(k)>fix(length/seg)
  x5(k)=fix(length/seg);
end

if x6(k)>fix(length/seg)
  x6(k)=fix(length/seg);
end

if x7(k)<1
  x7(k)=1;
end

if x8(k)<1
  x8(k)=1;
end

% Determine velocity vectors for each slug or medium gas bubble selected form the
% velocity vector matrix.  Replace any used velocity vector with NaN in the matrix.
vel1(k)=yvel_bub(y1(k),x1(k));
yvel_bub(y1(k),x1(k))=NaN;
vel2(k)=yvel_bub(y2(k),x2(k));
yvel_bub(y2(k),x2(k))=NaN;
```

```
vel3(k)=yvel_bub(y3(k),x3(k));
yvel_bub(y3(k),x3(k))=NaN;
vel4(k)=yvel_bub(y4(k),x4(k));
yvel_bub(y4(k),x4(k))=NaN;
vel5(k)=yvel_bub(y5(k),x5(k));
yvel_bub(y5(k),x5(k))=NaN;
vel6(k)=yvel_bub(y6(k),x6(k));
yvel_bub(y6(k),x6(k))=NaN;
vel7(k)=yvel_bub(y7(k),x7(k));
yvel_bub(y7(k),x7(k))=NaN;
vel8(k)=yvel_bub(y8(k),x8(k));
yvel_bub(y8(k),x8(k))=NaN;

% Remove any velocity vectors that are less than or greater than 70% of
%  the average velocity
vectors=[vel1(k) vel2(k) vel3(k) vel4(k) vel5(k) vel6(k) vel7(k) vel8(k)];
avg_vel=nanmean(vectors);
min_vel=(avg_vel)-(avg_vel)*0.3;
max_vel=(avg_vel)+(avg_vel)*0.3;

 if (vel1(k)<(min_vel))|(vel1(k)>(max_vel))
   vel1(k)=NaN;
 end
 if (vel2(k)<(min_vel))|(vel2(k)>(max_vel))
   vel2(k)=NaN;
 end
 if (vel3(k)<(min_vel))|(vel3(k)>(max_vel))
   vel3(k)=NaN;
 end
 if (vel4(k)<(min_vel))|(vel4(k)>(max_vel))
   vel4(k)=NaN;
 end
 if (vel5(k)<(min_vel))|(vel5(k)>(max_vel))
   vel5(k)=NaN;
 end
 if (vel6(k)<(min_vel))|(vel6(k)>(max_vel))
   vel6(k)=NaN;
 end
 if (vel7(k)<(min_vel))|(vel7(k)>(max_vel))
   vel7(k)=NaN;
 end
 if (vel8(k)<(min_vel))|(vel8(k)>(max_vel))
   vel8(k)=NaN;
 end
```

```
  % Calculate the velocity as an average of the four neighbouring
  % velcoity vectors.
  vectors=[vel1(k) vel2(k) vel3(k) vel4(k) vel5(k) vel6(k) vel7(k) vel8(k) ]
  vel(k)=nanmean(vectors);
end
```

XCORRF2 Function

```
function c = xcorrf2(a,b)
%  c = xcorrf2(a,b)
%   Two-dimensional cross-correlation using Fourier transforms.
%   XCORRF2(A,B) computes the crosscorrelation of matrices A and B.
%   XCORRF2(A) is the autocorrelation function.
%   This routine is functionally equivalent to xcorr2 but faster.
%   See also XCORR2.

%   Author(s): R. Johnson
%   $Revision: 1.0 $  $Date: 1995/11/27 $

    [ma,na] = size(a);
if nargin == 1
%   for autocorrelation
    b = a;
end
    [mb,nb] = size(b);
%   make reverse conjugate of one array
    b = conj(b(mb:-1:1,nb:-1:1));

%   use power of 2 transform lengths
    mf = 2^nextpow2(ma+mb);
    nf = 2^nextpow2(na+nb);
    at = fft2(b,mf,nf);
    bt = fft2(a,mf,nf);
%   multiply transforms then inverse transform
    c = ifft2(at.*bt);
%   make real output for real input
    if ~any(any(imag(a))) & ~any(any(imag(b)))
        c = real(c);
    end
%   trim to standard size
    c(ma+mb:mf,:) = [ ];
    c(:,na+nb:nf) = [ ];
```